
Peak Effect, Hall Effect and Vortex Phases in $\text{Fe}_x\text{Ni}_{1-x}\text{Zr}_2$ Superconducting Glasses

Josianne Lefebvre

Centre for the Physics of Materials

Department of Physics

McGill University

Montréal, Québec

Canada

October, 2004



A Thesis submitted to
McGill University
in partial fulfillment of the requirements for the degree of
Master of Science

© Josianne Lefebvre, 2004



Library and
Archives Canada

Bibliothèque et
Archives Canada

Published Heritage
Branch

Direction du
Patrimoine de l'édition

395 Wellington Street
Ottawa ON K1A 0N4
Canada

395, rue Wellington
Ottawa ON K1A 0N4
Canada

Your file *Votre référence*
ISBN: 0-494-06417-X
Our file *Notre référence*
ISBN: 0-494-06417-X

NOTICE:

The author has granted a non-exclusive license allowing Library and Archives Canada to reproduce, publish, archive, preserve, conserve, communicate to the public by telecommunication or on the Internet, loan, distribute and sell theses worldwide, for commercial or non-commercial purposes, in microform, paper, electronic and/or any other formats.

The author retains copyright ownership and moral rights in this thesis. Neither the thesis nor substantial extracts from it may be printed or otherwise reproduced without the author's permission.

AVIS:

L'auteur a accordé une licence non exclusive permettant à la Bibliothèque et Archives Canada de reproduire, publier, archiver, sauvegarder, conserver, transmettre au public par télécommunication ou par l'Internet, prêter, distribuer et vendre des thèses partout dans le monde, à des fins commerciales ou autres, sur support microforme, papier, électronique et/ou autres formats.

L'auteur conserve la propriété du droit d'auteur et des droits moraux qui protègent cette thèse. Ni la thèse ni des extraits substantiels de celle-ci ne doivent être imprimés ou autrement reproduits sans son autorisation.

In compliance with the Canadian Privacy Act some supporting forms may have been removed from this thesis.

Conformément à la loi canadienne sur la protection de la vie privée, quelques formulaires secondaires ont été enlevés de cette thèse.

While these forms may be included in the document page count, their removal does not represent any loss of content from the thesis.

Bien que ces formulaires aient inclus dans la pagination, il n'y aura aucun contenu manquant.


Canada

CONTENTS

Abstract	ix
Résumé	x
Acknowledgments	xi
1 INTRODUCTION	1
2 THEORY OF SUPERCONDUCTIVITY	5
2.1 Basic Theory of Superconductivity	5
2.1.1 Basic Phenomenology	5
2.1.2 The London Equations	6
2.1.3 Pippard Electrodynamics	8
2.1.4 Results from the BCS Theory and the Superconducting Energy Gap	9
2.1.5 The Ginzburg-Landau Theory	9
2.1.6 Type II Superconductivity	11
2.1.7 Dynamics of Vortices	12
2.2 The Peak Effect	14
2.2.1 Early Hypothesis	14
2.2.2 Sample Purity Effects	15
2.2.3 Current and Vortex Distribution	17
2.2.4 AC <i>vs</i> DC Driving Current	17
2.2.5 Changing the Sample Geometry	18
2.2.6 Superposing an AC Current to a Small DC Bias	20
2.2.7 The Phase Diagram	20
3 EXPERIMENTAL TECHNIQUES	23
3.1 Samples	23
3.1.1 Sample Preparation	24
3.1.2 The Clean and Dirty Limits	24
3.1.3 Some Length Scales and Physical Properties	25
3.1.4 Structural Relaxation	27
3.1.5 Addition of Electrical Contacts to the Samples	28
3.2 Experimental Setup	28
3.2.1 Components and Operation of the ^3He Insert	29
3.2.2 Data Acquisition Methods	29
3.2.3 Systematic Errors	31

4	LONGITUDINAL RESISTANCE RESULTS	34
4.1	Critical Temperature	35
4.2	The Peak Effect	35
4.2.1	The First Depinning Phase	37
4.2.2	The Reentrant Pinning Phase	39
4.2.3	The Second Depinning Phase	39
4.3	$V - I$ Characteristics	41
4.4	Vortex Instabilities	43
4.5	Joule Heating	46
4.6	Suppression of the Pinning Phase	47
4.7	Suppression of Hysteresis	48
4.8	Compilation of Results	49
4.9	Temperature dependence	50
5	THE HALL EFFECT IN TYPE II SUPERCONDUCTORS	54
5.1	Elementary Hall Effect Phenomenology	54
5.2	Anisotropic Pinning and Guided Vortex Motion	55
5.3	A First Description of the Hall Angle	59
5.4	Transverse Critical Force	59
5.5	Previous Measurements of the Hall Resistivity in Type II Superconductors	60
6	HALL RESISTANCE RESULTS	63
6.1	Paths of Vortex Flow	64
6.2	Reversing the Magnetic Field Polarity	64
6.3	Lowest Drive Regime	65
6.4	Peak Effect Regime	66
6.5	Largest Current Drive Regime	66
6.6	Comparison with the Phase Diagram	68
6.7	Results from Other Samples	70
6.8	Hall Angle	70
6.9	Local or Extended Effect	73
6.10	$V - I$ Characteristics	74
6.11	Inverting the Current and Voltage Leads	76
6.12	Temperature Dependence	76
7	CONCLUSIONS	80
A	MORE LONGITUDINAL RESISTANCE RESULTS	84
B	MORE HALL RESISTANCE RESULTS	88
	REFERENCES	96

LIST OF FIGURES

2.1	Schematic representation of the force induced on a vortex when a current is applied to the superconductor. The moving vortex then induces an electric field in the direction antiparallel to the current.	13
2.2	Electrode configuration for measurements in the Corbino disk geometry. The red electrodes are the voltage probes and the black ones serve to supply current.	19
2.3	Schematic phase diagram of disorder <i>vs</i> force F at $T = 0$. The exact shape of the boundaries between the phases is still not known. The red square is a region in which the behavior is unclear. (Drawing adapted from Ref.[1])	21
2.4	Schematic representation of the vortex lattice in the a) moving Bragg glass (MGB) phase and b) the moving transverse glass (MTG) phase. The blue lines represent coupling between the vortices whereas the black lines are the channels in which the vortices move. In b) the presence of defects (in red) causes the positions of vortices in different channels to decouple.	22
3.1	Schematic representation of the apparatus for sample preparation by melt-spinning.	25
3.2	On the left: Cryostat, magnet and ^3He insert. On the right: ^3He insert with some of the interior components.	30
3.3	a) Conventional contact geometry for Hall effect measurements. It has the advantage that all the current lines are located between the Hall probes. b) Non-ideal contact geometry used for our measurements. The real current between the Hall probes is reduced by a factor $\frac{L_v}{L_w}$	32
4.1	Geometry used for experimental measurements of R_{xx} with the magnetic field \vec{B} perpendicular to the direction of the current applied to the sample.	34
4.2	Resistance as a function of temperature for each sample. $I = 1\text{mA}$	35
4.3	Resistance as a function of B for up and down B sweeps on sample $\text{Fe}_{0.1}\text{Ni}_{0.9}\text{Zr}_2$. The different curves are for different excitations (0.05, 0.075, 0.09, 0.1, 0.2, 0.3, 0.4, 0.5, 0.6, 0.7, 0.8, 0.9, 1, 2, 3, 4, 5 mA). Inset: Expansion of the high field region. $T \approx 400\text{mK}$	36
4.4	Resistance of the 1 mA down-sweep for $\text{Fe}_{0.1}\text{Ni}_{0.9}\text{Zr}_2$, illustrating how the phases are determined.	37
4.5	Phase diagram of vortex dynamics for sample $\text{Fe}_{0.1}\text{Ni}_{0.9}\text{Zr}_2$. Solid lines correspond to data obtained sweeping B up and the dotted lines to data obtained sweeping B down. The lower panel is an enlargement of the low I and high B region.	38

4.6	V-I curves extracted from R_{xx} vs B data for sample $x = 0.3$ for up (solid lines) and down (dotted lines) B sweeps. The different curves correspond to different B values. Main panel: B in the peak effect region. Upper inset: Enlargement of the Low- B region. Lower inset: Low- B region, full range.	42
4.7	V-I curves plotted from equation(4.3) using $R_n = 0.515$, $V^* = 0.5$ and $\alpha = 2$ (red), 4 (blue), 8 (green), 14 (black), and 18.4 (orange).	44
4.8	Black: $V - I$ characteristics extracted from R vs B data on sample $x = 0.3$ for $B = 0.8$ T. Red: Best fit to the data using equation 4.3. The best fit values were found to be $a = 13.46$ and $V^* = 0.24$	45
4.9	Longitudinal resistance vs magnetic field for up and down B sweeps on a sample with 15% Fe and with $I = 0.07, 0.25, 0.5, 0.75, 1, 1.5, 2, 3, 5, 7, 9$ mA	48
4.10	Longitudinal resistance as a function of B for a sample of $\text{Fe}_{0.2}\text{Ni}_{0.8}\text{Zr}_2$ for up (solid lines) and down (dotted lines) B sweeps and for driving currents between 0.05mA and 6mA (0.05, 0.1, 0.15, 0.5, 1, 1.5, 2, 4, 6)mA. $T=400\text{mK}$	49
4.11	Onset of the different vortex phases as a function of x , the iron concentration in $\text{Fe}_x\text{Ni}_{1-x}\text{Zr}_2$ measured with $I = 1\text{mA}$. a) Onset of depinning 1 phase. b) Onset of pinning phase. (No data point is found for $x = 0.20$ for this phase, because the data did not show a reentrant pinning phase for this current.) c) Onset of depinning 2 phase. d) B_{c2}	51
4.12	Longitudinal resistance as a function of B for a current of 1 mA applied to a sample of $\text{Fe}_{0.4}\text{Ni}_{0.6}\text{Zr}_2$. The different curves correspond to different temperatures between 0.33 K and 1.65 K (0.33, 0.38, 0.45, 0.52, 0.62,1.1, 1.34, 1.59) K.	52
4.13	Phase diagram of vortex dynamics as a function of temperature for sample $\text{Fe}_{0.4}\text{Ni}_{0.6}\text{Zr}_2$. The data was rescaled with B_{C2} and taken with $I = 1\text{mA}$	53
5.1	Schematic representation of the direction of motion of a vortex such that a Hall voltage is induced.	56
5.2	Schematic representation of the effective forces on the vortices for a) the positive Hall effect; b) the negative Hall effect.	58
6.1	Geometry used in the measurements of the Hall effect. The current is applied to the sample along the x axis and the magnetic field is applied along the z axis.	63
6.2	Enlargement of the high- B depinning 1 phase region of the R_{xy} vs B curves shown in the inset.	64
6.3	Hall resistance vs B field for up B sweeps for the two magnetic field polarities.	65
6.4	Longitudinal resistance (black curve) and Hall resistance (red curve) vs B field for up (solid lines) and down (dotted lines) B sweeps with $I = 0.1$ mA on a sample with $x = 0.3$	66

6.5	Longitudinal resistance (black curve) and Hall resistance (red curve) <i>vs</i> B field for up (solid lines) and down (dotted lines) B sweeps with $I = 0.5$ mA on a sample with $x = 0.1$. Inset: Enlargement of the peak effect region.	67
6.6	Longitudinal resistance (black curve) and Hall resistance (red curve) <i>vs</i> B field for up (solid lines) and down (dotted lines) B sweeps with $I = 5$ mA on a sample with $x = 0.1$	68
6.7	Hall resistance (red) <i>vs</i> B field for different driving currents and vortex phase diagram (blue) extracted from longitudinal resistance measurements shown on the same graph so that the correspondence between the two types of measurements can be established.	69
6.8	Longitudinal (black curves) and Hall (red curves) resistance as a function of B for up (solid lines) and down (dotted lines) B sweeps on sample $x = 0.3$ with a) $I = 0.74$ mA and b) $I = 4$ mA.	71
6.9	Hall angle <i>vs</i> B field for up (solid line) and down (dotted line) B sweep and sample $x = 0.1$ with $I = 0.5$ mA. Inset: Longitudinal (black curve) and Hall (blue curve) resistance <i>vs</i> B showing the position of the Hall peak with respect to the reentrant pinning phase for careful computation of the Hall angle.	72
6.10	Longitudinal (black) and Hall (colors) resistance <i>vs</i> B for up B sweeps. a) $I = 0.07$ mA. b) $I = 0.75$ mA. The colors of the Hall curves correspond with different voltage probes as shown in the inset of panel a).	74
6.11	$V - I$ curves extracted from R_{xy} data acquired during an increasing B sweep for B/B_{C2} : main panel: in the peak region, inset: between 0.1 and 0.8.	75
6.12	Hall resistance R_{yx} <i>vs</i> B field with the current and voltage contacts in the configuration shown in the upper left corner. The solid curves correspond to up B sweeps and the dotted lines to down B sweeps for $I=0.3, 1, 2, 2.5, 3, 4, 5, 6, 7, 8, 9, 10$ mA.	77
6.13	Hall resistance <i>vs</i> B field for up (solid lines) and down (dotted lines) B sweeps at different temperatures (0.34, 0.38, 0.45, 0.52, 0.62, 1.1, 1.35, 1.42, 1.71) K for sample $\text{Fe}_{0.4}\text{Ni}_{0.6}\text{Zr}_2$	78
6.14	R_{xy} <i>vs</i> B for up (solid lines) and down (dotted lines) B sweeps at different temperatures below T_c on sample $\text{Fe}_{0.15}\text{Ni}_{0.85}\text{Zr}_2$, and for two different contact configurations. (The curves were shifted in R so as to show the features better.)	79
6.15	3D plot of the Hall resistance (red) curves at different temperatures <i>vs</i> B field for up B sweeps and phase diagram (blue) extracted from R_{xx} measurements at different temperatures showing the evolution of the different phases of vortex motion with temperature.	79
A.1	Longitudinal resistance as a function of B for up (solid lines) and down (dotted lines) B sweeps on sample NiZr_2 and driving currents between 0.1 mA and 10 mA (0.1, 0.25, 0.5, 0.75, 1, 1.5, 2, 4, 6, 8, 10) mA. $T \approx 320$ mK.	84

A.2	Longitudinal resistance as a function of B , for up (solid lines) and down (dotted lines) B sweeps on sample $\text{Fe}_{0.3}\text{Ni}_{0.7}\text{Zr}_2$ with driving currents between 0.05 mA and 8 mA (0.05, 0.1, 0.25, 0.5, 0.75, 1, 1.5, 2, 4, 6, 8) mA. $T \approx 320$ mK.	85
A.3	Longitudinal resistance as a function of B for up (solid lines) and down (dotted lines) B sweeps on sample $\text{Fe}_{0.33}\text{Ni}_{0.67}\text{Zr}_2$ with driving currents between 0.05 mA and 6 mA (0.05, 0.15, 0.25, 0.5, 1, 1.5, 2, 3, 4, 5, 6) mA. $T \approx 320$ mK.	85
A.4	Longitudinal resistance as a function of B for up (solid lines) and down (dotted lines) B sweeps on sample $\text{Fe}_{0.4}\text{Ni}_{0.6}\text{Zr}_2$. The different curves are for different driving currents between 0.05 mA and 7 mA (0.05, 0.25, 0.5, 0.75, 1, 1.5, 2, 3, 4, 5, 6, 7) mA. $T \approx 320$ mK.	86
A.5	$V - I$ curves extracted from R_{xx} vs B data acquired during increasing B sweeps for samples a) $x = 0$, b) $x = 0.1$, c) $x = 0.2$, d) $x = 0.4$. . .	87
B.1	Hall resistance vs B field for sample NiZr_2 . The solid lines correspond to data acquired during an increasing B sweep and dotted lines correspond to decreasing B sweeps.	88
B.2	Hall resistance vs B field for sample $\text{Fe}_{0.1}\text{Ni}_{0.9}\text{Zr}_2$. The solid lines correspond to up B sweeps and the dotted lines to down B sweeps and for the following driving currents: 0.1, 0.25, 0.5, 1, 1.3, 1.66, 2.5, 3, 3.33, 4.16, 5, 6.66, 7.5, 8.3, 9.5, 10 mA.	89
B.3	R_{xy} vs B for up (solid lines) and down (dotted lines) B sweeps with different excitation currents. The curves were offset in R with respect to each other to make the structures more visible.	89
B.4	Hall resistance as a function of magnetic field for up (solid lines) and down (dotted lines) B sweeps. These curves were also shifted in R with respect to each other in order to make the structures visible. . .	90
B.5	Hall resistance vs magnetic field for up (solid B lines) and down (dotted lines) B sweeps for different driving currents between 0.05 mA and 10 mA on sample $x = 0.3$. The curves were offset with respect to each other to make the features visible.	91
B.6	Hall resistance (R_{yx}) vs R field for up (solid lines) and down (dotted lines) B sweeps and for $I=0.25, 0.5, 1, 2, 6, 10$ mA. The curves were also offset in R with respect to each other to make the structures visible.	92
B.7	Hall resistance vs magnetic field for up (solid lines) and down (dotted lines) B sweeps on sample $x = 0.4$. Curves were offset in R to make the features more visible.	93
B.8	R_{yx} vs B field for up (solid lines) and down (dotted lines) B sweeps with $I=0.5, 1, 2, 3, 5, 7$ mA. Curves were offset in R with respect to each other to make the structures more visible.	94
B.9	$V - I$ curves for a) NiZr_2 b) $\text{Fe}_{0.2}\text{Ni}_{0.8}\text{Zr}_2$ c) $\text{Fe}_{0.3}\text{Ni}_{0.7}\text{Zr}_2$ d) $\text{Fe}_{0.4}\text{Ni}_{0.6}\text{Zr}_2$.	95

LIST OF TABLES

3.1	Properties of samples $\text{Fe}_x\text{Ni}_{1-x}\text{Zr}_2$ for different x . $\ast\rho_N$ was measured at room temperature. The errors mainly come from measurements of the distance between the contacts. $\ast\ast$ Not measured, the values are assumed to be close enough to the other values found.	26
4.1	List of samples with some important results	50

Abstract

The mixed state of type II superconductors is an ideal medium for the study of correlated systems since the density of vortices which penetrate the sample, as well as the driving force, can be tuned such as to measure their effects on correlations. The weak pinning character of the $\text{Fe}_x\text{Ni}_{1-x}\text{Zr}_2$ metal glasses permits vortex phases to be probed by dissipative transport (longitudinal and Hall) measurements. The complete phase diagram in this regime is mapped out as a function of magnetic field, driving current and temperature using results from longitudinal resistance measurements. The longitudinal measurements show a huge peak effect with a driving force induced pinning phase known to arise from a disordering transition. The Hall resistance measurements lead to remarkable new results: a critical angle dependence of the vortex flow direction when entering or leaving the disordered phase is revealed, which suggests the existence of orientational phase transitions.

Résumé

L'état mixte des supraconducteurs de type II est un médium idéal pour l'étude des systèmes corrélés puisque la densité de vortex qui pénètrent l'échantillon, ainsi que la force sur ceux-ci, peuvent être ajustées dans le but de mesurer leurs effets sur les corrélations. Comme les vortex dans les verres métalliques amorphes de $\text{Fe}_x\text{Ni}_{1-x}\text{Zr}_2$ sont très faiblement pigés, les phases de vortex peuvent être explorées à l'aide de mesures de transport électrique (longitudinal et Hall). Le diagramme de phases dans ce régime est obtenu en fonction du champs magnétique, du courant et de la température. Les mesures longitudinales montrent un énorme 'peak effect' ainsi qu'une phase pigée induite par la force sur les vortex et qui émane d'une transition de désordre. Les mesures de résistance de Hall mènent à de nouveaux résultats qui révèlent une dépendance critique de l'angle de circulation des vortex à l'entrée et à la sortie de la phase désordonnée, et qui suggèrent l'existence de transitions de phases orientationnelles.

Acknowledgments

I would like to thank first and most importantly my supervisors Michael Hilke and Zaven Altounian without whom this work would not have been possible. I was extremely fortunate to have the chance to work on such an interesting and important project and their constant help and suggestions through every step was invaluable. Their enthusiasm toward this research was also greatly appreciated.

I am also indebted to Robert Gagnon, who throughout the entire course of this study was available for help and good advice. His aid in some experimental manipulations was sometimes much needed and his expertise in fixing things that broke was always greatly appreciated.

Finally, I would also like to give special thanks to Luis Valcárcel whose constant support proved to be of premier importance throughout my graduate studies. His devotion to the revision of my work, and particularly of this thesis was considerable and his suggestions were very helpful. Other special thanks go to my friends and co-workers Anne-Sophie Lucier and Sophie Avesque who made our working atmosphere so pleasant. I also thank the other members of my research group who were always available for help, and my parents Marcel and Ida Lefebvre for their unparalleled love and support.

Peak Effect, Hall Effect and Vortex Phases in
 $\text{Fe}_x\text{Ni}_{1-x}\text{Zr}_2$ Superconducting Glasses

INTRODUCTION

Since the discovery of superconductivity by H. Kamerlingh Onnes in 1911 [2], scientists never ceased dreaming about the fantastic applications which could be developed from this surprising resistanceless state of matter appearing when certain materials are cooled to a temperature below some critical value T_c . The complete disappearance of resistance in this state is astoundingly demonstrated by the presence of persistent currents in superconducting rings, which have been predicted to flow without measurable attenuation for over 10^5 years. A subsequent revelation by Meissner and Ochsenfeld [2] triggered a new wave of aspiration: superconductors do not only carry current without dissipation of energy, but are also perfect diamagnets. This means that the existence of a magnetic field in their interior is completely prohibited, and that the superconducting state can be controlled by an additional external parameter: magnetic flux. A stupefying demonstration of the diamagnetic property of superconductors is the levitation of a magnet over a superconducting material brought to a temperature below T_c .

However, more useful and tangible applications of superconductivity were only made possible after the discovery in the 1950's of a different type of superconductivity, which was simply called type II superconductivity. This new state, which shares the quality of type I superconductors of becoming resistanceless below a critical temperature, however exhibits a different and important character when it comes to its behavior in the presence of a magnetic field: it allows the penetration of a magnetic field in the form of flux tubes, or vortices, each carrying a quantum of flux. From a practical standpoint, the most useful attribute of type II superconductors

is that their critical field (the field above which superconductivity is destroyed) is substantially more elevated than that of type I superconductors, which permits the fabrication of superconducting solenoids able to supply steady fields of over 10 T without dissipation of energy. For the purpose of comparison, producing a comparable field using a water-cooled copper solenoid would generate a steady dissipation of 2 MW of power. In addition, this system would not have the essentially infinite stability of the superconducting magnet, and needless to say, would have eminent cooling problems.

In the late 1980's, the advent of a new class of superconductors having properties similar to those of type II superconductors, high- T_c superconductors (HTSC), spawned an all-new and promising field of research. In fact, the discovery of these copper oxide-based materials elevated the traditional ceiling $T_c = 23$ K in conventional superconductors to an incredible value over 134 K, such that the superconducting state could now be reached by merely using liquid nitrogen as a coolant, thereby reducing the degree of difficulty and the cost involved in the traditional use of liquid helium. In addition to this advantageous property, HTSC typically have much higher critical current densities and critical magnetic fields than their conventional analogue; an unprecedented critical field of 100 T has been reported in YBCO at 6 K.

Unfortunately, there is a limit to the true dissipationless state in superconductors of the second kind, which is brought by the presence of the flux tubes penetrating the material when it is placed in a magnetic field: if a current higher than some critical value is applied to a superconductor in the vortex state, a force will be induced on the flux tubes such that they will start moving. This motion of flux tubes will in turn generate an electric field in the superconductor, which means that it is not superconducting anymore! However, this rather bad onset of resistance in the vortex state can be avoided by pinning the flux tubes in place, thereby providing them with the ability to resist the force induced by the applied current and preventing them from moving; inhomogeneities or defects can act as such pinning sites.

In order to understand the mechanisms of flux pinning and vortex motion, we

propose to measure the magnetoresistance and the Hall resistance in a system with the weakest possible pinning potential, such that the flux flow regime is reached at conveniently low values of field and current. These resistance measurements are performed at constant temperatures below 400 mK as a function of magnetic field on high purity Fe-Ni-Zr based metal glasses which have a remarkably low critical current density J_c below 0.4 A/cm². In addition, this system exhibits the peak effect: an enhancement of the critical current just below the transition to the normal state; its origin is still under debate, but is generally associated with an order-disorder transition. The disorder-induced pinning phase, the “peak”, can even lead to a reentrant superconducting phase if all vortices get re-pinned. The peak effect is one of the most intriguing consequences of vortex motion and its occurrence in our superconducting metal glasses $\text{Fe}_x\text{Ni}_{1-x}\text{Zr}_2$ makes these systems ideally suited for the study of vortex dynamics and mechanisms of vortex motion. Furthermore, reports of Hall resistance measurements in the vortex state of type II superconductors are not common in the literature owing probably to the difficulty of making such measurements; the signal is particularly faint, typically $\sim \mu\text{V}$ in our low- J_c , and the assembly of suitable voltage probes is arduous. Such measurements are nevertheless worth the trouble because they offer a noteworthy additional probe for the study of vortex dynamics since Hall effects in superconductors are attributable to vortex motion.

This thesis will be divided in five main parts, which will be sequenced such as to provide the reader with a background on the subject before the experimental results are presented. A chapter describing the experimental techniques used in this research will also be included before the first presentation of experimental results. However, we start in chapter 2 with a presentation of some of the pioneering theories of superconductivity, and with a description of different phenomena associated with the peak effect. Then follows chapter 3 with a description of the fabrication technique used to make our samples and with an exposition of some of their properties. This chapter also contains a description of the apparatus and procedure used to performed the low temperature measurements. A presentation of our measurements of the magnetore-

sistance showing the peak effect in chapter 4 completes the first main part of this thesis. Then, chapter 5 comprises a description of the phenomenology of Hall effects in type II superconductors as well as an outline of a few theories developed on the subject. Finally, in chapter 6, the experimental observations of the Hall resistance in our superconducting samples are presented and comparisons with longitudinal resistance data are established in order to discuss and reach a ubiquitous agreement between these two different types of results.

THEORY OF SUPERCONDUCTIVITY

This chapter will be composed of two parts: the first section will provide the reader with a cursory glance at the most important theories of superconductivity; from the basic London equations to the more involved BCS theory. It is meant to give an idea of the fundamental phenomenology before discussing the main matter of this work: vortex dynamics. However, it is to be noted that the reader does not need to understand the formalism described in sections 2.1.1 to 2.1.6 in order to understand the issues discussed in the remainder of this work. The chapter will be concluded by a section on the peak effect; it will discuss its origins and mechanisms as well as various phenomena associated to it.

2.1 Basic Theory of Superconductivity

2.1.1 Basic Phenomenology

There are two traditional hallmarks of superconductivity: the first one, discovered by Kamerlingh Onnes in 1911 [2], is perfect conductivity; the complete disappearance of resistance in a small temperature range at a critical temperature T_c (usually a few Kelvins) in various metals. In fact, the conductivity in superconductors is so perfect that a current set up in a superconducting ring is expected to persist without any diminution for at least 10^5 years! The second hallmark of superconductivity is perfect diamagnetism, which was first observed in 1933 by Meissner and Ochsenfeld [2]. They found that magnetic fields are not only *excluded* from superconductors, but also that they are *expelled* from such originally normal materials upon cool down through T_c . This reversible Meissner effect is important as it implies the existence of a critical

field H_c for which superconductivity is destroyed and which is thermodynamically related to the free energy difference between the normal and superconducting state in zero field. Empirically, the temperature dependence of the critical field is fairly well approximated by a parabolic law $H_c(T) \approx H_c(0) \left[1 - \left(\frac{T}{T_c} \right)^2 \right]$. It is also worth noting that the transition at T_c is second order in zero field, but first order in the presence of a magnetic field due to a discontinuity in the thermodynamic state of the system.

2.1.2 The London Equations

In 1935, the brothers F. and H. London [3] described in two equations the above-mentioned electrodynamic properties of superconductors. In terms of the phenomenological parameter

$$\Lambda = \frac{4\pi\lambda_L^2}{c^2} = \frac{m}{n_s e^2}, \quad (2.1)$$

where n_s is the number density of superconducting electrons, m and c are respectively the mass of the electron and the speed of light, and λ_L is the London penetration depth which will be described in more detail later; the microscopic electric field is given by

$$\vec{E} = \frac{\partial}{\partial t} (\Lambda \vec{J}_s), \quad (2.2)$$

which describes perfect conductivity since it expresses that any electric field accelerates the superconducting electrons instead of sustaining their velocity against a resistance as in normal conductors. The magnetic field is given by

$$\vec{H} = -c \vec{\nabla} \times (\Lambda \vec{J}_s), \quad (2.3)$$

which, when combined with the Maxwell equation

$$\vec{\nabla} \times \vec{H} = \frac{4\pi \vec{J}}{c}, \quad (2.4)$$

results in a quantitative description of the Meissner effect, namely

$$\vec{\nabla}^2 \vec{H} = \frac{\vec{H}}{\lambda_L^2}. \quad (2.5)$$

Solving this equation for \vec{H} , one finds that the magnetic field decays exponentially from the surface of a superconductor over a characteristic length λ_L ; the London penetration depth.

A quantum motivation for the London equations involves the use of the vector potential \vec{A} and the canonical momentum $\vec{p} = m\vec{v} + e\vec{A}/c$. The derivation assumes that in the absence of an applied field, the superconducting ground state would have zero net momentum $\langle \vec{p} \rangle = 0$ such that the average velocity of superconducting electrons in the presence of a field is

$$\langle \vec{v}_s \rangle = -\frac{e\vec{A}}{mc}; \quad (2.6)$$

a relation which holds if one assumes rigidity of the superconducting electron wavefunction. Starting from this, one can express both London equations in a single one:

$$\vec{J}_s = n_s e \langle \vec{v}_s \rangle = \frac{-n_s e^2 \vec{A}}{mc} = \frac{-\vec{A}}{\Lambda c}, \quad (2.7)$$

which equals equation (2.2) if one takes the time derivative of both sides, while taking the curl yields equation (2.3). These results are valid in the so-called London gauge: $\vec{\nabla} \cdot \vec{A} = 0$.

However, an important question still remains unanswered: What is the maximum density of superconducting electrons? The natural upper limit is obviously the total density of conduction electrons n ; using this in equation 2.1, one gets an estimate of the limiting value as $T \rightarrow 0$ of the penetration depth

$$\lambda_L(0) = \sqrt{\frac{mc^2}{4\pi n e^2}}. \quad (2.8)$$

Obviously, the simple approach to superconductivity offered by the London theory is not exact and measured values of the penetration depth in superconductors always yield values which are larger than λ_L , even when extrapolated to $T = 0$, thus indicating an incomplete rigidity of the wavefunction such that $n_s < n$. A quantitative analysis also calls for the introduction of a new characteristic quantity: the coherence length ξ_0 .

2.1.3 Pippard Electrodynamics

Pippard [4] was the first to introduce the concept of the coherence length while working on a nonlocal generalization of the London equations. His work comes in analogy to Chambers' nonlocal generalization of Ohm's law [5]. Pippard suggested that the superconducting wavefunction should have a characteristic extent: the above-mentioned coherence length ξ_0 . His reasoning to get to an evaluation of ξ_0 begins with the deduction that only electrons within $\sim kT_c$ of the Fermi energy can possibly participate in a phenomenon occurring at T_c . Therefore, proceeding with conventional uncertainty-principle arguments $\Delta x \gtrsim \frac{\hbar}{\Delta p} \approx \frac{\hbar v_F}{kT_c}$ yields the following definition for the coherence length:

$$\xi_0 = a \frac{\hbar v_F}{kT_c}, \quad (2.9)$$

where a is a constant of the order of unity. ξ_0 can be described as a length analogous to the mean free path l in the nonlocal electrodynamics of normal metals. In order to express his ideas in a more concise form, Pippard proposed that the coherence length ξ in the presence of scattering should be related to that of the pure metal by

$$\frac{1}{\xi} = \frac{1}{\xi_0} + \frac{1}{l} \quad (2.10)$$

and that equation (2.7) should be replaced by¹

$$\vec{J}_s(\vec{r}) = -\frac{3}{4\pi\xi_0\Lambda c} \int \frac{\vec{R} [\vec{R} \cdot \vec{A}(\vec{r}')] e^{-R/\xi}}{R^4} d\vec{r}', \quad (2.11)$$

where $\vec{R} = \vec{r} - \vec{r}'$.

Pippard evaluated the value of the numerical constant a in equation (2.9) for tin and aluminum and found $a = 0.15$ for both; later, Bardeen, Cooper and Schrieffer (BCS) found a value of 0.18 [2]. The Pippard theory nonetheless fits the experi-

¹Notice the analogy with Chambers' generalization of Ohm's law:

$$\vec{J}(\vec{r}) = \frac{3\sigma}{4\pi} \int \frac{\vec{R} [\vec{R} \cdot \vec{E}(\vec{r}')] e^{-R/l}}{R^4} d\vec{r}'.$$

mental data to great accuracy and anticipates the form of the electrodynamics of the microscopic theory which was found only years later.

2.1.4 Results from the BCS Theory and the Superconducting Energy Gap

The next key step in the development of the theory of superconductivity was the determination of the existence of an energy gap between the ground state and the excited state of the strongly interacting particles which compose the superconducting state (quasi-particle excitations). The size of the gap was predicted to increase from 0 at T_c to a limiting value of

$$E_g(0) = 2\Delta(0) = 3.528kT_c \quad (2.12)$$

as $T \rightarrow 0$. Of equal importance at about the same epoch was the proposition by Cooper that the excitations were always produced in pairs. In fact, BCS [6] showed that even a slight attractive interaction between electrons, such as the one caused by the interaction of the electrons with the phonons, would be enough to bind two electrons together in a pair: the Cooper pair. The electrons occupying the pair would have opposite momentum and spin and would have spatial extent ξ_0 . The minimum energy required to break such a pair was predicted to be $E_g = 2\Delta(T)$.

The BCS theory will not be presented in further details in this work since an elaborate knowledge of this microscopic treatment of superconductivity is not required to understand the phenomenology of the data which will be presented. Moreover, a thorough presentation of this subject alone would require a whole book in order to give it the credit it's due!

2.1.5 The Ginzburg-Landau Theory

A *chef-d'oeuvre* of ingenuity which followed the advent of the BCS theory was the theory of superconductivity by Ginzburg and Landau (GL) [7], which treats a totally different aspect of superconductivity: the superconducting electrons rather than the

excitations as the BCS theory does. In this theory, a complex pseudo-wavefunction Ψ is introduced as an order parameter for the superconducting electrons, thus giving for their density

$$n_s = |\Psi(x)|^2. \quad (2.13)$$

Then, a differential equation for Ψ can be derived from variational principles and assuming an expansion of the free energy in powers of Ψ and $\nabla\Psi$, and expansion coefficients α and β gives

$$\frac{1}{2m} \left(\frac{\hbar}{i} \vec{\nabla} - \frac{e^*}{c} \vec{A} \right)^2 \Psi + \beta |\Psi|^2 \Psi = -\alpha(T) \Psi. \quad (2.14)$$

The equation for the supercurrent is then

$$\vec{J}_s = \frac{e^* \hbar}{2im} (\Psi^* \nabla \Psi - \Psi \nabla \Psi^*) - \frac{e^{*2}}{mc} |\Psi|^2 \vec{A}. \quad (2.15)$$

Notice the similarities between equation (2.14) and the Schrödinger equation for a free particle; equation (2.15) is the same as the usual quantum-mechanical one for particles of charge $e^* = 2e$ and mass m .

The advantages of this formalism over the London theory are that it not only permits the treatment of nonlinear effects in fields strong enough to change the superconducting electron density n_s , but also allows for spatial variations of n_s . Though, the key triumph of the theory lies in its capacity in treating situations close to H_c , in which both superconducting and normal domains coexist, namely the intermediate state.

This theory also relies on both characteristic lengths already introduced, λ and ξ , though ξ is now changed to the temperature-dependent

$$\xi(T) = \frac{\hbar}{|2m^* \alpha(T)|^{1/2}}, \quad (2.16)$$

which now sets the scale for spatial variations of the order parameter Ψ . The ratio of these two characteristic lengths is

$$\kappa = \frac{\lambda}{\xi} \quad (2.17)$$

which defines the GL parameter. Typical values for the characteristic lengths are $\lambda \approx 500 \text{ \AA}$ and $\xi \approx 3000 \text{ \AA}$, such that usually $\kappa \ll 1$. This value of κ serves in determining the sign of the surface energy between superconducting and normal domains in the intermediate state. In fact, a cutoff was found such that for $\kappa < 1/\sqrt{2}$, the surface energy is positive, while if $\kappa > 1/\sqrt{2}$, one has a negative surface energy, in which case it becomes energetically favorable for magnetic flux to penetrate a superconductor and form intermingled regions of superconducting and normal material. Superconductors for which this happens are called *type II* (the other ones are *type I*); their particularities will be discussed in the next section.

2.1.6 Type II Superconductivity

Abrikosov [8] published in 1957 a remarkable theory which dealt with systems in which $\kappa > 1/\sqrt{2}$: type II superconductors. Contrary to type I superconductors, type II superconductors allow a continuous increase in flux penetration, starting at a first critical field H_{c1} up to an upper critical field H_{c2} . This critical field H_{c2} can be much greater than the critical field H_c in type I superconductors, a property which is found to be very convenient for the making of high-field solenoids for instance.

Another finding attributable to Abrikosov is that in the state between H_{c1} and H_{c2} , the magnetic field enters the superconductor under the form of a regular array of flux tubes, each carrying a quantum of flux $\Phi_0 = \frac{hc}{2e}$. These flux tubes are basically vortices of supercurrent concentrating the flux in the center of the tube. It follows from this that type II superconductors are obviously not perfect diamagnets, but neither are they perfect conductors; a surprise comes along with the existence of these flux tubes: if a current is applied on such a vortex filled sample, the vortices will start moving under the action of the Lorentz force, thus inducing an electric field in the sample, which means that it is no longer superconducting! Fortunately, this readily happens only in very homogeneous samples in which only a viscous drag opposes vortex motion. In real samples, there are always some inhomogeneities present in the superconductor which serve as pinning sites for the vortices, such that they only

start moving once the Lorentz force overcomes the pinning force. The subjects of pinning, vortex motion and related phenomena will be treated in the remainder of this work.

2.1.7 Dynamics of Vortices

Flux Flow

As mentioned in section 2.1.6, the presence of moving vortices in a type II superconductor induces an electric field in the sample, such that a finite resistance can be measured. A schematic representation of this situation is shown in Figure 2.1, in which one sees that upon application of a current density \vec{J} to the superconductor in a magnetic field perpendicular to its surface, a force (the Lorentz force)

$$\vec{F}_L = -\vec{J} \times \frac{\vec{\Phi}_0}{c} \quad (2.18)$$

(the minus sign comes from the fact that it is the direction of motion of the electrons which is important, not the direction of conventional current) is induced on a vortex such that vortex motion is actuated in a direction perpendicular to the applied current. An electric field

$$\vec{E} = \vec{\Phi}_0 \times \frac{\vec{v}}{c} \quad (2.19)$$

is then induced from this vortex motion in a direction anti-parallel to the current; this electric field acts as a resistive voltage such that power is dissipated. If pinning is weak compared to the driving force, the vortices will move in a rather steady fashion; this regime in which only a viscous drag limits the velocity of the vortices is called “flux flow”. The “flow resistance” is comparable to the resistance of the material in the normal state such that for practical applications, flux flow must be avoided. However, weakly pinned superconductors in which the flux flow regime is attained at low current densities are ideal systems for the study of the mechanisms of vortex motion.

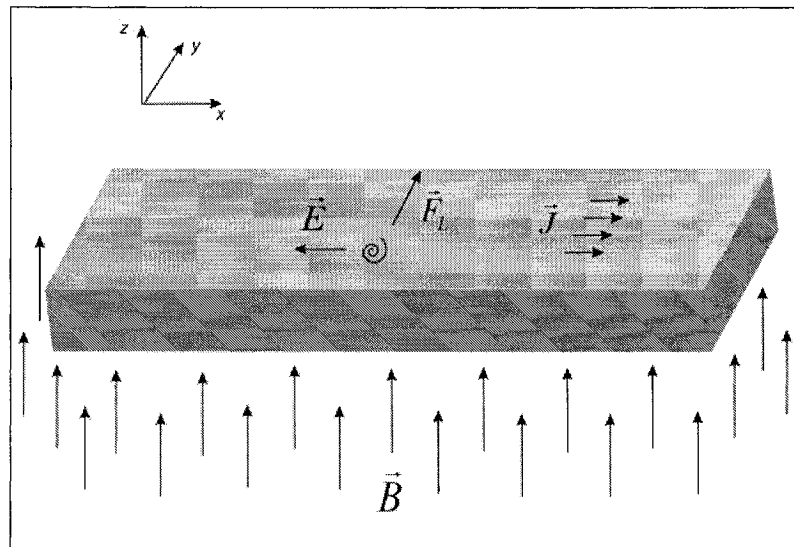


Figure 2.1: Schematic representation of the force induced on a vortex when a current is applied to the superconductor. The moving vortex then induces an electric field in the direction antiparallel to the current.

Flux Pinning

In order to avoid vortex motion, a mechanism must exist such that the vortices are “pinned” at specific locations in the material; the force acting on the vortices from this pinning action would oppose the Lorentz force and vortex motion would be prevented until the Lorentz force would overcome the opposing force. Fortunately, such a force exists; it is called a pinning force and arises from the presence of any spatial inhomogeneities in the material. This is so because local variations of ξ , λ , or H_c due to impurities, grain boundaries, voids or any defect will cause local variations of the free energy of a flux line, thereby causing some locations of the vortex to be favored over others. These inhomogeneities, if of typical size ξ or λ will be most effective at pinning vortices; atomic scale inhomogeneities which cause electronic scattering only limit the mean free path l .

Flux Creep

Pinning can typically be made sufficiently strong such that vortex motion is mostly avoided and the superconductor acts like a perfect conductor. However, at finite temperatures, thermal energy always leads to a phenomenon called “flux creep” by

which the vortices hop from one pinning site to another with an associated and unwanted dissipation of energy . This creep rate is sometimes measurable, but it is typically unobservably slow; velocities of the order of 10^{-7} cm / s have been measured. However, since any creep that occurs will relieve the flux-density gradient, the creep rate will get slower and slower; the time dependence is logarithmic such that as much creep takes place between 1 and 10 seconds as between 1 and 10 years. Therefore, flux creep is more than often negligible.

2.2 *The Peak Effect*

The peak effect, a very puzzling phenomenon, is an anomalous enhancement of the critical current observed just below the critical transitions (T_c and B_{c2}) in the vortex state of some low- T_c type II superconductors. This anomaly in the current response of certain superconductors was observed for the first time about 40 years ago and is still the subject of ongoing research. It has been accepted for some time now that this phenomenon is the signature of a transition from the quasicrystalline Bragg glass phase into a highly disordered phase above T_p , the temperature at which the peak appears. The Bragg glass is a phase in which crystalline order is destroyed by the presence of impurities. Even though this phase is a glass, it is nearly as ordered as the crystalline phase, being described by a power-law decay of the crystalline order. In addition to the sudden increase in critical current, several perplexing phenomena associated with the peak effect are observed, which include: history and geometry-dependent dynamic response, suppression of the AC response by a small DC bias and high vortex mobility for alternating current but no apparent vortex motion for direct currents. This section will describe some characteristics of the vortex lattice and phenomena associated with the peak effect.

2.2.1 *Early Hypothesis*

The early study of the peak effect phenomenon by Larkin and Ovchinnikov[9] suggested that this sudden increase in the critical current J_c just below B_{c2} could be

attributed to a pinning-induced transformation from an ordered to a disordered vortex phase. The proposed scenario is the following: the pinning force is given by

$$F_p = J_c B = \sqrt{\frac{n_p \langle f_p^2 \rangle}{V_c}}, \quad (2.20)$$

where n_p and f_p are the density and strength of pins respectively. $V_c = R_c^2 L_c$ is the volume of the correlated region; $R_c = \frac{c_{44}^{1/2} c_{66}^{3/2} r_f}{n_p \langle f_p^2 \rangle}$ is the transverse correlation length, and $L_c = R_c \sqrt{\frac{c_{44}}{c_{66}}}$ is the longitudinal correlation length, which depend on c_{66} ² and c_{44} ³ respectively the shear and tilt moduli, and r_f the pinning range. These correlation lengths determine the length scale over which the flux line lattice (FLL) is correlated. The moduli correspond to different elastic constants which increase the elastic energy of the FLL [2]. This elasticity of the FLL is essential for any effective pinning of the FLL because it allows the paths of individual flux lines to deviate from an ideal periodic lattice, and thus lower their energy by passing through a favorable pinning site. Also, a sudden enhancement of the squared elementary interaction averaged over a lattice cell is ruled out as a cause for the peak effect, being a property of individual vortices [11]. This leaves the possibility that the peak effect results from the rapid collapse of V_c , i.e. an amorphization of the lattice; this is the theory accepted presently [11, 12]. This loss of order was observed in neutron diffraction experiments as the loss of Bragg intensity upon increase of the temperature through the peak effect [13, 14]. However, this leaves an important question open: what mechanism causes this transformation in the ordering of the FLL?

2.2.2 Sample Purity Effects

The degree of purity of samples is known to affect greatly the characteristics of the peak effect. This is so because the degree of purity influences directly the pinning

$${}^2 c_{66} \approx \frac{B_{c2}^2}{\mu_0} \frac{b(1-b)^2}{8\kappa^2} \left(1 - \frac{1}{2\kappa^2}\right) (1 - 0.58b + 0.29b^2) [10]$$

where $b = B/B_{c2}$ and κ is the GL parameter.

$${}^3 c_{44} \approx \frac{B^2}{\mu_0} \quad (\text{for small } b)$$

$$c_{44} \approx \frac{B^2(1-b)}{\mu_0 \kappa^2} \quad (\text{for } b > 0.5) [11]$$

strength of the material; high-purity samples have a weaker pinning potential. For instance, experiments on the low- T_c , weakly-pinned system 2H-NbSe₂ showed [12] that higher-purity samples show sharper and narrower peaks in critical current as a function of temperature. Moreover, an important dependence on the thermomagnetic preparation history is found in dirty (larger pinning strength) samples: a sample cooled in zero-magnetic field typically shows a wide peak effect, while a sample cooled in a magnetic field shows no peak at all, indicating that the vortices remain pinned up to the upper critical field. An explanation for this is that in the field-cooled state, further disordering with increasing temperature could be absent since this metastable state is already highly disordered. Therefore, the zero-field-cooled and the field-cooled states represent two distinct metastable states of the vortex system, most likely with different correlation volumes since they have different J_c 's, and also because neither f_p nor n_p , being microscopic quantities, can depend on the history of the system. No such history dependence is observed in the highest-purity (most weakly pinned) samples, thus indicating that this is really a consequence of the degree of pinning.

Considering these effects caused by the degree of purity of the samples on the shape of the peak, the proposed mechanism for the onset of the peak is as follows: in the region below the peak, the solid is relatively well ordered, akin to a Bragg glass, and is elastically deformed. This Bragg glass phase has the attributes of a standard glass phase according to its dynamical properties, but in addition possesses perfect topological order [15] (no defects or dislocations, unlike the usual naive picture of a glass as a very scrambled system). The equilibrium flux-line configuration is the distorted arrangement which minimizes the sum of elastic and pinning energy [2], and the Bragg glass phase is a regime in which elastic energy surpasses both pinning and thermal energy. But with increasing temperature, elastic energy decreases at a larger rate than pinning, until the point where pinning overcomes elastic energy; this is the onset of the peak effect. At this point, the system suffers a transition into a glassy state full of topological defects. Then, in the region between the onset of the

peak effect and the peak itself, the increased disorder stabilizes the imperfect glassy phase, as inferred by the broadening of the peak with the degree of pinning. In fact, if the degree of pinning is augmented, pinning energy overcomes elastic energy at progressively lower temperatures, and the width of the stable disordered vortex glass phase expands. Ultimately, at the position of the peak T_p , thermal energy overcomes elastic energy and the FLL enters an even more disordered amorphous state. In the absence of pinning, this state would be equivalent to a vortex liquid.

2.2.3 Current and Vortex Distribution

In the standard strip geometry, the vortices enter the sample from one edge and leave at the other edge; an action which requires a large force in order to overcome the surface barrier. In addition, this surface barrier is non-uniform due to its great sensitivity to surface imperfections; this induces a non-uniform entry and exit of vortices through the surface. The presence of weaker points on the barrier facilitates the injection of vortices there, causing a non-homogeneous distribution of vortices at the sample edge. Therefore, a more important part of the current applied to the sample should flow at the edges in order to provide the driving force necessary to overcome the surface barrier [16, 17]. This applied current then has the effect of injecting a metastable disordered vortex phase at the sample edge, whereas the current flowing in the bulk serves as an effective temperature and anneals the metastable phase. Hence, the special phenomena associated with the peak effect, such as memory of the previous history must arise from a delicate balance between these two competing processes.

2.2.4 AC vs DC Driving Current

The nature of the driving current, AC or DC, has an influence on the size of the metastable phase at the onset of the peak effect. This disordered phase is extremely unstable, and in the presence of a driving force its relaxation time τ_r is very brief, so that it rapidly anneals over a characteristic length $L_r = \nu\tau_r$, where ν is the vortex lattice drift velocity. Upon annealing, the current density is expected to decay from

J_c^{dis} , the critical current density in the disordered state, to J_c^{ord} the critical current density in the ordered state, over the characteristic length L_r . When approaching the peak effect, the free energies of the disordered and the ordered phase become comparable, such that τ_r and L_r increase. This means that J_c^{dis} will now decay to J_c^{ord} over a larger distance from the sample edge, *i.e.* it allows the front of the disordered phase to penetrate more deeply into the bulk. From this, it is concluded that the region below the peak effect is not at equilibrium for a DC driving current, but is rather a dynamic coexistence of two phases [18].

Alternatively, if the driving force is provided by an AC current, the contamination of the sample takes place only periodically and close to the edges. The positive half cycle contaminates the left edge of the sample with a disordered vortex lattice to some depth, while during the negative half cycle, this disordered phase leaves the left edge and a disordered phase on the right enters. The effect of this on the peak was observed in Ref. [16, 19, 20] in critical current I_c vs T measurements as a steeper increase of I_c toward the peak upon application of an AC current; as opposed to the smooth onset of the peak observed in the presence of a DC drive. This is an evidence that in the presence of an AC drive, the vortices contaminate the sample to a less significant degree than upon application of a DC current. It is also observed that the contaminated depth decreases with increasing frequency of the applied AC current leading to steeper onsets of the peak. The smooth behavior of the I_c^{dc} curve at the onset of the peak effect reflects the dynamic coexistence of the ordered and disordered vortex phases, while the abrupt increase of I_c^{ac} at high frequency indicates a sharper transition between the ordered and the disordered phases.

2.2.5 Changing the Sample Geometry

The results described previously point to the conclusion that the discrepancy between the behavior of the edge and the bulk of a sample could be a key to the determination of the underlying nature of the peak effect. As previously described, experiments in the standard strip geometry allow vortex contamination of the edges by the vortices, such that a disordered phase is present at the sample surface. As will be described

here, experiments in the Corbino disk geometry [19], shown in Figure 2.2, yield observations of the peak effect under conditions such that the injections of vortices at the sample surface is suppressed. In fact, the radial current drives the vortices in circle around the disk so that no edge is crossed, and voltage differences are measured along the radius of the disk. Therefore, since the Corbino disk geometry does not allow vortices to cross the edges, if the peak effect is a bulk phenomenon, then no significant difference is expected between the two geometries. However, one expects a qualitatively different behavior to be witnessed if the edges indeed play a significant role in this disorder-driven transition.

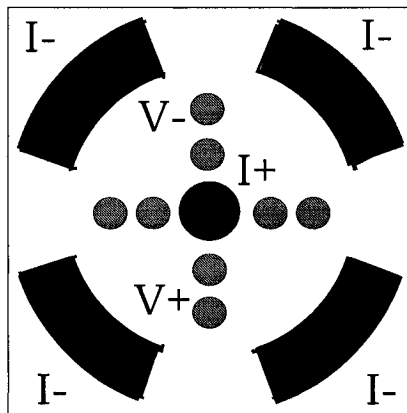


Figure 2.2: Electrode configuration for measurements in the Corbino disk geometry. The red electrodes are the voltage probes and the black ones serve to supply current.

Results have shown [19] that peak effect measurements in the Corbino disk geometry yield a very sharp increase of the critical current as a function of temperature at the onset of the peak; even sharper than that witnessed with a high-frequency AC driving current. Therefore, these results also point to the conclusion that the region below the peak is a coexistence phase of an ordered and a disordered solid, the disorder being due to the entry of vortices from the sample edges. In the Corbino geometry, in which the entry of vortices by the edges is practically prohibited, the transition between the ordered phase and the disordered phase is so sharp that the coexistence region is virtually non-existent, thereby establishing the role of the edge and bulk in the peak effect phenomenon.

2.2.6 Superposing an AC Current to a Small DC Bias

The superposition of an AC current to a small DC bias in measurements of the peak effect again stress the curious interplay between edge and bulk effects in these superconductors. It is observed [16] that a DC bias of only 10% to 20% of I^{ac} decreases (increases) the response $R^{ac}(I_c^{ac})$ by orders of magnitude. The mechanism for this phenomenon embeds perfectly with the edge contamination mechanism proposed earlier. In fact, a small DC bias contaminates the sample in the same manner as the pure DC case does, though with the addition of an AC current, the vortices now move back and forth in and out of the sample during the AC cycle, but with a net forward displacement due to I^{dc} . That is to say, the vortices drift deeper into the bulk, and as I^{dc} augments, the bulk becomes more and more contaminated and a sharp drop in R^{ac} is observable.

2.2.7 The Phase Diagram

In the absence of a driving force, the phase diagram for such periodic system as the vortex lattice is the static one presented in Ref. [21] for disorder strength as a function of temperature. One finds at finite disorder strength a transition between a pinned phase, called the Bragg glass phase, and the amorphous vortex glass at larger disorder strength. The Bragg glass phase has quasi-long range order and no topological defects; it is as good as a perfect lattice as far as translational order is concerned and shows Bragg peaks in neutron diffraction experiments [13]. On the other hand, the vortex glass is characterized by the presence of dislocations.

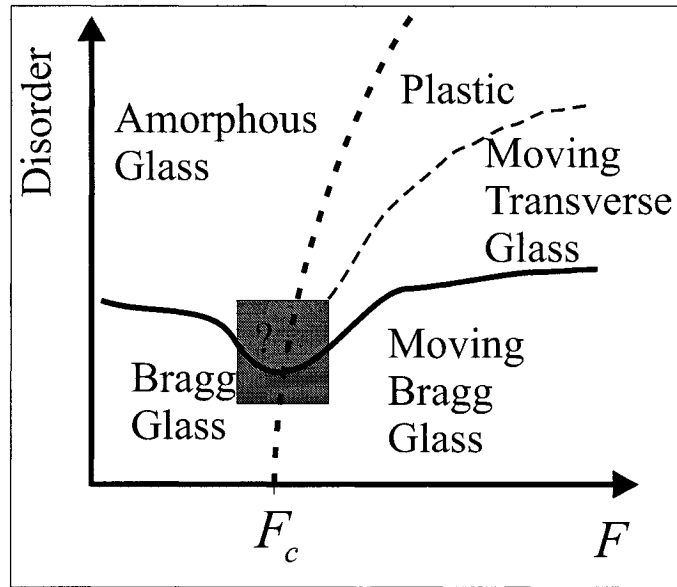


Figure 2.3: Schematic phase diagram of disorder *vs* force F at $T = 0$. The exact shape of the boundaries between the phases is still not known. The red square is a region in which the behavior is unclear. (Drawing adapted from Ref.[1])

The phase diagram for driven lattices in the presence of disorder is predicted in Ref. [1], and shown schematically in Figure 2.3 for disorder as a function of driving force. Upon application of a force greater than some critical force F_c , the Bragg glass survives motion by becoming simply the moving Bragg glass (MBG), which is characterized by static channels in which the vortices flow (see Figure 2.4(a)). These channels are determined by the static disorder and do not fluctuate in time; they are the easiest paths the particles can follow without undue dissipation and are thus the result of a subtle competition between elastic energy, disorder, and dissipation. Also, the channels are rough, not perfectly straight as would be expected for a perfect lattice. In particular, the MBG phase corresponds to a full elastic coupling between the particles in different channels, which despite the rough nature of the channels, the phase retains topological order.

Still for $F > F_c$ but for larger disorder strength, one finds the moving transverse glass (MTG) (see Figure 2.4(b)) again characterized by channels as the MBG, though now corresponding with the position of particles in different channels being decoupled.

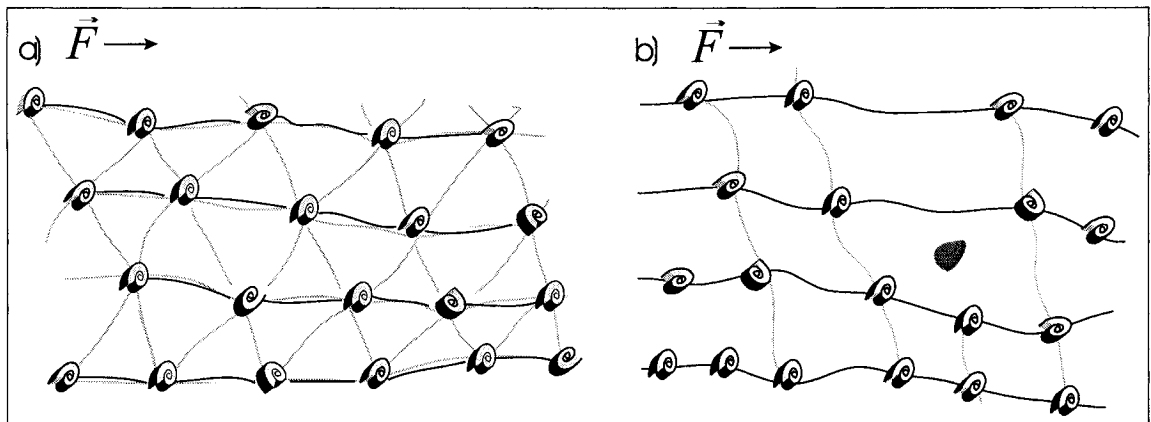


Figure 2.4: Schematic representation of the vortex lattice in the a) moving Bragg glass (MGB) phase and b) the moving transverse glass (MTG) phase. The blue lines represent coupling between the vortices whereas the black lines are the channels in which the vortices move. In b) the presence of defects (in red) causes the positions of vortices in different channels to decouple.

Dislocations are also present beyond a certain length scale R_d such that the lattice now has a smectic topological order. Upon increasing the disorder again, one finds a phase characterized by plastic flow of vortices. This filamentary motion proceeds via plastic channels between pinned regions, which are fundamentally different in nature from the channels in the MGB and the MTG. Despite numerous investigations, a detailed theoretical understanding of this regime is still skimpy.

Going back to the regime in which $F < F_c$, but now for large disorder strength, one finds the so-called amorphous glass or vortex glass of the static case, the nature of which remains unclear, though it must contain topological defects.

EXPERIMENTAL TECHNIQUES

This chapter will present the details of the experimental methods employed for this study. To this end, a description of the method by which the $\text{Fe}_x\text{Ni}_{1-x}\text{Zr}_2$ samples were prepared will first be presented along with a report of some of their properties. Then will follow a presentation of the apparatus used for the low-temperature measurements and a short explanation of its working principles. A discussion of the systematic errors which have to be considered in the analysis will conclude this chapter.

3.1 *Samples*

The preparation of amorphous materials requires the rapid cooling of the melted material; a rate of cooling of 10^5 K/s is typically needed. As this requirement is arduously fulfilled, the preparation of amorphous materials was quite limited before the 1980's, such that before this epoch, the study of superconducting materials more than often involved crystalline samples. Unfortunately, crystals typically have a high critical current due to the long-range order, and thus exhibit strong collective pinning. This forces one to use a perhaps large current before any flow of vortices can take place, such that the linear magnetoresistive behavior considered in the idealized theory can not be probed. Moreover, these assets make the investigation of the pinning and depinning mechanisms of the flux line lattice more difficult and less enlighting such that this facet of superconductivity remained obscure long after its discovery. On the other hand, the lower critical currents typical of amorphous superconductors permit a more interesting study of the dynamics of the flux line lattice. The samples used in this study are Fe-Ni-Zr-based superconducting metal glasses, which due to

their high purity have a very weak pinning potential and critical current density ($J_c \leq 0.4 \text{ A/cm}^2$) about 100 to 1000 times smaller than materials used in previous similar studies [22, 23, 24, 25, 26]. Other similar studies also involving amorphous films [27, 28, 29, 11] still have critical current densities which are 10 times larger than ours, confirming the high purity of our materials.

3.1.1 Sample Preparation

The alloys were prepared by arc melting appropriate amounts of high-purity starting materials (99.99% pure Zr, 99.999% pure Fe and Ni) under titanium-gettered argon atmosphere to avoid contamination from oxygen traces. The crystalline buttons of alloys were re-melted several times to ensure homogeneity. Then, melt-spinning techniques were used to obtain metal glasses.

As mentioned above, in order to make amorphous materials, one principally needs a technique to cool the material extremely quickly, typically $\sim 10^5 \text{ K/s}$; such a cooling rate is provided using the technique of melt-spinning, which involves the cooling of a substance by propulsion onto the rim of a rapidly spinning copper wheel. As shown in Figure 3.1, the buttons of alloys are placed in a quartz tube which has a small orifice at the bottom. The alloys are then heated to a temperature no higher than 150 K above their fusion temperature. Once the alloy is liquefied, it is propelled through the aperture at the bottom of the tube onto the rim of a copper wheel with a tangential velocity of about 50 m/s, which allows it to cool at the desired rate of $10^5 - 10^6 \text{ K/s}$. To minimize oxidation effects, the melt spinning was done at a pressure of 50 kPa of helium. The samples produced are long ribbons of metal glass about 1.0 mm wide and 20 μm thick. The amorphous nature of the samples was verified by x-ray diffraction, and confirmed by the absence of Bragg peaks.

3.1.2 The Clean and Dirty Limits

The clean and dirty limits of superconductors are characterized by the ratio of the mean free path l to the coherence length of the pure material ξ_0 [30]. Superconductors

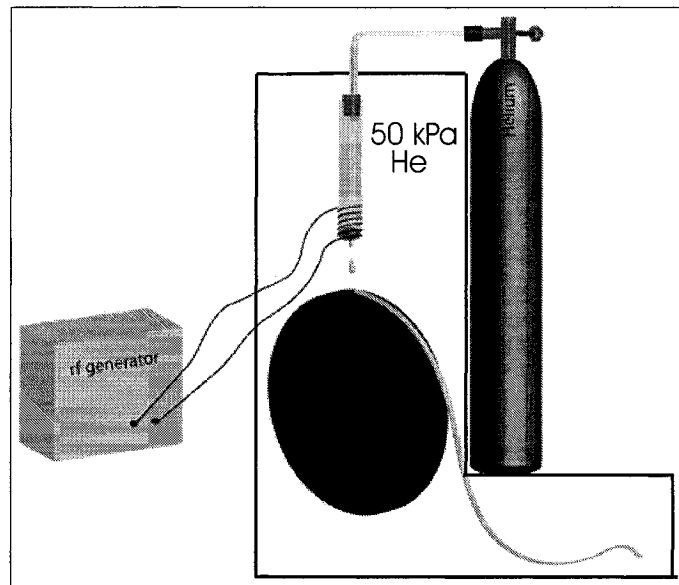


Figure 3.1: Schematic representation of the apparatus for sample preparation by melt-spinning.

in the clean limit have $\frac{l}{\xi_0} \gg 1$, while superconductors in the dirty limit have $\frac{l}{\xi_0} \ll 1$. However, when impurities are considered, the coherence length is dependent on l , such that an effective coherence length $\xi(l)$ can be defined as

$$\frac{1}{\xi(l)} = \frac{1}{\xi_0} + \frac{1}{l}. \quad (3.1)$$

Therefore, as l becomes shorter, $\xi(l)$ becomes shorter as well such that in the dirty limit:

$$\xi(l) = l, \quad (3.2)$$

and in the clean limit:

$$\xi(l) = \xi_0. \quad (3.3)$$

It is to be noted that equations 3.2 and 3.3 are valid only at $T = 0$, but even at higher temperatures, a decrease in l means that the superconductor becomes more impure.

3.1.3 Some Length Scales and Physical Properties

The different length scales characterizing our superconducting samples were estimated from standard expressions for superconductors in the dirty limit [28]. The zero

temperature penetration depth λ is obtained from

$$\lambda = 1.05 \times 10^{-3} \left(\frac{\rho_N}{T_c} \right)^{1/2} \quad (3.4)$$

where ρ_N is the normal state resistivity and T_c is the critical temperature. The BCS coherence length ξ_{BCS} ensues from

$$\xi_{BCS} = \frac{1.81 \times 10^{-8}}{\sqrt{T_c S}} \quad (3.5)$$

in which S is obtained from the slope of B_{c2} vs T at T_c , namely $S \equiv -\frac{dB_{c2}}{dT}|_{T_c}$, and the GL coherence length ξ_{GL} is

$$\xi_{GL} = \left(\frac{\Phi_0}{2\pi B_{c2}} \right)^{1/2} \quad (3.6)$$

where $\Phi_0 = \frac{h}{2e}$ is the flux quantum. Also, the GL parameter can be obtained from

$$\kappa = 3.54 \times 10^4 (\rho_N S)^{1/2}. \quad (3.7)$$

The values of these length scales for our $\text{Fe}_x\text{Ni}_{1-x}\text{Zr}_2$ samples are presented in Table 3.1 and are found to be typical of strong type II superconductors.

x	ρ_N ($\mu\Omega m$)	B_{C2} (T)	T_C (K)	$\frac{dB_{c2}}{dT} _{T_c}$ (T/K)	λ (μm)	ξ_{BCS} (nm)	ξ_{GL} (nm)	κ
0	$1.3 \pm 0.1^*$	4.8 ± 0.1	1.9 ± 0.1	$-2.7 \pm 0.2^{**}$	0.9	8.1	8.3	66
0.1	1.4 ± 0.1	5.5 ± 0.1	2.72 ± 0.05	$-2.7 \pm 0.2^{**}$	0.8	6.7	7.7	69
0.15	1.5 ± 0.1	4.7 ± 0.1	1.72 ± 0.08	-2.7 ± 0.2	1.0	8.4	8.4	71
0.2	2.1 ± 0.2	3.9 ± 0.1	1.54 ± 0.05	$-2.7 \pm 0.2^{**}$	1.2	8.9	9.2	84
0.3	1.6 ± 0.1	4.0 ± 0.1	1.53 ± 0.01	-2.7 ± 0.2	1.1	8.9	9.0	74
0.33	1.3 ± 0.1	3.6 ± 0.1	1.60 ± 0.03	$-2.7 \pm 0.2^{**}$	1.0	8.7	9.7	66
0.4	2.1 ± 0.1	3.5 ± 0.1	1.43 ± 0.03	-2.7 ± 0.2	1.3	9.2	9.7	84

Table 3.1: Properties of samples $\text{Fe}_x\text{Ni}_{1-x}\text{Zr}_2$ for different x . $^*\rho_N$ was measured at room temperature. The errors mainly come from measurements of the distance between the contacts. ** Not measured, the values are assumed to be close enough to the other values found.

3.1.4 Structural Relaxation

The attentive reader will have noticed that the T_c values found in Table 3.1 are significantly lower than expected for such materials. Specifically, for NiZr₂, $T_c > 2.8$ K was expected [31]. Moreover, a linear decrease of T_c with increasing iron content was expected, with NiZr₂ having the highest T_c ; instead, we find a T_c lower for NiZr₂ than for Fe_{0.1}Ni_{0.9}Zr₂, which is unusual since the introduction of iron is known to suppress superconductivity. The explanation for the too low T_c values found here is that these samples could contain an important amount of oxygen, which is known to lower T_c [32]. The amount of oxygen in the samples should have been verified prior to cool down, such that low-oxygen containing samples could have been chosen.

The reason why the T_c values are not comparable for samples with different iron concentrations pertains to the fact that the as-made ribbons have various states of structural relaxation. In order to understand what structural relaxation is in a sample, we can compare it to the real life situation of throwing balls in a bucket: if you leave the balls at the positions they initially fell in, there will probably be holes between the balls. On the other hand, if you shake the bucket slightly, the balls will move such as to fill those holes and the structure of the balls in the bucket will be more compact. Therefore, if the samples are not fully relaxed, they might have different amounts of strain fields and a non-uniform distribution of voids which make them incomparable. Structurally relaxed samples typically show a T_c which is about 10 % lower [32] than the T_c of not fully relaxed samples, but at least they can be compared with each other. Structural relaxation could have been attained by heating the samples to a temperature about 50 K below their crystallization temperature; however this was not done because it is known that this process sometimes makes the samples become brittle, such that the soldering of contacts to them is made much more difficult because the samples tend to break. Moreover, even if the sample does not break during attachment of the contacts, it will often break during the cool down process, thus decreasing significantly the success rate of experiments. This is the reason why this research does not present an exhaustive study of the evolution of T_c ,

or H_{c2} values as a function of the concentration of iron in the samples; these are not meaningful for not fully relaxed samples.

3.1.5 *Addition of Electrical Contacts to the Samples*

An issue also worth discussing is the attachment of ohmic contacts to the samples, as required for subsequent low temperature measurements in the ^3He system. The conventional method of soldering indium contacts was used, even though it involves many challenges due for instance to the small size of the samples, and to the presence of an oxide layer on their surface. The oxide layer could have been removed by bathing the samples in a mixture of strong acids; however this was not done for the samples presented here because it changes some of the properties of the samples such as the T_c values, due to the introduction of hydrogen into the sample. Furthermore, by soldering the electrical contacts, one is faced with another eminent problem; the procedure can introduce an important heating of the sample if the In is overheated, and though localized, this heating should suffice to partly crystalize the region neighbouring the contacts. In the case of the longitudinal resistance, the contacts used for the measurements are sufficiently far apart for the effect of the crystalized region to be insignificant, thus not affecting the measurements. On the other hand, the two Hall probes, being located on a width of about 1mm will be greatly surrounded by this crystalized phase; the Hall resistance results will thus most probably be seriously affected. This issue will be addressed in more detail in section 3.2.3.

3.2 *Experimental Setup*

The experiments were performed in a ^3He system with a base temperature of 300 mK. A superconducting magnet provided magnetic fields up to 9 T. The schematics of the apparatus are shown in Figure 3.2. The sample is placed in the main chamber of the ^3He system, which is then brought to high vacuum, typically $P \sim 2 \times 10^{-7}$ mbar during data acquisition. The ^3He insert is lowered into the cryostat, which is

filled with liquid helium. The design is such that the sample is located exactly in the middle of the superconducting coil, and is thus subject to a uniform and known magnetic field.

3.2.1 Components and Operation of the ^3He Insert

The components described in this section refer to the drawing of the ^3He insert in Figure 3.2. The Helium-3 reservoir contains the gaseous ^3He prior to cool down. ^3He liquefies at $T = 3.2$ K and in order to get to temperatures below 1.5 K, the vapor pressure of the condensed ^3He needs to be lowered; this is done with the sorbtion pump. The 1K pot, as its name indicates is held at $T \sim 1$ K and provides the cooling power necessary to condense the ^3He into the ^3He pot. Liquid ^4He is brought into the 1K pot from the ^4He bath by a ^4He inlet tube, the opening of which is controlled by a needle valve. The temperature of the ^3He pot is monitored by a calibrated Cernox temperature sensor and can also be controlled with a heater for more elevated temperatures when needed. Pumping ports are mounted at the room temperature end of the insert (not shown) of which one is connected to a rotary pump to draw liquid ^4He through the 1K pot, and another one is connected to a diffusion pump in series with a rotary pump used to bring the main chamber to the desired vacuum. Pumping on the 1K line and sorbtion pump allows condensation of the ^3He charge and draws liquid ^4He from the bath inside the 1K pot. As the 1K stage cools, the ^3He condenses in the ^3He pot; the temperature in the sample chamber decreases as the ^3He condenses and the heat load from the remaining gas is reduced. The lowest temperatures are attained by allowing the 1K stage to cool the liquid as far as possible before the sorbtion pump starts to lower the vapor pressure above the liquid.

3.2.2 Data Acquisition Methods

The detection of small resistive signals such as the ones resulting from Hall effects requires the use of specialized measurement techniques. In our case, Hall resistance measurements require the possibility to discern changes of the order of $1 \mu\text{V}$ with a

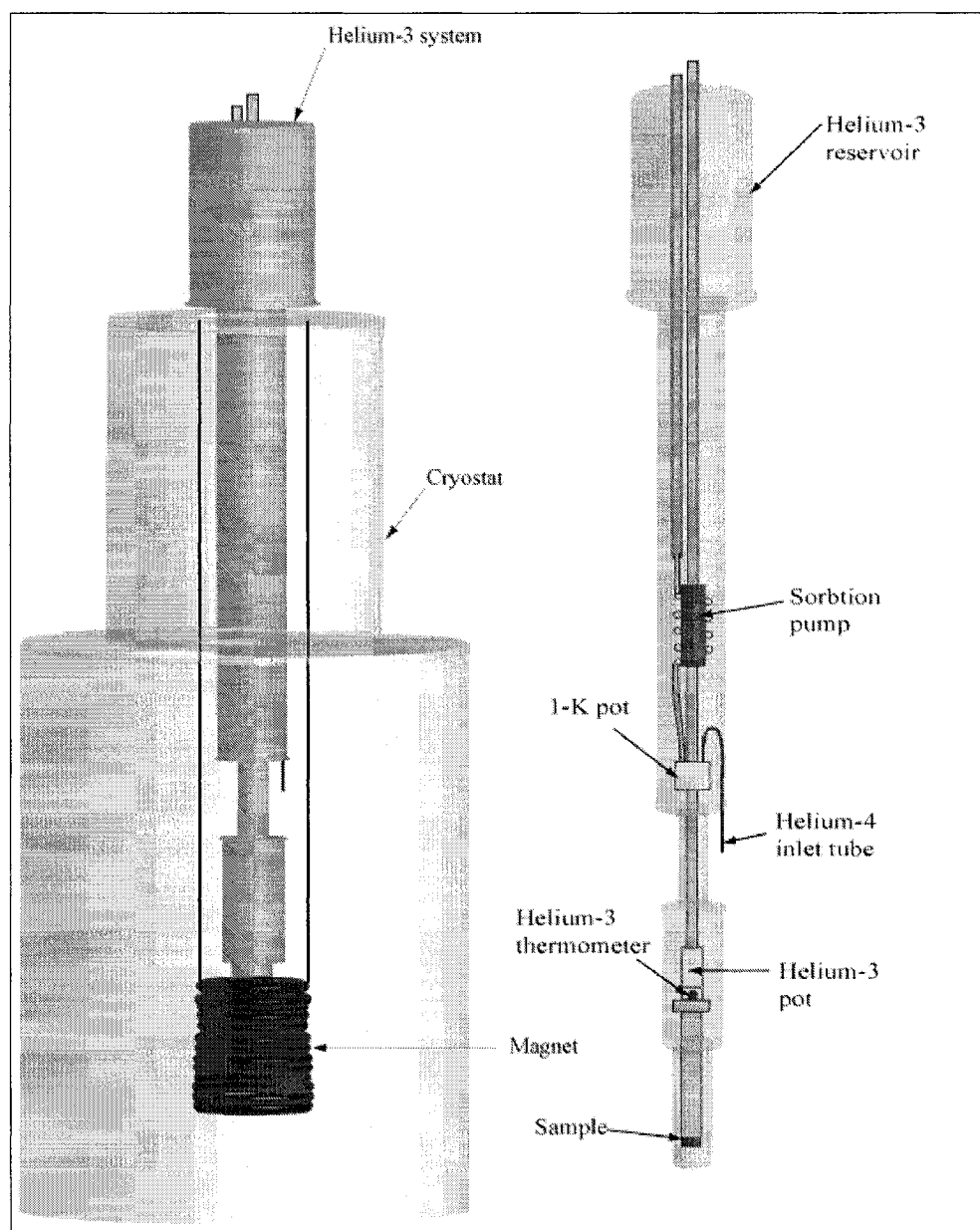


Figure 3.2: On the left: Cryostat, magnet and ^3He insert. On the right: ^3He insert with some of the interior components.

precision of at least 10 nV. The use of a direct current as a source is problematic as it introduces noise voltages mainly due to thermal effects in the sample or in the wires connecting the sample to the measurement system. Such thermoelectric phenomena as the Seebeck effect or the Thomson effect [33] can produce voltages of the order of a μV , even at low temperatures. Therefore, we used an alternating current as a source for our resistance measurements because it minimizes thermoelectric effects and filters an important part of the random noise. To this end, an AC resistance bridge was used which provided currents up to 10 mA at the frequency of 17 Hz. The resistance measurements were performed using a four-probe circuit, eliminating the effect of lead resistance in the results. The signal from the sample is pre-amplified before entering the resistance bridge for superior low noise performance of the instrument. The resistance bridge is also connected to a computer via a GPIB interface for a programmed control of the instrument. The use of a computer to control experiments evidently makes the tasks of data acquisition and analysis much easier. It also permits to acquire data with a greater precision since it allows repeated measurements of each data point.

3.2.3 *Systematic Errors*

Current Distribution

The conventional geometry used in measurements of Hall effects is shown in Figure 3.3(a). In this geometry, if the length of the sample is much greater than its width, one is sure that the current lines will be very parallel to the sides of the sample, thus avoiding most contact dependent effects. However, due to the reduced width of our samples (~ 1 mm), producing such a contact geometry is quite impossible. Therefore, the contact geometry shown in Figure 3.3(b) was used with the Hall probes directly on the sample, even though it implies that not all current lines will flow between the Hall contacts. To a first approximation, the real current flowing between the contacts will be reduced by a factor given by the ratio of the distance between the

Hall probes (L_v) to the width (L_w) of the sample:

$$I_{\text{real}} = \frac{L_v}{L_w} I_{\text{applied}}. \quad (3.8)$$

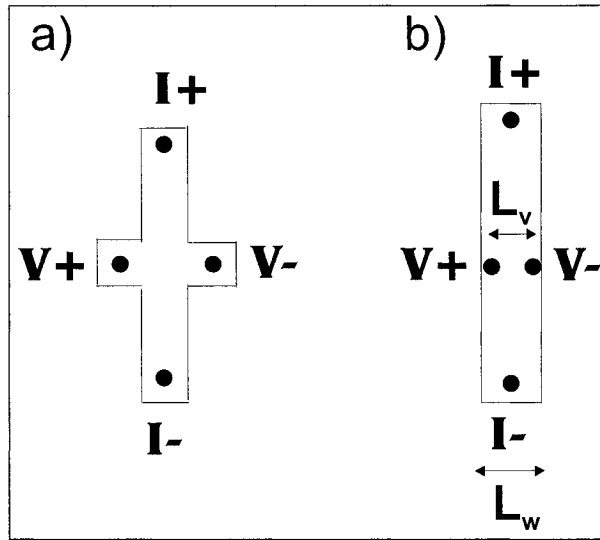


Figure 3.3: a) Conventional contact geometry for Hall effect measurements. It has the advantage that all the current lines are located between the Hall probes. b) Non-ideal contact geometry used for our measurements. The real current between the Hall probes is reduced by a factor $\frac{L_v}{L_w}$.

Temperature Stability

The magnetic field sweeps were typically performed at the rate of 0.8 T/min such that the time required for two sweeps (increasing and decreasing the field) between 0 and 6 T was about 15 min during which the temperature varied. The amount by which the temperature changed was dependent on the rate of sweeping the B field and on the current used, being larger for high sweep rates and high driving currents. However, even with the quite large B sweep rate of 0.8 T/min used and with currents up to 10 mA, temperature changes of less than 0.01 K were observed for all currents during the complete up and down sweeps. Considering that in this low temperature range (< 0.4 K) the upper critical transition B_{c2} is constant to within 0.1 T (see Figure 4.13, these temperature variations of the order of 0.01 K can be safely neglected. In fact, the greatest sources of errors in this work do not come

from the measurement apparatus, but from the samples themselves or the electrical contacts attached to them.

Separation of the Magnetoresistance and of the Hall Resistance

Since it is practically impossible to have a contact geometry such that the Hall probes are perfectly face to face along the width of the sample, the Hall signal will invariably contain a component of magnetoresistance which, in certain cases, can even hide any interesting feature due to the Hall effect, the magnetoresistance signal being about 100 times larger than the Hall signal. In normal Hall effect measurements (not in the superconducting state), this problem is overcome by measuring the magnetoresistance, which is symmetric in B field, and the Hall resistance, which is asymmetric in field, for both magnetic field orientations, such that the longitudinal contribution can be subtracted from the total voltage measured, leaving only the desired Hall contribution. However, Hall effects in the superconducting state are symmetric with magnetic field, as will be discussed in section 5.1, such that this trick can not be used here. A possibility would be to use a DC current as a source instead of an AC current, then if only the current or the field direction is reversed, the Hall voltage will be reversed and the pure Hall component can be extracted by subtracting two corresponding curves. However, this was not done because of the above-mentioned (section 3.2.2) downsides to the use of a DC source current. Therefore, the Hall contacts were made face to face as much as possible, such as to measure the smallest longitudinal component possible, and in cases where the contact alignment was not satisfactory the contacts were simply redone until adequate. The resulting Hall data still contain a minor longitudinal contribution, though negligible enough that the true Hall signal constitutes the most important part of it. In any case, the purpose of this work is not to establish the precise value of the Hall constant in the different samples of $\text{Fe}_x\text{Ni}_{1-x}\text{Zr}_2$, but to investigate the obscure behavior of the Hall effect in the superconducting state and its relation to the dynamics of vortices.

LONGITUDINAL RESISTANCE RESULTS

In this section, we describe qualitatively and quantitatively the results obtained from magnetoresistance measurements of different samples of $\text{Fe}_x\text{Ni}_{1-x}\text{Zr}_2$ with $x = 0, 0.1, 0.15, 0.2, 0.3, 0.33, 0.4$. Resistance variations were measured at temperatures below 400 mK and magnetic fields up to 6 T. The magnetic field was applied in a direction perpendicular to the current circulating in the sample, as shown in Figure 4.1. The peculiar phenomena known as the peak effect is observed in all samples. First, we present data for a sample with an iron content $x = 0.1$ and describe the mechanisms at the origin of the peak effect and the characteristics of vortex motion in the different phases observed. Then, different subjects related to observations on the rest of the samples will be introduced and supporting data will be shown.

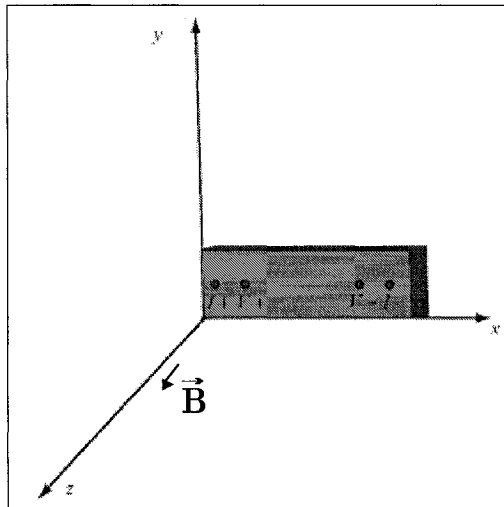


Figure 4.1: Geometry used for experimental measurements of R_{xx} with the magnetic field \vec{B} perpendicular to the direction of the current applied to the sample.

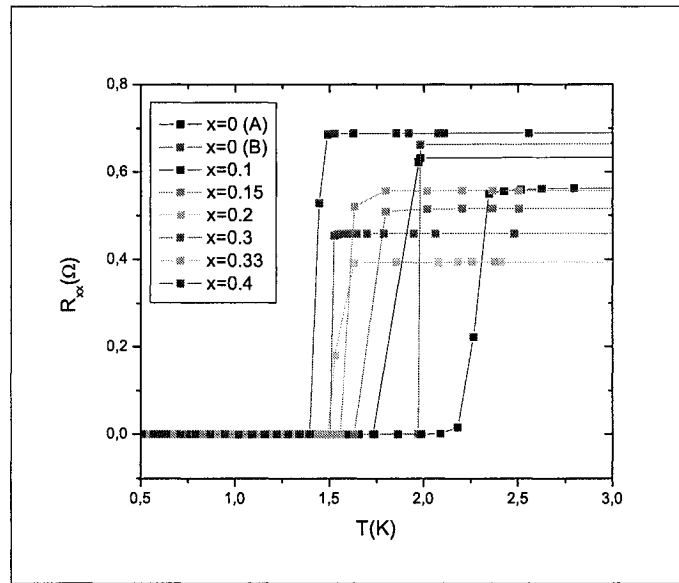


Figure 4.2: Resistance as a function of temperature for each sample. $I = 1\text{mA}$.

4.1 Critical Temperature

The critical temperature T_c was measured during cool down of the samples without a magnetic field and with a driving current $I = 1\text{mA}$; the results for all samples are shown in Figure 4.2. The transitions to the superconducting state are found to be very sharp, though a really meaningful evaluation of the widths of the transitions would require more data points in the transition region. The T_c values for the different alloys can be found in Table 3.1. The observed decrease of the T_c values was expected with increasing concentration of Fe as the introduction of iron suppresses superconductivity.

4.2 The Peak Effect

The resistance variation with magnetic field for a sample of $\text{Fe}_{0.1}\text{Ni}_{0.9}\text{Zr}_2$ observed at a temperature around 400mK is shown in Figure 4.3¹. A phase diagram of the dynamics of vortices, shown in Figure 4.5, is mapped out using these R_{xx} vs B results; the criteria for the determination of the phases are depicted in Figure 4.4,

¹Data for the samples with $x = 0, 0.3, 0.33, 0.4$ are found in Appendix A.

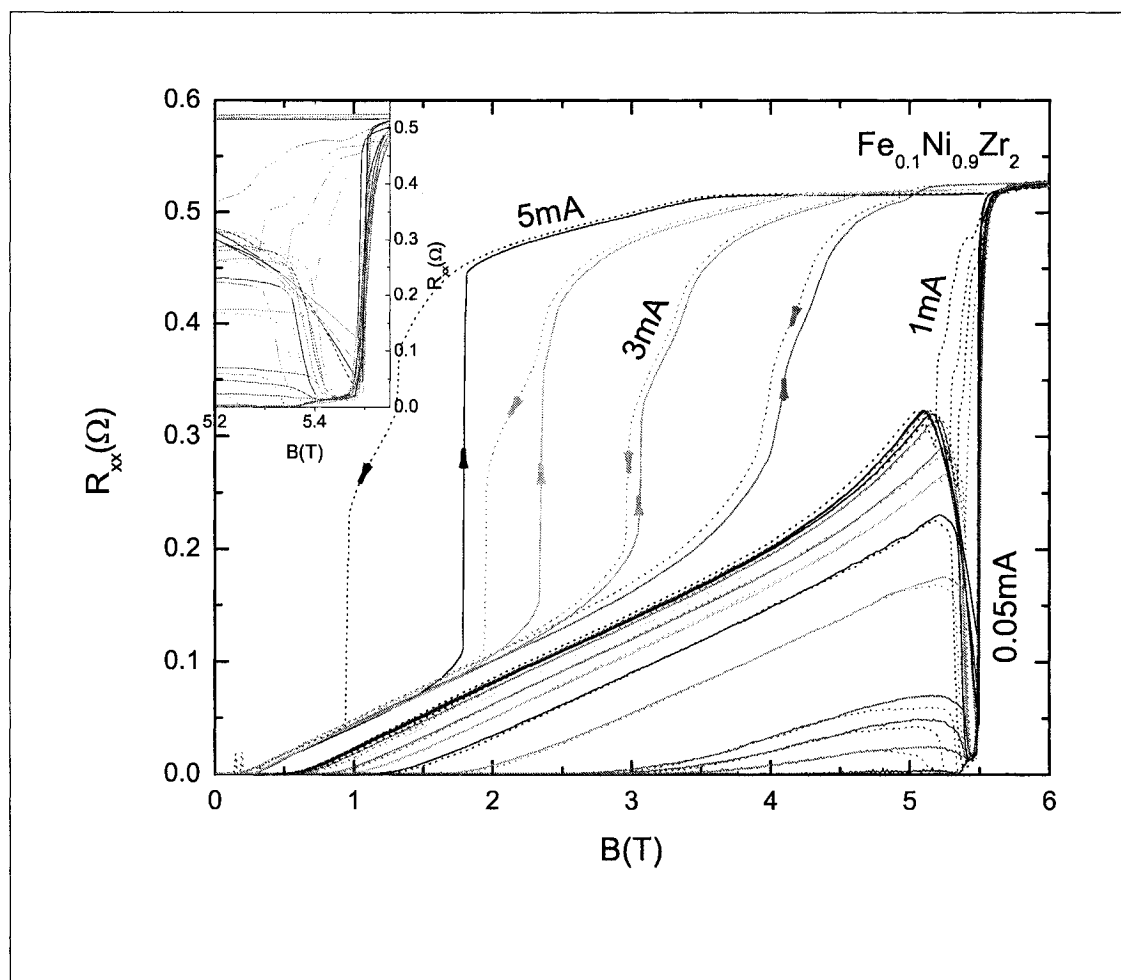


Figure 4.3: Resistance as a function of B for up and down B sweeps on sample $\text{Fe}_{0.1}\text{Ni}_{0.9}\text{Zr}_2$. The different curves are for different excitations (0.05, 0.075, 0.09, 0.1, 0.2, 0.3, 0.4, 0.5, 0.6, 0.7, 0.8, 0.9, 1, 2, 3, 4, 5 mA). Inset: Expansion of the high field region. $T \approx 400\text{mK}$.

which shows a B down-sweep with $I = 1$ mA for $\text{Fe}_{0.1}\text{Ni}_{0.9}\text{Zr}_2$. The first depinning transition is defined when the resistance exceeds 0.5 m Ω , which is our experimental resolution. Close to this transition, the dependence of the resistance on B is stronger than exponential, making the choice of this cutoff not critical. The pinning transition is then defined when $\frac{dR}{dB} = 0$; it is this reentrant pinning phase which is known as the peak effect. Finally, we define B_{c2} as the point of strongest negative curvature just before reaching the normal state. At sufficiently high driving current, an additional depinning phase is clearly observed right before the transition to the normal state, which we will call depinning 2; it is delimited by either the departure from the pinning phase in the smaller drive regime or the abrupt increase in R after the depinning 1 phase in the larger drive regime. These different phases of vortex motion will be described in detail in the following sections.

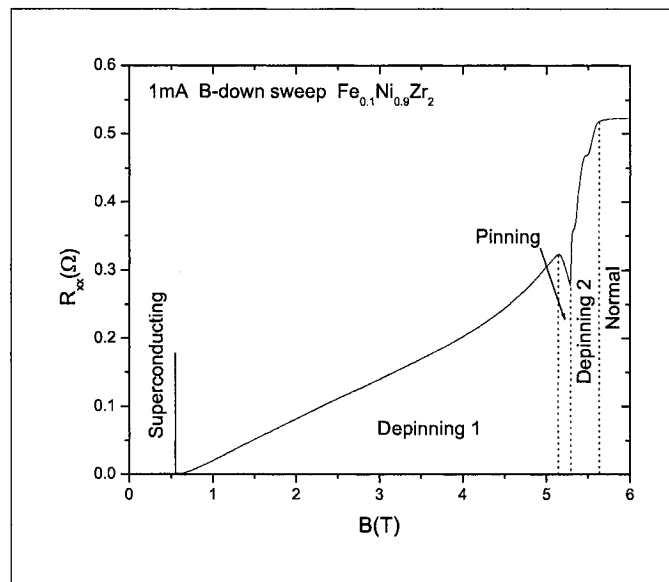


Figure 4.4: Resistance of the 1 mA down-sweep for $\text{Fe}_{0.1}\text{Ni}_{0.9}\text{Zr}_2$, illustrating how the phases are determined.

4.2.1 The First Depinning Phase

The current dependent departure from the superconducting state at some magnetic field value marks the onset of vortex motion and indicates the existence of a critical

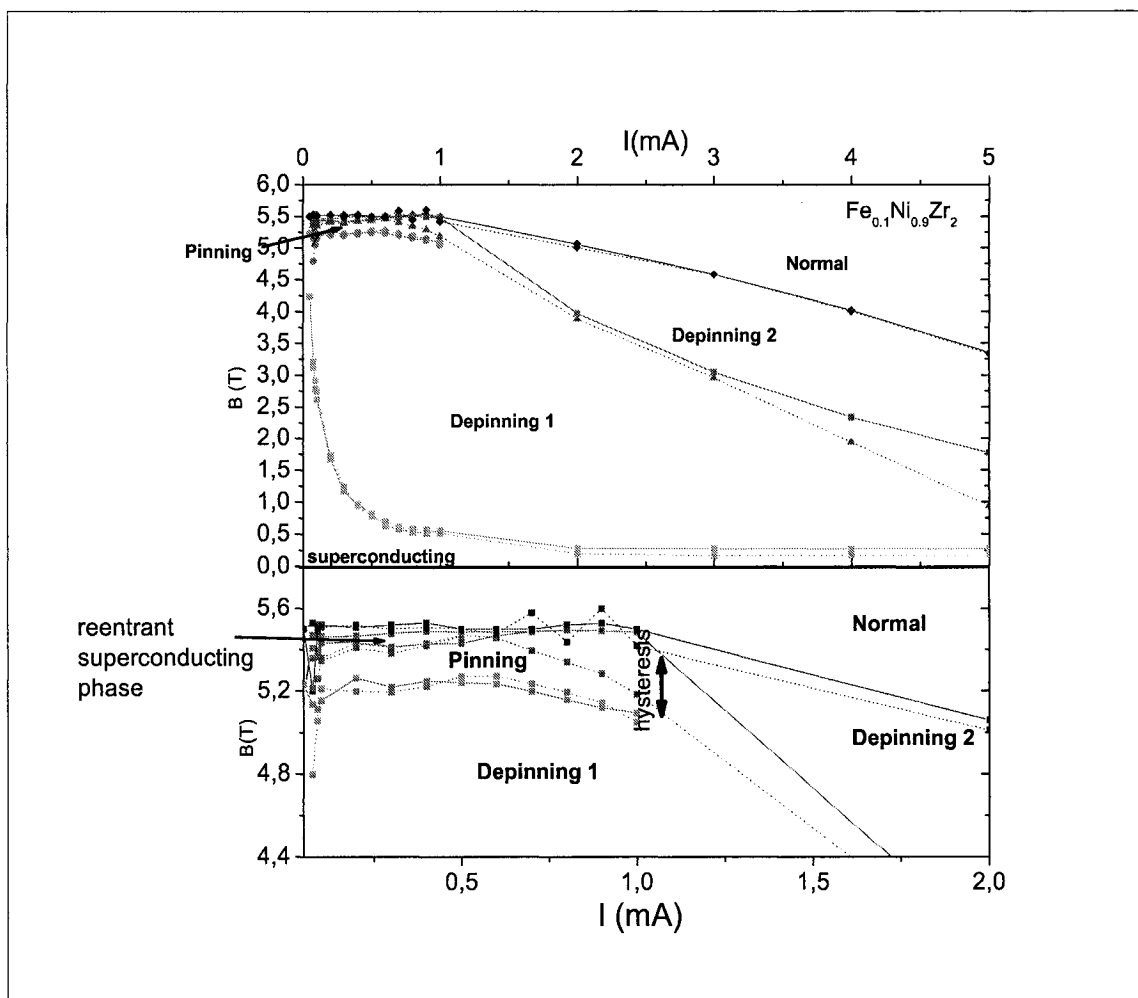


Figure 4.5: Phase diagram of vortex dynamics for sample $\text{Fe}_{0.1}\text{Ni}_{0.9}\text{Zr}_2$. Solid lines correspond to data obtained sweeping B up and the dotted lines to data obtained sweeping B down. The lower panel is an enlargement of the low I and high B region.

force for the depinning of vortices. This motion of vortices induces a dissipative current in the sample, which is responsible for the finite resistance measured in the superconductor, as described in section 2.1.6. This phase, which we will call depinning 1, is characterized by weakly pinned, slow moving vortices. It is generally described in the literature [21] as a phase having long-range order: the moving Bragg glass (MBG). The increase in resistance in this phase is almost linear until the magnetic field reaches a certain value slightly below the upper critical transition at which the resistance drops as some, or all, the vortices become pinned again.

4.2.2 *The Reentrant Pinning Phase*

A reentrant pinning phase occurs at a magnetic field value slightly below the upper critical transition which is characterized by a sudden decrease in the resistance: this is the peak effect. The origin of this new pinning transition is still under debate, but is generally accepted to result from an order-disorder transition, or the melting of the vortex lattice. In this phase, the distance between vortices is of the order of ξ and inter-vortex correlations become strong. The mechanisms for this reentrant pinning phase can be understood in terms of a softening of the FLL (see section 2.2.1) which causes the vortices to adapt better to the pinning potential, thus allowing them to find a configuration which lowers their energy, thereby suspending their motion. In amorphous superconductors, this is the first observation of such a strong reentrant behavior, and the fact that this type of behavior is observed for different concentrations of Fe hints that this effect is typical of weakly pinned amorphous superconductors. This pinning phase is very narrow and the sample readily leaves it to enter a second depinning phase before reaching the normal state.

4.2.3 *The Second Depinning Phase*

In these longitudinal resistance measurements, the depinning 2 phase is only observed at sufficiently high driving current, either when leaving the pinning phase, or when leaving the depinning 1 phase in the larger drive regime. This phase was described in some theoretical and numerical works [1, 34, 35] as being characterized by a smectic

or plastic motion of vortices. The presence of this phase between the peak effect and the normal state suggests a much richer transition than previously expected between these two phases; it is not just an inhomogeneous mix of normal and superconducting regions as inferred by the width of the superconducting-to-normal transition (less than 30 mT wide for the 10%-90% transition) at low currents.

The phase diagram of Figure 4.5 clearly shows that for excitation currents above 1 mA, the sample goes directly from the depinning 1 phase to the depinning 2 phase without entering a pinning phase as is the case at low excitation current. This direct transition from the depinning 1 region to the depinning 2 region is identified in the longitudinal transport data shown in Figure 4.3 by a jump in the resistance and corresponds to a sudden delocalization of the vortices. In this region, a strong hysteretic behavior is observed from sweeping the magnetic field up (solid lines) and down (dotted line). This means that for a fixed I in this range, increasing the magnetic field for a system in the depinning 1 regime into the hysteresis region results in motion of vortices characteristic of the depinning 1 phase. On the other hand, reducing the magnetic field from the depinning 2 regime into the hysteresis region, vortex motion remains plastic or smectic, characteristic of the depinning 2 phase. This type of behavior was predicted in ref. [35], in which the hysteresis region was described as a mixed regime between a plastic flow of vortices in a decoupled channel regime and a MBG regime. The hysteretic region becomes larger with driving current and does not depend on the sweeping rate; it is also found to be independent of pinning effects. This phase will be described in more detail in section 4.4.

The lower panel of Figure 4.5 shows that another hysteretic region exists for currents between 0.5 mA and 2 mA, which now occurs between the pinning phase and the depinning 2 phase. This second hysteretic phase does not arise from the same effects as those which cause the hysteresis between the two depinned regimes, but originates from the pinning phase and the depinning 2 phase being two metastable states separated by an energy barrier. The presence of this hysteresis is definitely a consequence of pinning effects, which clearly makes it distinct from the hysteretic

curves found at large driving currents, which are practically independent of pinning.

4.3 $V - I$ Characteristics

The $V - I$ curves² extracted from the R vs B data³ for a sample with $x = 0.3$ ⁴ are shown in Figure 4.6 for different fields in the peak effect region. The motivation for the study of the $V - I$ characteristics is the comparison with theoretically predicted results which will be presented in the next section.

In the region close to the peak effect, the observed negative differential resistance indicates that some vortices get re-pinned before the second depinning transition at some higher B -field value suggesting the existence of a dynamical pinning mechanism for high vortex velocities.

The insets show the curves as extracted from the low- B depinning 1 region. The low- B and low- I curves of the upper inset are well fitted by the activated creep expression $V \approx \exp\left(\frac{U}{T}\sqrt{I}\right)$, which is consistent with the long-range ordered moving Bragg glass proposed by Giamarchi [1, 36]. This creep regime is characterized by a very slow thermally activated motion of vortices as described in section 2.1.7.

The hysteretic behavior of the disordering transition is again observed here from the switching character of the $V - I$ curves extracted from up B sweep data (solid lines) and down B sweep data (dotted lines). The main panel of Figure 4.6 shows the switching character between the pinning and depinning 2 phase, while the lower inset shows that between the two depinning phases. Similar $V - I$ characteristics are obtained from R_{xx} vs B measurements on all our samples. Comparable results also prevail in the literature in both experimental [37, 38] and theoretical [39, 36, 40, 41, 1] works. The next section will discuss how such $V - I$ characteristics are obtained.

² $V - I$ characteristics are analogous to vortex velocity vs driving force characteristics which are more often found in theoretical works on the subject.

³The $V - I$ characteristics were not recorded experimentally because this would have required the use of a DC current, with all the associated drawbacks described in section 3.2.2.

⁴ $V - I$ curves for the other alloys are shown in Appendix A.

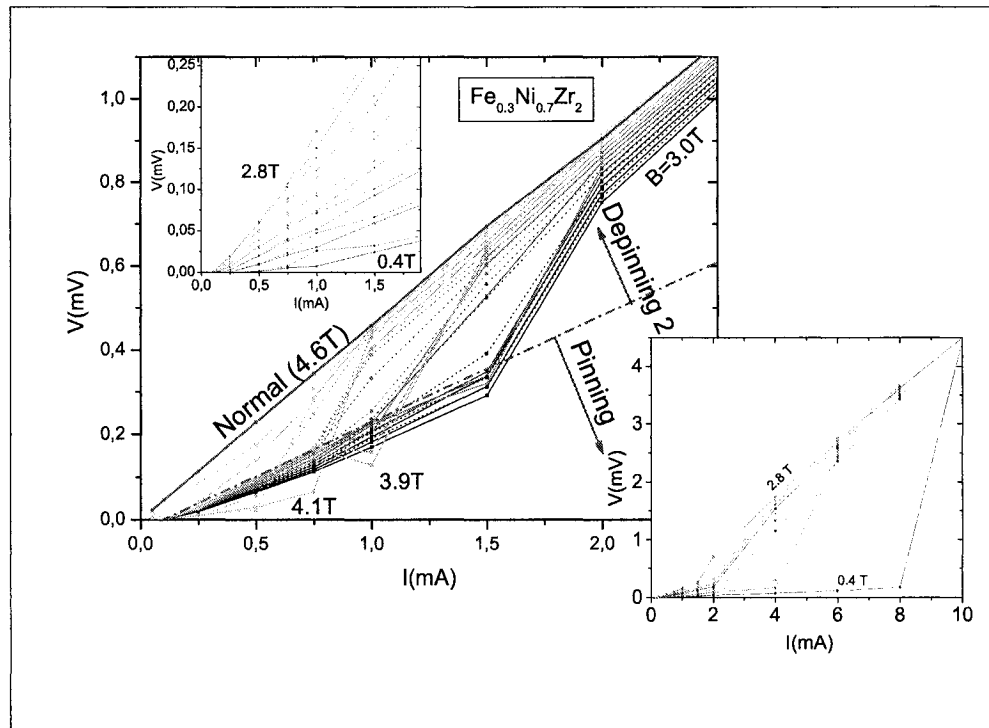


Figure 4.6: V - I curves extracted from R_{xx} vs B data for sample $x = 0.3$ for up (solid lines) and down (dotted lines) B sweeps. The different curves correspond to different B values. Main panel: B in the peak effect region. Upper inset: Enlargement of the Low- B region. Lower inset: Low- B region, full range.

4.4 Vortex Instabilities

This section discusses the occurrence of the direct and abrupt transitions from the depinning 1 phase to the depinning 2 phase in the high-drive R_{xx} vs B curves, as well as the hysteresis observed at this transition. A theory by Larkin and Ovchinnikov (LO) [42, 43] predicted in 1975 the existence of such hysteretic jumps in the current-voltage characteristics. The LO theory attributes this effect to the fact that at large vortex velocities, the number of quasiparticles inside the vortex cores would diminish for the benefit of those outside, as the particles accelerated by the electric field could reach energies above that of the superconducting energy gap and diffuse away from the cores. This would cause a significant decrease in the size of vortices since the effective pressure exerted by the quasiparticles on the vortex walls would diminish, and this shrinking of vortex diameter would in turn induce a decrease of the viscosity drag coefficient. Therefore, for some critical value of flux line velocity, the voltage as a function of current bias suddenly jumps to a maximum value with the associated discontinuity in the $V - I$ characteristics. This hysteretic jumps would be unrelated to Joule heating and depairing current. Such sudden voltage jumps were observed in some experiments on low- T_c [44, 45, 46] and high- T_c [47] superconductors; to the best of our knowledge, the hysteresis was observed only once [48].

We will now show how the LO theory relates to our $V - I$ curves. The vortex radius ξ as a function of voltage is given by

$$\xi^2(V) = \frac{\xi^2(0)}{1 + (V/V^*)^2}, \quad (4.1)$$

while the viscosity coefficient η is

$$\eta(V) = \eta(0) \frac{\xi^2(V)}{\xi^2(0)}. \quad (4.2)$$

The nonlinear $V - I$ characteristics are found from

$$I = \frac{V}{R_n} \left[\alpha \frac{1}{1 + (V/V^*)^2} + 1 \right] \quad (4.3)$$

and

$$\left(\frac{V^*}{l} \right) = \frac{1792\zeta(3)\beta_A k_B^2 (T_c - T)^3}{\pi^6 e^2 D T \tau_\epsilon}, \quad (4.4)$$

where τ_ϵ is the inelastic electron scattering time, $\zeta(x)$ is the Riemann zeta function, e is the electron charge, k_B is Boltzmann's constant, $\beta_A = 1.16$, $D = (1/3)v_F l$ is the diffusion coefficient where v_F is the Fermi velocity, and l the electron mean free path. In the low-field limit (which is the case we want to study), the coefficient α is given by

$$\alpha = \frac{4.04 H_{c2}}{\left(1 - \frac{T}{T_c}\right)^{1/2} H}. \quad (4.5)$$

Plots of equation 4.3 are shown in Figure 4.7 with $R_n = 0.515$ as is the case for our sample with $x = 0.1$, and $V^* = 0.5$ and $\alpha = 2, 4, 8, 14, 18.4$. These values for α and V^* were chosen so as to best show the evolution of the $V - I$ characteristics with field. Lower α values basically correspond to higher magnetic field values.

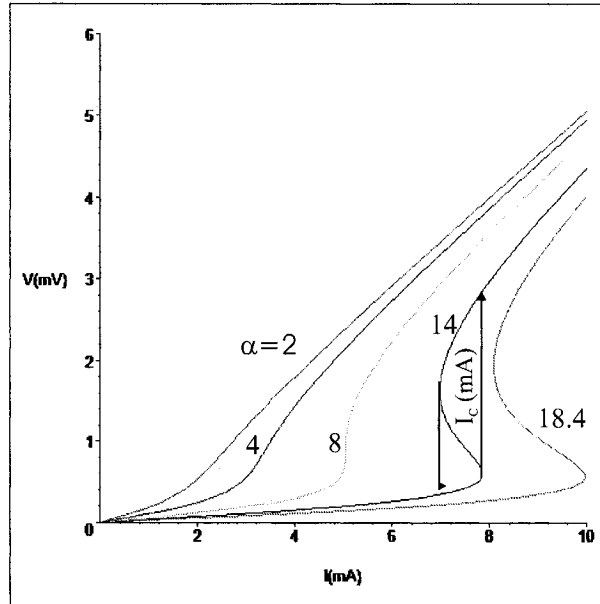


Figure 4.7: V-I curves plotted from equation(4.3) using $R_n = 0.515$, $V^* = 0.5$ and $\alpha = 2$ (red), 4 (blue), 8 (green), 14 (black), and 18.4 (orange).

The S shape of curves $\alpha = 14$ and $\alpha = 18.4$ shows how one gets the hysteretic behavior of the $V - I$ characteristics. In experiments using increasing current bias, when I reaches the value labeled as I_c , at which point $\frac{dI}{dV}$ would become negative in the V -biased case, the voltage switches to the more resistive state (as shown by the up-pointing arrow). Alternatively, when decreasing the current bias, the voltage

adopts the less resistive state at a lower value of current, as shown now by the down-pointing arrow. Our $V - I$ curves are found to be well-fitted by equation 4.3, as shown in Figure 4.8 in which the $B = 0.4$ T curve is fitted using $\alpha = 13.46$ and $V^* = 0.24$. This fit mimics well the hysteretic behavior found in the data such that it can be asserted that the LO theory clearly predicts the relationship between V and I for large magnetic fields. It is to be noted however that the LO theory does not take into account pinning effects which are always present in real samples, but which might be weak enough in our samples for the data to be well represented by the theory.

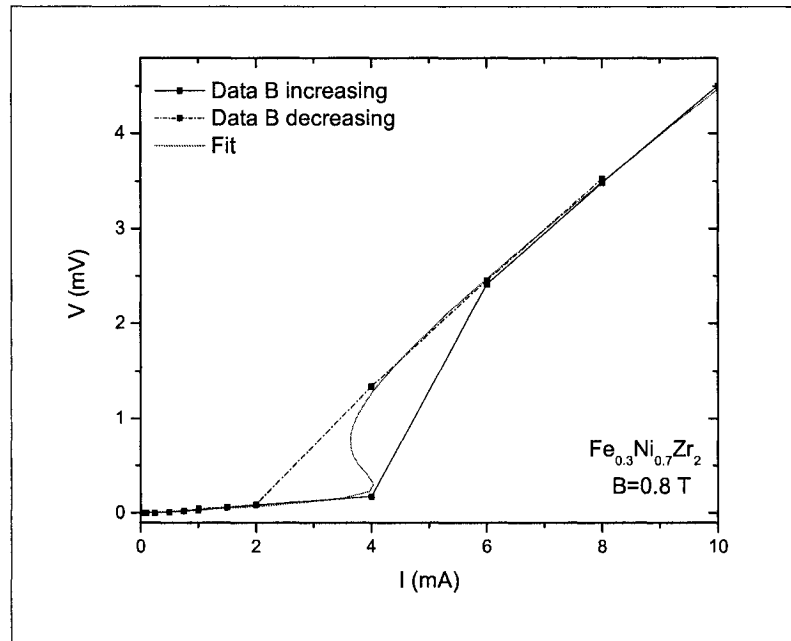


Figure 4.8: Black: $V - I$ characteristics extracted from R vs B data on sample $x = 0.3$ for $B = 0.8$ T. Red: Best fit to the data using equation 4.3. The best fit values were found to be $\alpha = 13.46$ and $V^* = 0.24$.

Now, the question is: how does this relate to the R_{xx} vs B data? The answer can be found by simply inspecting the curves shown in Figure 4.7. For the higher-driving current curves, the voltage jumps occur at lower magnetic field values, as expressed in the $I - V$ equation 4.3 by larger parameter α values. In addition, the size of the hysteretic region augments with increasing drive and this is observed in the more

pronounced S shape (curve $\alpha = 18.4$) of the $V - I$ curve when plotting equation 4.3 using larger α values.

4.5 Joule Heating

Joule heating is an important effect to discuss at this point as it is known [49] to cause nonlinear phenomena and bistability in superconductors. Self-heating can occur in superconductors when a significantly high current is applied, such that there is an increase in the effective temperature at the sample; the critical current is thus lowered and the superconducting state is prematurely destroyed. Joule heating in superconductors typically produces nonlinear, S-shaped $V - I$ characteristics much like those shown in Figure 4.7, though for different reasons. Usually, the $V - I$ characteristic of a hard superconductor in the resistive state is linear in E and given by

$$j = j_c(T, B) + \frac{1}{\rho_f} E \quad (4.6)$$

where $\rho_f \sim \rho_n B / B_{c2}$ is the flux-flow resistivity, and ρ_n is the normal state resistivity. If self-heating is non-negligible, nonlinearities in the $V - I$ characteristics arise because $j_c(T)$ in equation 4.6 is a function of the sample temperature T , which in turn depends on the heat balance equation $Q(T) = W(T) = \frac{h(T)}{d}(T - T_0)$ where $Q(T)$ is the power of the Joule heat release, $W(T)$ is the power of heat transfer to a coolant, $h(T)$ is the heat-transfer coefficient, T_0 is the coolant temperature and $d = A/P$, the ratio of the area to the perimeter of the sample.

A useful quantity in determining whether self-heating is important or not is the Stekly [50] parameter β ; if $\beta > 1$, then Joule heating is substantial, but if $\beta \ll 1$, it is negligible. β is given by the ratio of the characteristic heat generation in the normal state to the heat transfer, thus

$$\beta = \frac{\rho_n j_c^2 d}{h(T_c - T_0)}. \quad (4.7)$$

We typically have $j_c \leq 0.4 \text{ A/cm}^2$, $\rho_s = 1.7 \mu\Omega\text{m}$, $T_c = 2.3 \text{ K}$, $T_0 = 0.35 \text{ K}$, and $d = \frac{8 \text{ mm}^2}{18 \text{ mm}} = 0.44 \text{ mm}$. The heat transfer coefficient h is hard to determine because it depends on many factors; as the sample is in vacuum, heat transfer to the surrounding is very negligible, so that the bulk of the heat is transferred to the copper sample holder. Estimating the lower limit for h such that $\beta > 1$, and Joule heating becomes important, one obtains $h_{\min} \approx 6 \times 10^{-3} \frac{\text{W}}{\text{m}^2\text{K}}$. This means that for $h > h_{\min}$, Joule heating will not be significant, and since the estimated value of h_{\min} is very small (a typical value for heat transfer to copper is $1 \text{ W/cm}^2\text{K}$), we can safely assume that self-heating is unimportant in the present case.

Another indication that Joule self-heating is negligible here is by looking at the value of B_{c2} for up and down B sweeps in Figure 4.3, for the $I = 5 \text{ mA}$ curve for instance. One sees that B_{c2} is not shifted to lower values of B in the down B -sweep with respect to the up B -sweep curve, indicating that Joule heating is not taking place, because it would tend to lower the B_{c2} of the down B -sweep curve. Moreover, since the temperature must be practically constant along the upper part of the hysteresis loop (the down B -sweep part), but more heat is dissipated along this branch because it is more resistive, it is impossible that the resistance jump observed in the up B sweep curve be attributable to self-heating since it occurs precisely in the part of the hysteresis loop which is less resistive, and thus dissipates less heat. Therefore, this is a clear indication that the temperature increase due to Joule heating is negligible, and that the nonlinear, S-shaped $V - I$ characteristics observed here result from vortex instabilities.

4.6 Suppression of the Pinning Phase

In some of our samples, namely those with $x = 0$, $x = 0.15$ and $x = 0.20$ iron, a suppression of the reentrant pinning phase was observed, as shown in Figure 4.9 for a sample with $x = 0.15$. This might be due to those ribbons not being fully structurally relaxed, as discussed in section 3.1.4. These samples could contain different amounts of strain fields and/or a non-uniform distribution of voids, which could affect vortex

motion significantly.

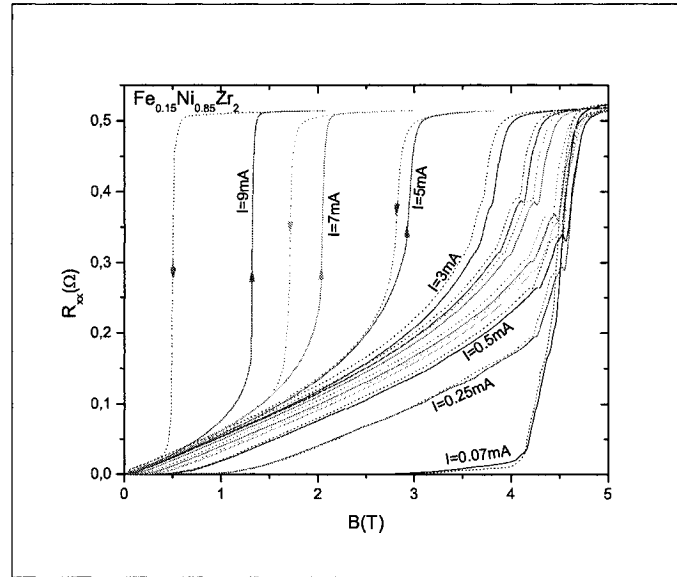


Figure 4.9: Longitudinal resistance *vs* magnetic field for up and down B sweeps on a sample with 15% Fe and with $I = 0.07, 0.25, 0.5, 0.75, 1, 1.5, 2, 3, 5, 7, 9$ mA

4.7 Suppression of Hysteresis

A striking feature of the data from sample $\text{Fe}_{0.2}\text{Ni}_{0.8}\text{Zr}_2$ (Figure 4.10) is the total absence of any of the hysteretic behavior observed in the other samples (in addition to the suppression of the reentrant pinning phase) at the transition between the two depinning phases at high driving currents and in the pinning phase at larger B . This shows that there really is something different in the samples with 20% iron. We could not find any explanation for the absence of the large- I hysteresis described earlier by the LO theory. However, since the hysteresis in the reentrant pinning phase is a consequence of pinning, it can be resolved that the suppression of this hysteretic phase here arises from a discrepancy in the disorder present in this sample with respect to the other samples. If this sample contains different amounts of strain fields, or a non-uniform distribution of voids compared to the other samples as suggested in the previous section, then it is possible that these attributes have an important effect on pinning.

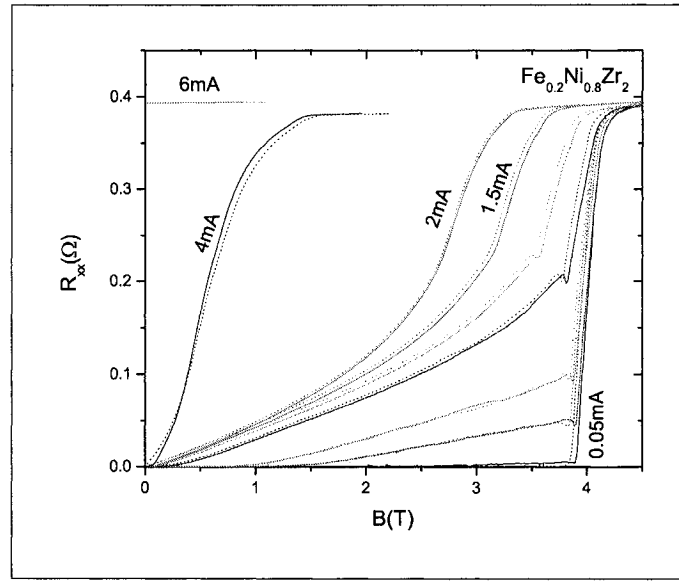


Figure 4.10: Longitudinal resistance as a function of B for a sample of $\text{Fe}_{0.2}\text{Ni}_{0.8}\text{Zr}_2$ for up (solid lines) and down (dotted lines) B sweeps and for driving currents between 0.05mA and 6mA (0.05, 0.1, 0.15, 0.5, 1, 1.5, 2, 4, 6)mA. $T=400\text{mK}$

4.8 Compilation of Results

A compilation of the results for all the alloys with different iron concentrations is presented in this section. Figure 4.11 shows the B -onset of the depinning 1 phase, pinning phase, depinning 2 phase, and B_{c2} as a function of x , the iron concentration in the alloy. The real values for each alloy can not be determined from this study because this would require several data points for each alloy; still the observed behavior of B_{c2} with increasing iron concentration follows our expectations. In fact, it is known from ref. [51] that superconductivity is strongly suppressed by the presence of Fe in Fe-Zr metallic glasses. This result is interpreted as due to stronger spin fluctuations in Fe-rich alloys, which favor parallel spin configurations and therefore act as pair breakers. In addition, it is known from ref. [31] that for alloys of $\text{Ni}_x\text{Zr}_{100-x}$ and $\text{Fe}_x\text{Zr}_{100-x}$ with $x = 20$, $B_{c2} = 2.97 \text{ T/K}$ and $B_{c2} = 3.71 \text{ T/K}$ respectively, as if the introduction of a small amount of Fe increases B_{c2} . In the light of these results, the increase in B_{c2} when going from $x = 0$ to $x = 0.1$ in our case, as well as its subsequent decrease with increasing x could be expected.

Table 4.1 shows some results for the different alloys in tabular form. It includes the values of the B -onsets of the different pinning-dependent phases, the T_c 's and the widths of the 10%-90% transition. The B -onsets of the different phases and the T_c 's are taken for curves measured with $I = 1$ mA. T_c is determined in the usual way as the midway point on the R vs T transition. The width of the 10%-90% transition is always established from the lowest excitation curve available for each data set. It is important to note that these results are issued from a single measurement on a single sample of each alloy such that the values are not to be taken as the "real" values. An exhaustive study of the different alloys is not the subject of this work and this compilation is only shown for the purpose of completeness and comparison between the different alloys.

Sample	B/B _{c2} Depin- ning 1	B/B _{c2} Pinning	B/B _{c2} Depin- ning 2	B _{c2} (T)	T _c (K)	Width 10%-90% (mT)
NiZr ₂	0.05	0.91	0.92	4.83 ± 0.01	1.9 ± 0.1	310
Fe _{0.1} Ni _{0.9} Zr ₂	0.10	0.93	0.99	5.50 ± 0.01	2.72 ± 0.05	30
Fe _{0.15} Ni _{0.85} Zr ₂	0.04	0.96	0.96	4.65 ± 0.01	1.72 ± 0.08	470
Fe _{0.2} Ni _{0.8} Zr ₂	0.02	–	0.91	3.91 ± 0.01	1.54 ± 0.05	210
Fe _{0.3} Ni _{0.7} Zr ₂	0.02	0.87	0.96	4.02 ± 0.01	1.53 ± 0.01	150
Fe _{0.33} Ni _{0.67} Zr ₂	0.04	0.90	0.94	3.59 ± 0.01	1.60 ± 0.03	190
Fe _{0.4} Ni _{0.6} Zr ₂	0.03	0.74	0.92	3.51 ± 0.01	1.43 ± 0.03	530

Table 4.1: List of samples with some important results

4.9 Temperature dependence

The temperature dependence of the B -induced peak effect in a sample of Fe_{0.4}Ni_{0.6}Zr₂ is shown in Figure 4.12. The data was acquired with a current of 1 mA at different constant temperatures, typically varying by only ± 0.01 K for $T < 0.6$ K

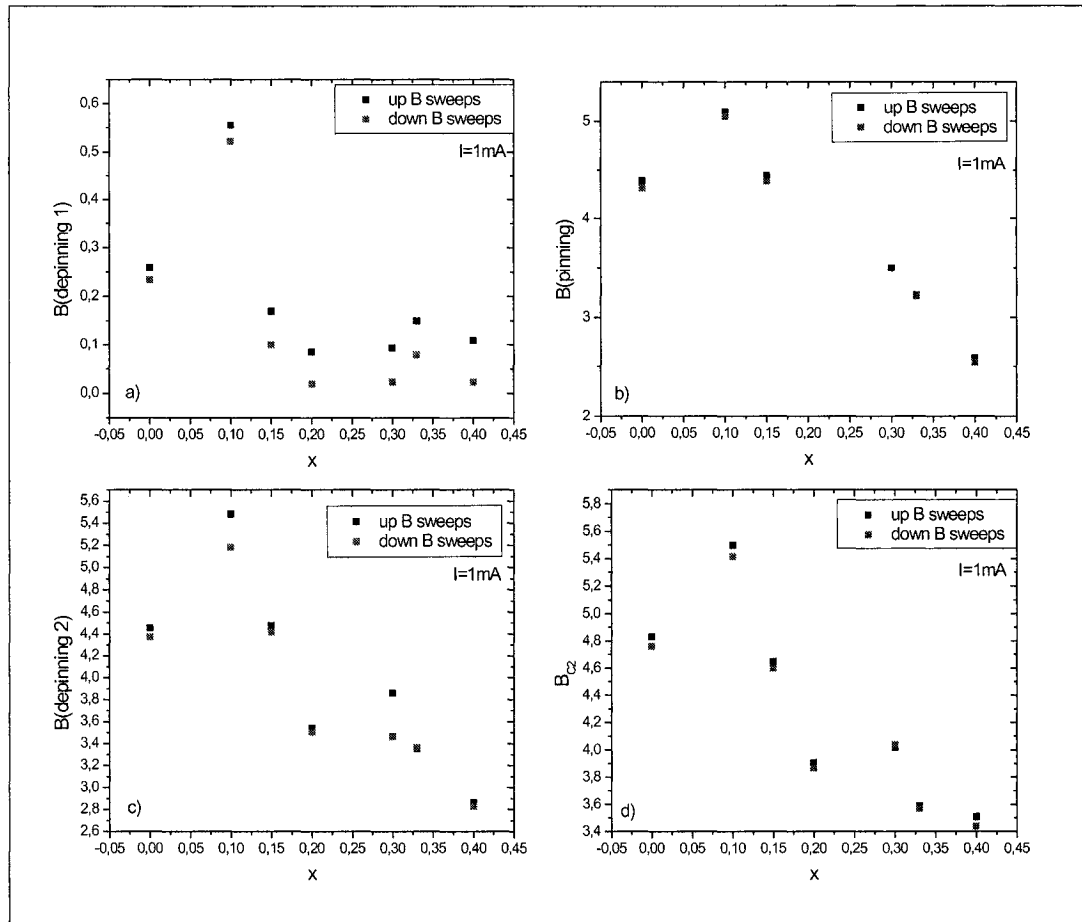


Figure 4.11: Onset of the different vortex phases as a function of x , the iron concentration in $\text{Fe}_x\text{Ni}_{1-x}\text{Zr}_2$ measured with $I = 1\text{ mA}$. a) Onset of depinning 1 phase. b) Onset of pinning phase. (No data point is found for $x = 0.20$ for this phase, because the data did not show a reentrant pinning phase for this current.) c) Onset of depinning 2 phase. d) B_{c2}

and ± 0.07 K for $0.6 < T < 2$ K over each B sweep. The shape of the magnetoresistance curves is found to be very similar from curve to curve in the lowest temperature range. However, for temperatures higher than 1 K, a significant narrowing of the pinning phase is observed. Unfortunately, no data was acquired for temperatures between 0.62 K and 1 K due to the difficulty of stabilizing the temperature within that range, making it hard to determine the exact temperature at which the pinning phase starts to narrow significantly.

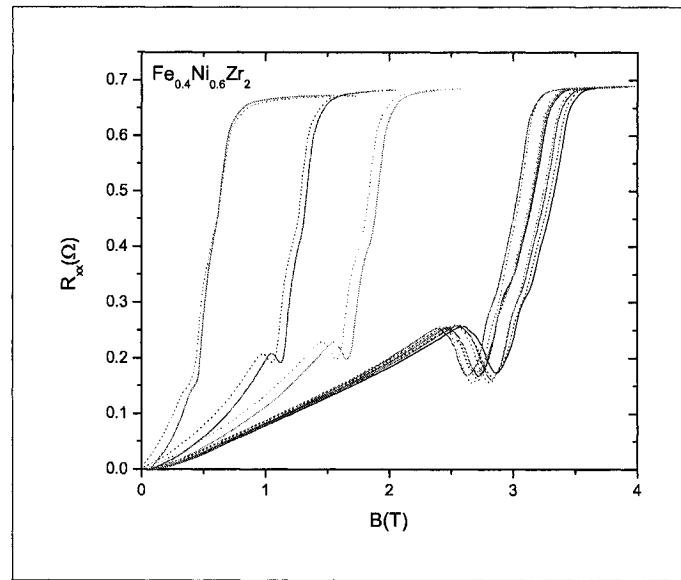


Figure 4.12: Longitudinal resistance as a function of B for a current of 1 mA applied to a sample of $\text{Fe}_{0.4}\text{Ni}_{0.6}\text{Zr}_2$. The different curves correspond to different temperatures between 0.33 K and 1.65 K (0.33, 0.38, 0.45, 0.52, 0.62, 1.1, 1.34, 1.59) K.

The phase diagram of vortex dynamics as a function of temperature extracted from the transport data of Figure 4.12 is shown in Figure 4.13. The phase diagram shows no region of hysteresis, in contradiction with ref. [37] in which a large region of hysteresis was observed for $\text{Fe}_{0.3}\text{Ni}_{0.7}\text{Zr}_2$ to decrease with increasing temperature until it finally completely vanished. The reason why we do not find the same result here is most probably not dependent on the sample, but rather on the fact that even at the lowest temperature attained, the data acquired with $I = 1$ mA does not show any hysteretic behavior. Having used a current of 3 mA, a phase diagram with a region of hysteresis similar to that observed in [37] would certainly have been

observed, as judging from the 3 mA curve in Figure A.4 since an important region of hysteresis is observed in this curve. In any case, the dependence on temperature is noncritical, which is highly suggestive of a first order transition here associated with the transition to the depinning 2 phase rather than with the pinning phase as shown by earlier experiments on crystals [52]. A broadening of the depinning 2 phase is observed at higher temperature as seen in Figure 4.13, as was predicted in ref. [1].

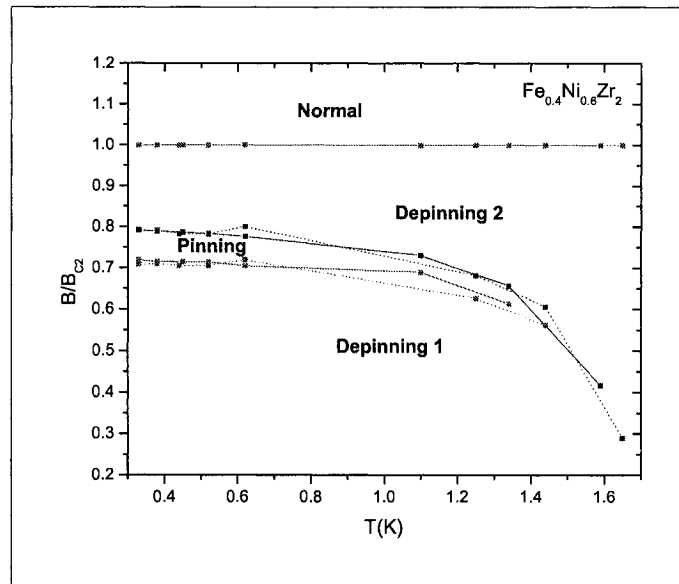


Figure 4.13: Phase diagram of vortex dynamics as a function of temperature for sample $\text{Fe}_{0.4}\text{Ni}_{0.6}\text{Zr}_2$. The data was rescaled with B_{C2} and taken with $I = 1 \text{ mA}$.

THE HALL EFFECT IN TYPE II SUPERCONDUCTORS

The Hall effect in the superconducting state still eludes the scientific community; it remains controversial even after over 40 years of research on the subject. Some predict a Hall sign reversal below T_c caused by pinning effects [53], others argue that the anomaly can not be due to pinning [54, 55, 56], whilst others even predict no sign reversal at all [57, 58]. Only few studies report Hall effect measurements [56, 59, 60, 61] on samples which also exhibit the peak effect in longitudinal transport measurements; the results obtained in these studies will be discussed in this section, though we start first with a description of the forces at work in a superconductor such that a Hall resistance is measured, which will be followed by a terse presentation of some theories of transverse vortex motion proposed to date.

5.1 Elementary Hall Effect Phenomenology

The Hall effect in normal metals is a transport phenomenon very well understood today and which has been used since its discovery in 1879 for numerous purposes such as the determination of the sign of charge carriers in metals. In normal metals, the Hall resistance arises from the electric field developed across two ends of a conductor in the direction $\vec{J} \times \vec{B}$ upon application of a current \vec{J} , which flows in a direction perpendicular to a magnetic field \vec{B} . In the mixed state of type II superconductors, the principle for the appearance of a Hall resistance is the same, though in this case it is the motion of vortices which gives rise to the Hall field. For the purpose of simplification, the case of a single vortex in a superconductor will be considered, as shown schematically in Figure 5.1. The situation shown is that of a superconductor in the vortex state, immersed in a magnetic field perpendicular to the plane in the z

direction with a current applied at 90° in the x direction. As previously described, this situation produces a force acting on the vortex in the positive y direction: the Lorentz force

$$\vec{F}_L = -\Phi \frac{(\vec{J} \times \vec{n})}{c}, \quad (5.1)$$

where Φ is the total flux, \vec{J} is the applied current density and \vec{n} is a unit vector pointing in the direction of the flux. However, if the vortex moves precisely in the direction of the Lorentz force, no Hall voltage will be induced. Moving flux tubes in the direction of the Lorentz force only set up an electric field

$$\vec{E} = \Phi \frac{\vec{v} \times \vec{n}}{c}, \quad (5.2)$$

which is parallel to the transport current and in which \vec{v} is the velocity of the vortex (see Figure 2.1). In order to give rise to a measurable Hall voltage, vortex motion has to proceed at some angle to the Lorentz force as shown by \vec{v} in Figure 5.1; it is the component of vortex motion v_x parallel to the transport current which is responsible for the Hall voltage. Notice also that if one inverts the magnetic field direction, the Hall voltage does not change sign since in this case, both \vec{v} and $\Phi\vec{n}$ are reversed, such that \vec{E} stays the same.

5.2 Anisotropic Pinning and Guided Vortex Motion

Observations by Niessen and Weijnsfeld [61] of transverse voltages in type-II superconductors lead to a description of Hall effects in such systems as being composed of two distinct contributions: a “true” Hall effect and a mere transverse voltage; this measurable transverse voltage being the result of guided motion of vortices. As will be shown, this guided motion of vortices can be caused by preferred directions of pinning resulting from structural asymmetry left from the fabrication of the sample. It is of primary importance in such an instance to determine how this channeling of vortices affects the transverse voltage because it indubitably determines a spurious Hall angle having no intrinsic significance.

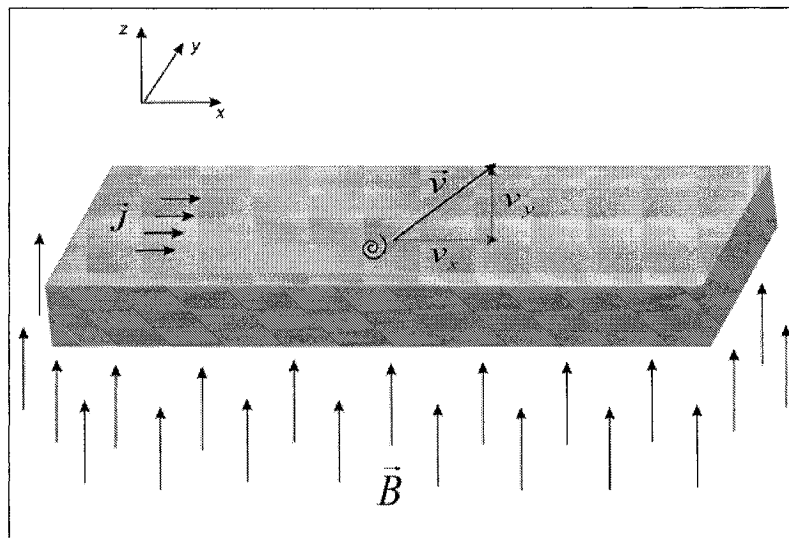


Figure 5.1: Schematic representation of the direction of motion of a vortex such that a Hall voltage is induced.

The force \vec{F}_L on the vortices resulting from a current \vec{J} applied in the longitudinal direction and a magnetic field applied perpendicular to both the current and the plane of the sample is still given by equation 5.1. In the absence of pinning, the vortices will move under the influence of that force in the direction perpendicular to \vec{J} , but this moving flux tube will generate eddy currents which will subject the vortices to a damping force \vec{F}_d . This damping force is velocity dependent:

$$\vec{F}_d = -\eta\vec{v}, \quad (5.3)$$

where η is a constant determined by the vortex and the conductivity in the normal state; the vortex velocity will increase until \vec{F}_L and \vec{F}_d balance each other. The moving vortices will also generate an electric field as given in equation 5.2. If Hall effects in the normal core are included in this phenomenology, the damping force will be shifted by an angle θ_H , the Hall angle in the normal vortex core. This will now cause the balance of forces to be achieved by the motion of vortices in the direction of the angle θ_H with respect to the applied current. Resulting from this, both a longitudinal and a Hall-like transverse voltage can be measured. Going back to equation 5.2, observe that upon reversal of the magnetic field direction, both vectors

$\Phi\vec{n}$ and \vec{v} change sign such that the electric field is left unchanged. This demonstrates why the transverse resistance remains unchanged upon reversal of the direction of the magnetic field.

However, the preceding description can only be applied to ideal systems without impurities nor defects, but experiments are performed on real systems in which pinning effects are present, and if the pinning centers are distributed inhomogeneously then anisotropic effects may occur. We will consider a case such that the pinning centers are arranged in planes making some angle θ with the current direction, which act as energy barriers of some height. The component of the Lorentz force perpendicular to the barrier will be counterbalanced by the barrier (up to some force threshold), so that the vortices which are subject only to the component of the Lorentz force parallel to the barrier will move along it. The angular dependence of this generated longitudinal and transverse electric fields is found to be

$$E_{\perp} \sim F_{L\parallel} \cos \theta = F_L \sin \theta \cos \theta \sim F_L \sin 2\theta \quad (5.4a)$$

$$E_{\parallel} \sim F_{L\parallel} \sin \theta = F_L \sin^2 \theta. \quad (5.4b)$$

This $\sin 2\theta$ dependence of the transverse resistance was observed in ref. [62], but the $\sin^2 \theta$ of the longitudinal electric field was not found; a divergence attributed to vortex slips across the barriers which were not taken into account here. These vortex slips occur if the component of the Lorentz force perpendicular to the barrier becomes greater than the maximum guiding force provided by the barrier; in such a case, the vortices tend to move in the direction of the large applied current. Therefore, the peculiar field dependence of the transverse voltage observed in ref. [60] is attributed to this competition between guided motion of vortices by the planar pinning centers and the thermal hopping motion over the barriers.

However, this phenomenology cannot be compared directly to our results because we do not have such large scale inhomogeneities as pinning barriers nor strong pre-

ferred pinning directions in our samples. Nevertheless, it shows that pinning can really influence the direction of vortex motion, which is a phenomenon we assume is taking place in our alloys.

Reports of a sign change of the Hall resistivity are numerous in both high- T_c [63, 64, 65, 66, 67] and low- T_c [56, 60] systems, as well as in numerical simulations of type II superconductors [68]. In any case, pinning could be the cause of this anomaly [53] as will be described now.

The idea is that for the positive Hall effect to take place, the magnitude of the pinning force $|\vec{F}_p|$ along the transverse direction would be smaller than the magnitude of the Lorentz force $|\vec{F}_L|$ along the opposite direction, thus setting up an electric field in the positive y direction ($R_{xy} > 0$) as shown in Figure 5.2(a) where \vec{v}_L is the velocity of the vortex lattice and θ_H is the Hall angle. On the other hand, the condition for the negative Hall resistance is that the magnitude of the pinning force in the positive transverse direction be greater than the magnitude of the Lorentz force in the negative transverse direction, thus setting up an electric field in the negative transverse direction ($R_{xy} < 0$), as shown in Figure 5.2(b).

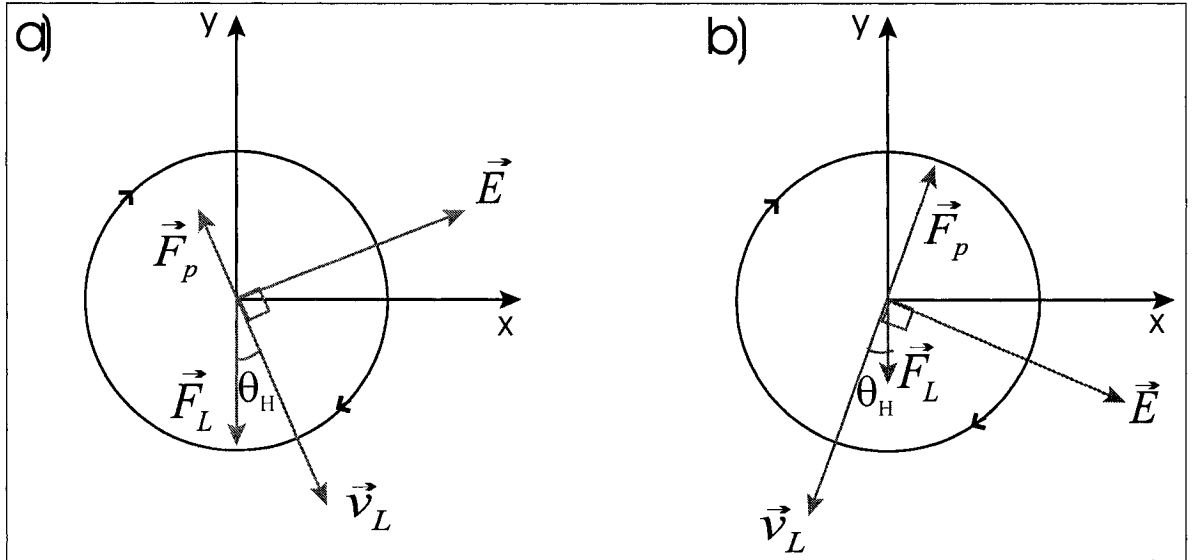


Figure 5.2: Schematic representation of the effective forces on the vortices for a) the positive Hall effect; b) the negative Hall effect.

5.3 A First Description of the Hall Angle

Among the first theories of vortex motion stands the pioneering work of Bardeen and Stephen [57], whose description of the forces acting on the vortices is as follows: in the absence of a driving current, the only force acting on the vortices is a viscous drag acting in the direction opposite to the force resulting from the driving current. [69]. However, upon application of a driving current, the force on the vortex line is given by the Lorentz force in equation 5.1. This excludes any force resulting from interaction between vortex lines.

Bardeen and Stephen [57] described the occurrence of Hall effects in superconductors in terms of the forces presented above in section 5.1. In addition, they predicted the Hall angle to remain the same as that in the normal state at a field equal to that in the core, or

$$\tan \theta_H = \tan \theta_{H_{c2}} \left(\frac{H}{H_{c2}} \right) = \left(\frac{e\tau}{mc} \right) H = \omega_c \tau, \quad (5.4c)$$

where ω_c is the cyclotron frequency. In terms of the longitudinal and transverse vortex velocity, the Hall angle is expressed as

$$v_{Lx} = v_{Ly} \tan \alpha = \left(\frac{H}{H_{C2}} \right) v_x, \quad (5.4d)$$

where v_x is the drift velocity of the electrons inside the core which results only from the transport current. Measurements of the Hall angle in our alloys of $\text{Fe}_x\text{Ni}_{1-x}\text{Zr}_2$ yield a Hall angle very different from this prediction, being highly nonlinear in magnetic field.

5.4 Transverse Critical Force

One of the main predictions from Le Doussal and Giamarchi [1] about transverse vortex motion is the existence of a transverse critical force for the depinning of vortices, which would give rise in this moving state to interesting effects such as hysteresis.

The transverse critical force is found to be

$$F_c^y \sim A \frac{c r_f}{(R_c)^2} \quad (5.5)$$

where $c = \sqrt{c_{11}c_{44}}$, A is a non-universal constant, r_f is the correlation range and c_{11} is the compression modulus. R_c is the dynamical Larkin length which represents the transverse dimensions of the region in which there is short-range order; it is defined as

$$R_c = \sqrt{32} \frac{c_{66}^{3/2} c_{44}^{1/2} a^2}{n f_{pin}^2}. \quad (5.6)$$

This expressions comes from simple estimates of the size of a region in which there exists short-range order due to the presence of defects. It supposes that the force of interaction of a lattice with one pinning center is f_{pin} , and that the lattice is shifted by period a due to the presence of the defects, while n gives the concentration of pinning centers. As a result, the transverse critical force is observed, not surprisingly, to depend strongly on the interaction of the lattice with the pinning centers.

5.5 Previous Measurements of the Hall Resistivity in Type II Superconductors

One of the first observation of the Hall voltage in type II superconductors [60] was performed on alloys of Nb and Ta which interestingly also show the peak effect. The Hall voltage is found to have two distinct peaks, one at the onset of the pinning phase responsible for the peak effect, and the other at H_{c2} . The dip between the two peaks corresponds with the reentrant pinning phase of the peak effect. A sign change is also observed. These results are interpreted in terms of a competition between guided motion of vortices and vortex slips over pinning barriers, which would cause these sudden increase of the Hall resistance, as discussed in section 5.2. We will see later that these results are the ones which, to the best of our knowledge, most closely resemble our measurements of the Hall resistance in the metal glasses $\text{Fe}_x\text{Ni}_{1-x}\text{Zr}_2$, though the Hall resistance peaks we observe are much more pronounced,

like hallmarks of phase transitions. Also, the effect in our samples can not be due to guided motion of vortices since such large scale inhomogeneities as pinning barriers are not present, though it shows that some degree of pinning can cause such anomalous increase of the Hall signal.

In ref. [59], both ρ_{xx} and ρ_{xy} vs B measurements on the anisotropic superconductor 2H-NbSe₂ are reported, with ρ_{xx} showing the peak effect. In this study, ρ_{xy} is seen to increase linearly with field in the low field range, while no sign change is observed. Also, the Hall angle $\tan \theta_H = \rho_{xy}/\rho_{xx}$ assumes a constant value up to the peak effect, as predicted in the theory of Nozières and Vinen [70] in which

$$\tan \theta_H = \tan \theta_{H_{c2}} = \left(\frac{e\tau H_{c2}}{m} \right). \quad (5.7)$$

At the peak, the Hall angle starts increasing linearly with the field in the normal state. It is important to note that the theory in ref. [70] incorporates a finite pinning force, but arrives at the result that it does not affect the flux-flow Hall angle.

Other Hall resistivity measurements [56] also yield a ρ_{xy} which increases linearly with the field in the low field regime as predicted by the NV theory [70], though it departs rapidly from this behavior and starts decreasing at higher field. Interestingly, it attains a minimum exactly at the position in H corresponding to the peak effect, above which it increases sharply. A sign reversal of ρ_{xy} is also observed, though it is argued that it can not originate from pinning effects. The proposed explanation for the observed departure from the NV theory is that in the regime in which the discrepancy occurs, the density of vortices increases and inter-vortex interaction become important such that treating them as independent vortices, as implied in the theoretical models, becomes inadequate.

Finally, Hall effects measurements in the mixed state of amorphous Mo₃Si [71] show a Hall angle which increases as the current is increased, but also find a Hall conductivity σ_{xy} which is independent of the current density over the entire field range, which would indicate that the Hall conductivity is independent of pinning. This is

explained by the argument that as the current is increased, vortex velocity increases equally, but the pinning force remains the same, thus the relative strength of pinning diminishes with increasing current. Therefore, if σ_{xy} is independent of current, it also has to be independent of pinning since the relative pinning strength changes with current. Their observed $\sigma_{xy} \sim 1/B$ dependence at low fields is in agreement with predictions from Nozières and Vinen [70] and with the time-dependent Ginzburg-Landau theory [72, 73]. At the highest fields, the Hall conductivity dependence is $\sigma_{xy} \sim B$.

6

HALL RESISTANCE RESULTS

This chapter will present the results of the measurements of the Hall effect in our Fe-Ni-Zr-based metal glasses; it will be divided in several parts. The first segment will discuss results pertaining to all samples; it will be followed by a presentation of the results in three different current drive regimes. Novel results were obtained, namely large peaks in the Hall resistance as a function of magnetic field, which we associate with orientational phase transitions. A comparison of the Hall resistance with the phase diagram obtained from longitudinal resistance measurements is then shown. Various topics concerning the results will also be discussed, such as the Hall angle and the $V - I$ characteristics. The chapter will be concluded by a presentation of the variation of the Hall resistance with temperature. At this point, a qualitative explanation for the experimental results obtained will be reached.

The geometry used for the Hall measurements of the alloys of $\text{Fe}_x\text{Ni}_{1-x}\text{Zr}_2$ is shown in Figure 6.1.

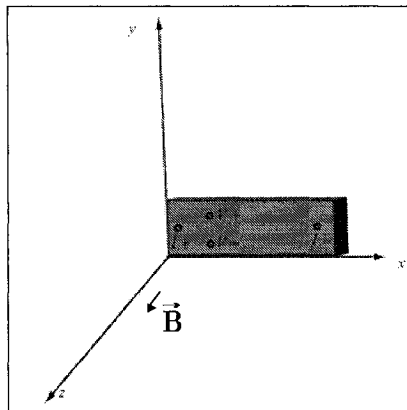


Figure 6.1: Geometry used in the measurements of the Hall effect. The current is applied to the sample along the x axis and the magnetic field is applied along the z axis.

6.1 Paths of Vortex Flow

Measurements of the Hall resistance on a sample of $\text{Fe}_{0.3}\text{Ni}_{0.7}\text{Zr}_2$ on which the voltage contacts are not suitably at 90° to the current directions are shown in Figure 6.2. In these results, one sees that the diagonal component overshadows significantly the Hall contribution¹, such that the only signature of the off-diagonal contributions are the small irregularities in the high- B depinning 1 phase. These curves were all acquired with the same driving current and show from different up and down B sweeps that the inconspicuous structures are repeated from sweep to sweep; an indication that the vortices almost invariably follow the same paths of motion in the sample. Similar evidence of fixed motion paths were observed in ref. [60, 61].

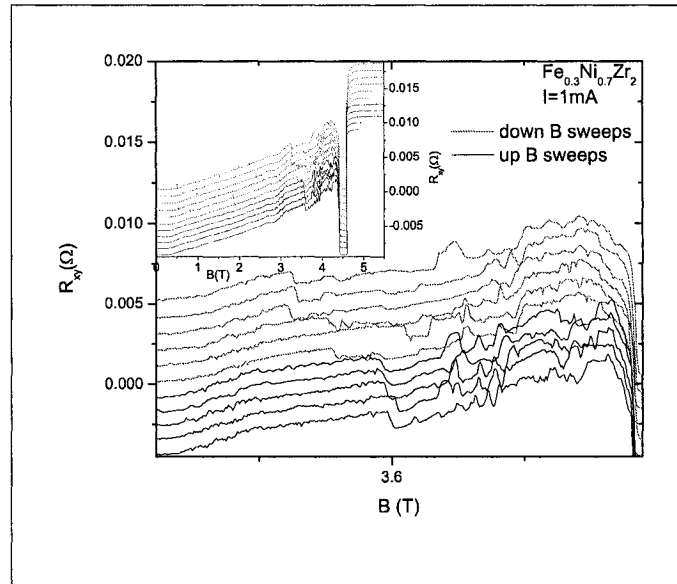


Figure 6.2: Enlargement of the high- B depinning 1 phase region of the R_{xy} vs B curves shown in the inset.

6.2 Reversing the Magnetic Field Polarity

The Hall resistance was also observed not to change sign and to have the exact same magnetic field dependence under the exchange of polarity of the B field, as observed

¹The longitudinal signal is typically 100 times larger than the transverse signal here such that any misalignment between the Hall probes causes the longitudinal voltage to hide any Hall voltage.

in Figure 6.3 showing data from sample $\text{Fe}_{0.1}\text{Ni}_{0.9}\text{Zr}_2$. This particularity of the Hall resistance in superconductors was expected [60, 61, 74] as described in section 5.1 and is seen in all the other samples.

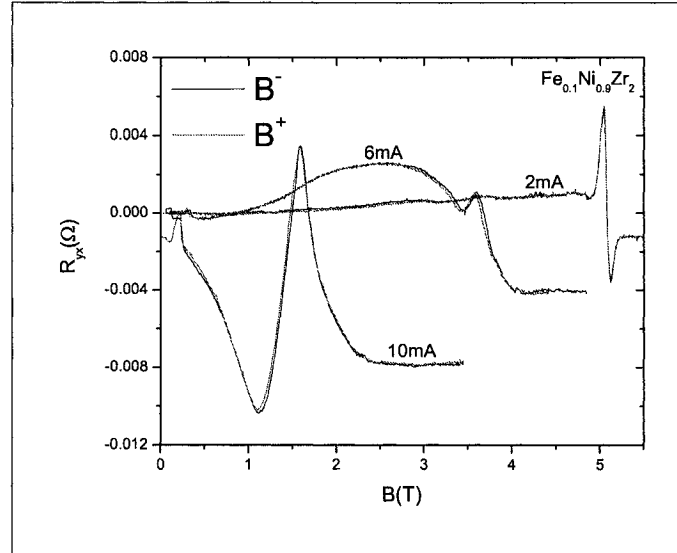


Figure 6.3: Hall resistance *vs* B field for up B sweeps for the two magnetic field polarities.

Now, the Hall resistance results will be introduced for three different current drive regimes. This is done because the data was found to exhibit three different characteristic behaviors corresponding to three current drive regimes.

6.3 Lowest Drive Regime

A typical Hall resistance curve observed in the lowest driving current regime is shown in Figure 6.4 for sample $\text{Fe}_{0.3}\text{Ni}_{0.7}\text{Zr}_2$; the corresponding R_{xx} curve is also shown for comparison. In this low-drive regime, the longitudinal resistance barely shows the peak effect and a sharp transition (less than 150 mT) between the superconducting and the normal state is observed. Strikingly, the Hall resistance shows a huge sharp peak precisely at the transition between the superconducting and the normal state. This peak can only result from a sudden onset of vortex motion just before the transition to the normal state.

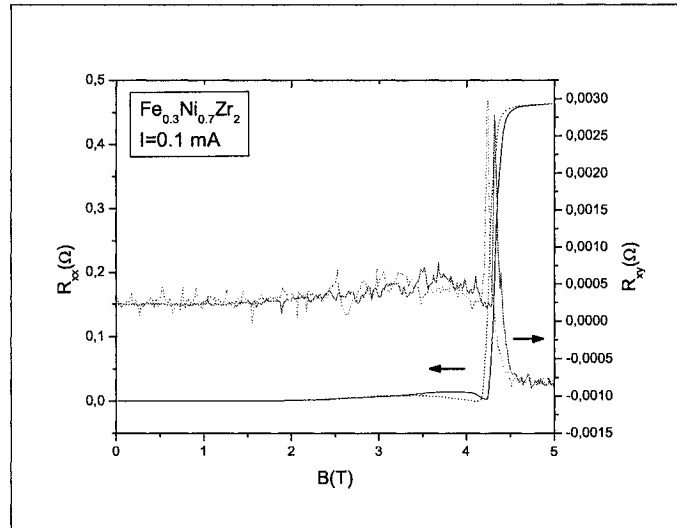


Figure 6.4: Longitudinal resistance (black curve) and Hall resistance (red curve) vs B field for up (solid lines) and down (dotted lines) B sweeps with $I = 0.1$ mA on a sample with $x = 0.3$.

6.4 Peak Effect Regime

In the slightly higher driving current regime, in which the peak effect is observed in the longitudinal resistance data (Figure 6.5), the Hall resistance now shows two very sharp peaks: in addition to the peak already observed at the normal-to-superconducting transition in the lowest drive regime, another peak is found at the onset of the reentrant pinning phase responsible for the peak effect. The amplitude of these peaks depends on the direction of motion of the vortices; very large peaks indicating that the direction of motion makes a large angle with the Lorentz force as described in section 5.3.

6.5 Largest Current Drive Regime

As shown in Figure 6.6, in the highest current drive regime, the longitudinal resistance does not show the peak effect anymore, and a direct and sharp transition between two depinned vortex phases is observed instead. Nevertheless, the Hall resistance shows again a single peak at the transition to the normal state, though this peak is much wider than the one observed in the lowest drive regime at this critical transition.

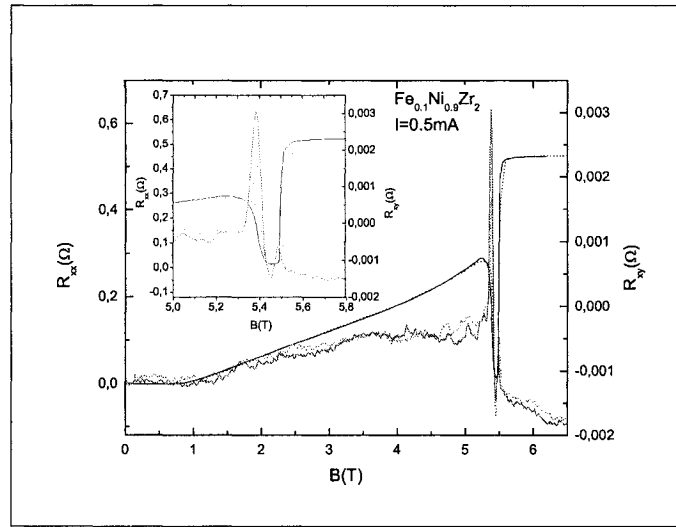


Figure 6.5: Longitudinal resistance (black curve) and Hall resistance (red curve) *vs* B field for up (solid lines) and down (dotted lines) B sweeps with $I = 0.5$ mA on a sample with $x = 0.1$. Inset: Enlargement of the peak effect region.

Gathering observations from the three regimes, we conclude that the Hall resistance peaks are observed whenever the vortex lattice undergoes a transition to a more disordered state, namely the pinning phase and the normal state. In fact, the peaks would be the signature of orientational phase transitions; their amplitude being dependent of the direction of vortex motion and their position in B being located precisely at the known disordering transitions. A way to understand how the peaks at the transitions occur is by considering what happens during a down B -field sweep starting for a sample in a disordered state in which the vortices are localized. In such a state, the vortex lattice is quite soft and adapts more easily to the pinning potential, but as the magnetic field decreases through a transition, the lattice becomes stiffer and vortex motion starts to proceed through channels (see section 2.2.7), suddenly giving rise to a measurable Hall resistance. As the magnetic field is decreased deeper in the quasi-ordered depinning phase, most vortices already move in the channels and the Hall resistance decreases to a more modest and normal value. In other words, it is really the sudden delocalization of the vortices which gives rise to the large peaks in the Hall resistance, and the direction in which motion proceeds establishes the amplitude of the peaks. No such important signature is observed in the Hall resistance

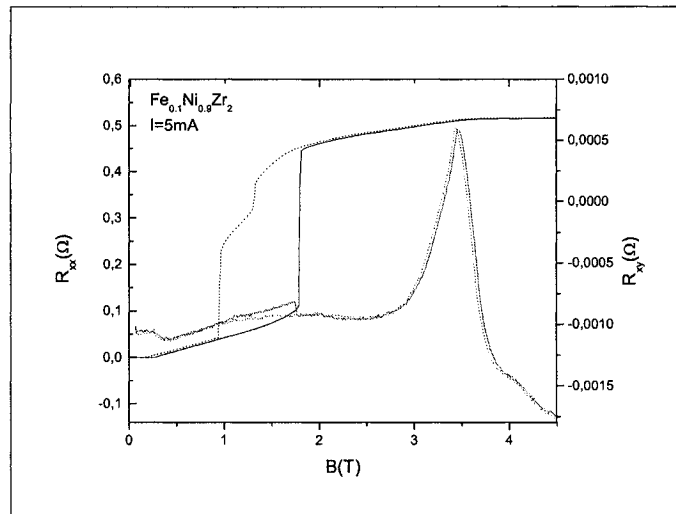


Figure 6.6: Longitudinal resistance (black curve) and Hall resistance (red curve) *vs* B field for up (solid lines) and down (dotted lines) B sweeps with $I = 5$ mA on a sample with $x = 0.1$.

at the direct transition between the depinning 1 and depinning 2 phase because both these phases have quasi-long-range order, such that correlations in the system at this transition do not change dramatically.

Furthermore, the width of the Hall resistance peak at the transition to the normal state reflects the size of the smectic (depinning 2) phase, which was observed in Figure 4.5 to be larger for higher driving currents, and non-existent for the lowest driving currents. However, the presence of these sharp peaks in the lowest drive Hall resistance curves would indicate that the depinning 2 phase indeed exists in the lowest drive regime, but would be extremely narrow.

6.6 Comparison with the Phase Diagram

The phase diagram of vortex motion extracted from longitudinal resistance measurements on sample $\text{Fe}_{0.1}\text{Ni}_{0.9}\text{Zr}_2$ (Figure 4.5) can be compared with the Hall resistance curves in order to establish the correspondence between these two types of measurements and how they relate with respect to vortex phases. This comparison is shown in a 3D graph in Figure 6.7, in which the Hall resistance is plotted against magnetic

field and current with the vortex phases explicitly shown. It is important to note that a straight line corresponding to the asymmetry in the Hall resistance was subtracted from the Hall curves in this graph in order to remove the diagonal components they contained.

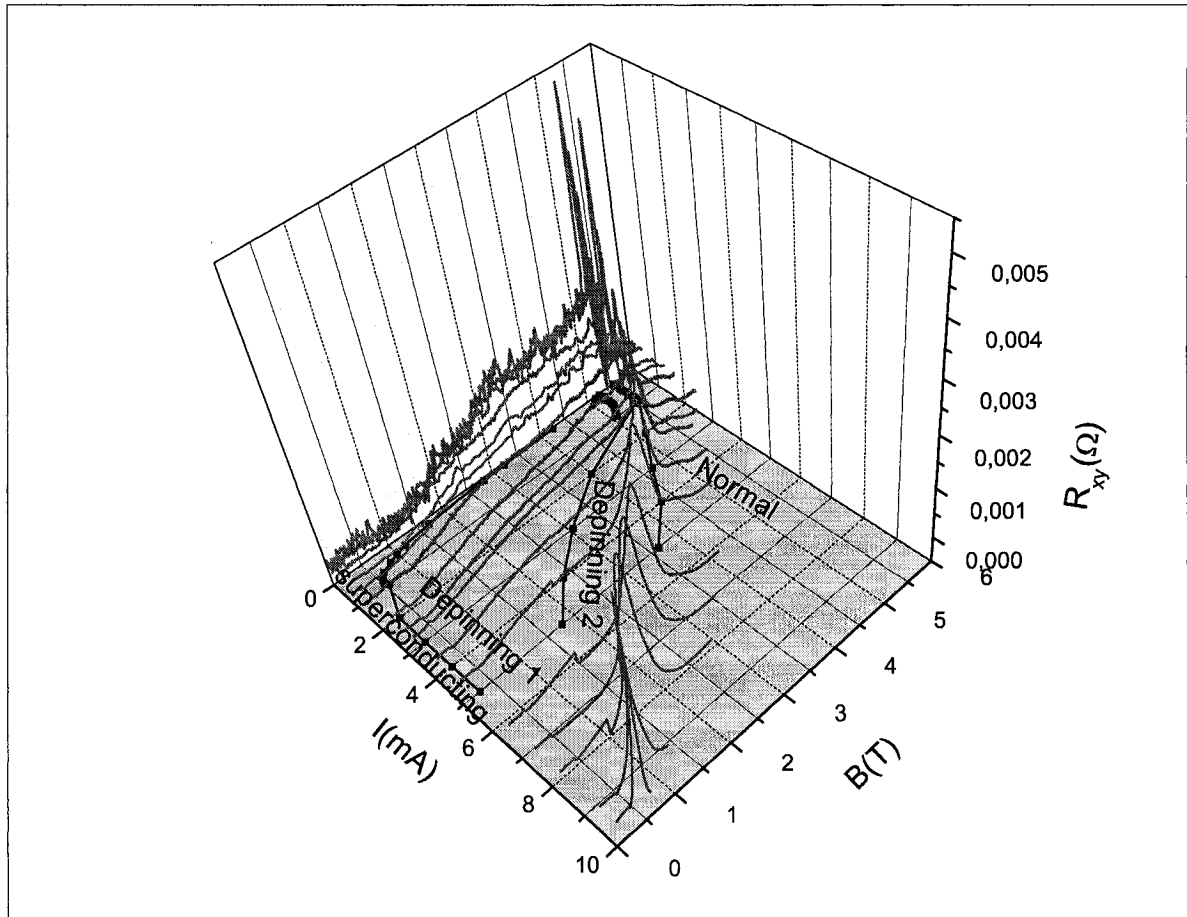


Figure 6.7: Hall resistance (red) vs B field for different driving currents and vortex phase diagram (blue) extracted from longitudinal resistance measurements shown on the same graph so that the correspondence between the two types of measurements can be established.

The Hall resistance peaks for all driving currents are observed to be located just below the transition to the normal state in the phase diagram. In addition, at driving currents below 2 mA, a second peak is also observed right at the onset of the pinning phase. As mentioned before, the widths of the peaks at the normal transition increase strongly with driving current, just as the smectic phase does. Also, the mere presence of the peaks at the lowest driving currents is evidence for the existence of this

second depinning phase in this regime, though also indicates that it is very narrow since the peaks are extremely sharp. To the best of our knowledge, this is the first reported evidence for the existence of the smectic phase right before the transition to the normal state in such low driving regime.

6.7 Results from Other Samples

Hall resistance measurements performed on samples with iron contents from $x = 0$ to $x = 0.40$ all yield similar results, as shown for instance in Figure 6.8 for a sample with $x = 0.3^2$. The shapes of the peaks are observed to differ from sample to sample, but the general behavior discussed in the previous sections is always found. For instance, the data shown in Figure 6.8(a) in the peak effect regime has the two characteristic peaks in the Hall resistance at the onset of the disordered phases, though the one at the pinning phase is quite buried in other structures resulting from some vortex motion out of the channels even in the MBG phase. Again, the sole presence of the peak is an indication of the same process taking place at the onset of the pinning phase in this sample too, and the differing peak amplitude merely indicate that the direction in which the vortices are traveling makes a larger or smaller angle with the Lorentz force, as will be discussed in more detail in section 6.8.

6.8 Hall Angle

We compute the Hall angle as the ratio of the Hall resistance to the longitudinal resistance $\tan \theta = \frac{R_{xy}}{R_{xx}}$ as discussed in section 5.3. The Hall angle is really a measure of the direction in which the vortices are moving, though the exact size of the angle is hard to determine because it dramatically depends on the position in B of the pinning phase for both R_{xx} and R_{xy} ; a small shift in one or the other induces a sizable change in the value of the angle. However, it is unquestionable that a *critical* angle dependence of the vortex flow direction when entering or leaving the disordered

²A complete set Hall resistance data can be found in Appendix B

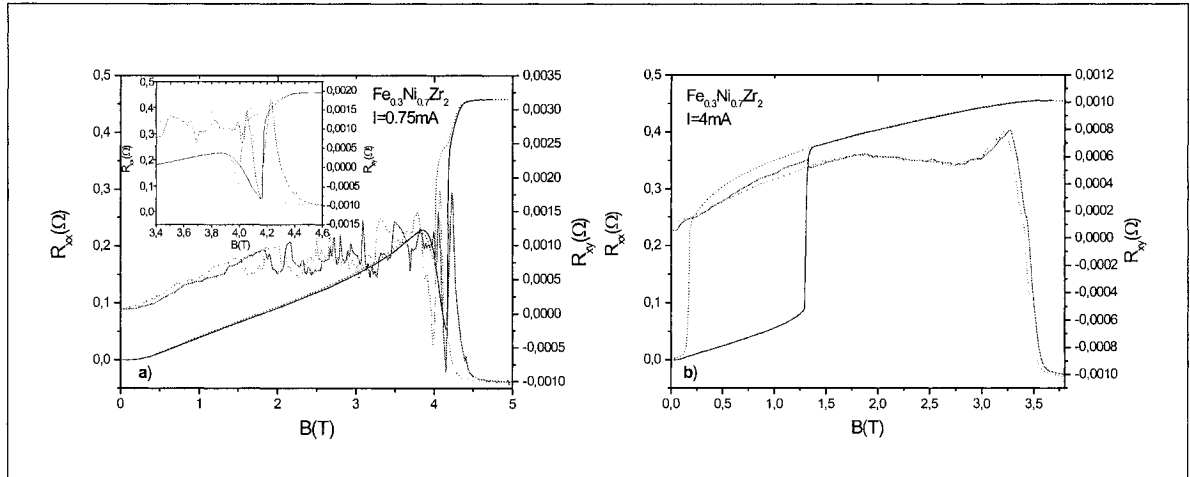


Figure 6.8: Longitudinal (black curves) and Hall (red curves) resistance as a function of B for up (solid lines) and down (dotted lines) B sweeps on sample $x = 0.3$ with a) $I = 0.74 \text{ mA}$ and b) $I = 4 \text{ mA}$.

phase is observed. For instance, the Hall angles shown in Figure 6.9 were computed assuming the “worst case scenario” meaning that the Hall resistance peak was carefully shifted such that no portion of the peak would correspond with the low resistance reentrant pinning phase of the longitudinal data, such that the smallest possible angle is computed. (Such a shifting of the data is legitimate as even small differences in the temperature from sweep to sweep induce some shift in the data.) The results are nonetheless striking as angles between 2° and -6° are found. In fact, the angles are very close to zero from the low B region up to the peak effect region, at which point a large positive peak is observed and is immediately followed by a large negative peak. The amplitude of these peaks is found to decrease with increasing drive and this difference between the amplitude of the Hall angle at the peaks for the different excitation curves is very dramatic: more than one order of magnitude between the $I = 0.1 \text{ mA}$ and the $I = 1 \text{ mA}$ curves.

The Hall angle shown in Figure 6.9 in $x = 0.1$ displays the behavior of the Hall angles observed in all other samples, for all driving currents in the peak effect regime; the angle goes from strongly positive at the onset of the pinning phase to strongly negative deep in the pinning phase at the onset of the depinning 2 phase. Since this

behavior is observed in all cases, we expect it to be the signature of orientational phase transitions, meaning that the channels in which the vortices move would suddenly reorient while the system suffers the disordering transitions.

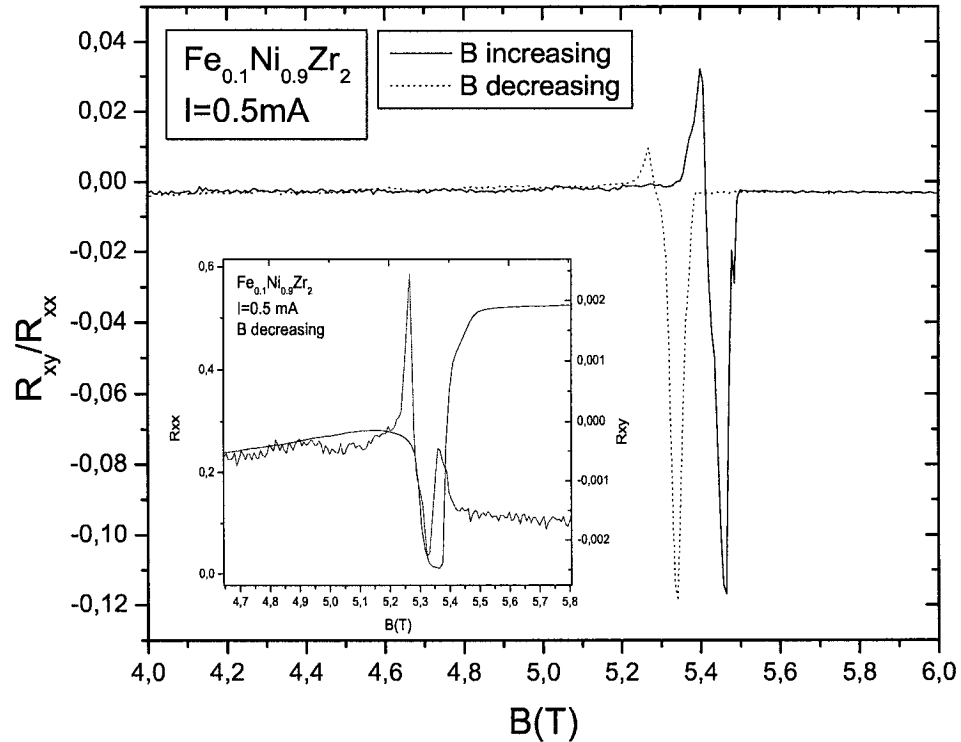


Figure 6.9: Hall angle *vs* B field for up (solid line) and down (dotted line) B sweep and sample $x = 0.1$ with $I = 0.5 \text{ mA}$. Inset: Longitudinal (black curve) and Hall (blue curve) resistance *vs* B showing the position of the Hall peak with respect to the reentrant pinning phase for careful computation of the Hall angle.

6.9 Local or Extended Effect

The measured Hall resistance is already known to depend strongly on the position of the contacts to the sample; if the voltage probes are not perfectly at 90° to the current direction, even a small diagonal component of the resistivity will overshadow the interesting features of the Hall signal. However, this does not answer the question: are the peaks in the Hall resistance the result of local vortex motion or do they result from an extended effect? In order to shed light on this issue, a sample with three pairs of Hall probes was prepared; some results are shown in Figure 6.10 for a sample with $x = 0.15$. Panel a) shows curves measured in the lowest current drive regime. The green curve, which corresponds to a pair of voltage probes at one end of the sample shows a large asymmetry due to some misalignment of the contacts, but both the red and blue curves show a very limited diagonal component. In any case, the Hall resistance measured at three different locations on the sample yields this characteristic single sharp peak at the transition between the superconducting and the normal state in the lowest drive regime. However, the position of the peak differs significantly from one pair of contacts to the other, even though it still could only be associated with the superconduction-to-normal transition.

We believe that such a shift in the peak position can not be caused by temperature differences between the sweeps since temperature variations are not that important at such low driving currents. Also, in this temperature regime (< 0.4 K), it is known that the temperature dependence of the upper critical transition is not strong (see Figure 4.12). On the other hand, some inhomogeneities in the sample could be the source of these differing peak positions, as this could cause parts of the sample to reach the normal state while others are still in the superconducting state, and this could be reflected in these local measurements. As the longitudinal resistance measurements reveal a transition to the normal state which is not very sharp and rather continuous, it is quite likely that this sample is not very homogeneous, most probably because it is not structurally relaxed.

The results in the peak effect regime, again at different locations of the sample are shown in panel b), in which one sees again these discrepancies in peak positions. Nevertheless, the results confirm quite well that the Hall resistance in this regime generally shows two peaks, independent of the location of the Hall probes on the sample. However, the smaller structures observed in these curves really differ and thus result from local attributes of the sample affecting vortex motion. Therefore, we conclude this section by asserting that the Hall resistance peaks result from an extended effect, though their shape and amplitude can be altered by local effects. Indeed, if the peaks are the signature of phase transitions, it is expected that they are observed at any location on the sample because at the phase transition, correlations become infinite such that the system itself becomes effectively infinite. In any case, the peaks really mark the event of major changes in the motion of vortices throughout the sample.

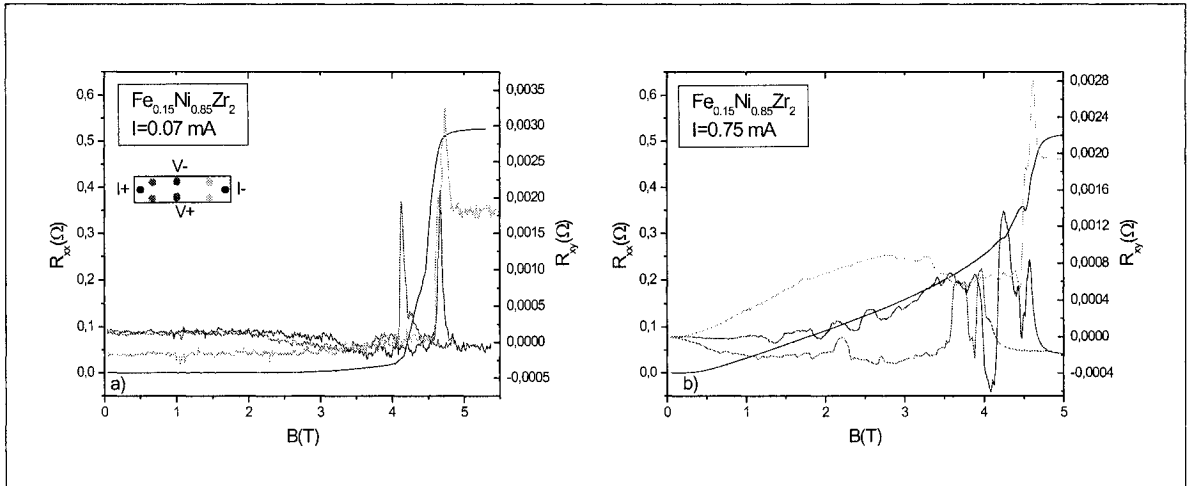


Figure 6.10: Longitudinal (black) and Hall (colors) resistance *vs* B for up B sweeps. a) $I = 0.07$ mA. b) $I = 0.75$ mA. The colors of the Hall curves correspond with different voltage probes as shown in the inset of panel a).

6.10 $V - I$ Characteristics

$V - I$ curves extracted from R_{xy} data from the $x = 0.1$ sample are found in Figure 6.11. The main panel shows curves for B/B_{c2} close to 1; the onset of the reentrant pinning

phase being found around $B/B_{c2} = 0.98$ is observed as a sharp peak in R_{xy} and is found in the $V - I$ curves as a bump at low I . Otherwise, we generally observe a decrease of the voltage with increasing driving current, though the analysis of the $V - I$ characteristics is quite tedious as no prevailing trend is observed, at least in the peak effect regime. However, as the inset of Figure 6.11 shows, the V dependence on I is fairly linear in the low- B and low- I regime; the same result is found in $V - I$ curves from the other samples³.

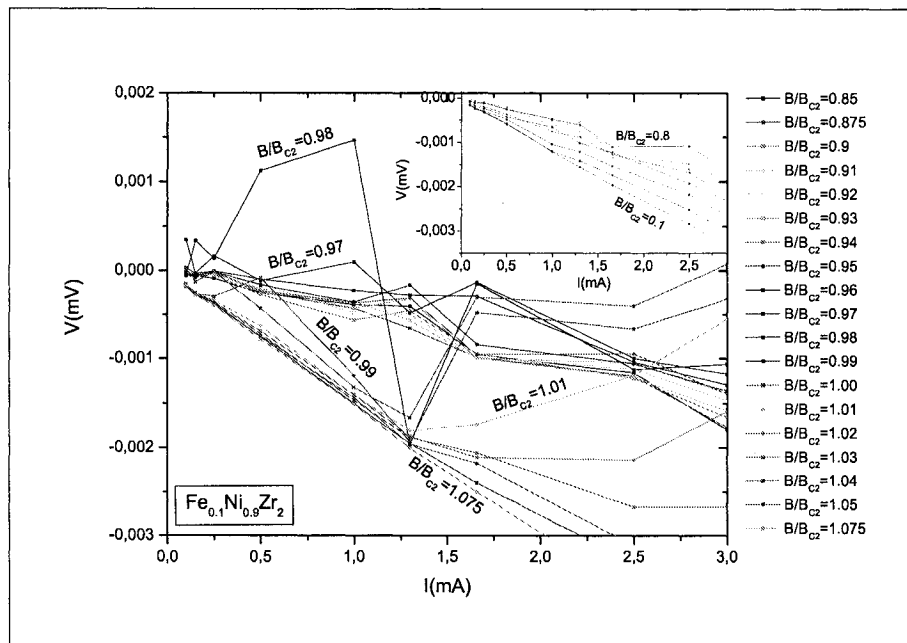


Figure 6.11: $V - I$ curves extracted from R_{xy} data acquired during an increasing B sweep for B/B_{c2} : main panel: in the peak region, inset: between 0.1 and 0.8.

Giamarchi [1] predicted the existence of a transverse critical force for the depinning of a vortex lattice at $T = 0$; the presence of such a force is not detected here in the $V - I$ curves where the transverse voltage tends to zero with the current. The existence of the transverse critical force can neither be inferred from the $V - I$ curves for the other alloys, which all show a V that decreases to zero with decreasing current. The existence of a transverse critical force raises important issues about history effects,

³ $V - I$ curves for the other alloys are found in Appendix B.

which are characteristic of a glassy state (such as the Bragg glass) in which the barriers become very large as $I \rightarrow 0$, as opposed to a liquid state in which they remain finite and no history dependence is expected.

6.11 Inverting the Current and Voltage Leads

Inverting the current and voltage probes, we obtain the Hall resistance (R_{yx}) curves shown in Figure 6.12 on sample $\text{Fe}_{0.1}\text{Ni}_{0.9}\text{Zr}_2$. The motivation for the presentation of these curves is that they show the same features as the Hall curves presented previously, thus establishing that this is a general result which does not arise from spurious effects of the contacts, nor from inhomogeneities in the sample. The odd-looking shape of the different I curves is most likely a result of a special current distribution in the sample, as one would expect from the contact geometry used and shown in the upper left corner of Figure 6.12. The principal feature of these curves, namely the huge sharp peaks at low driving current is very similar to that observed R_{xy} data in that they surpass well the high drive peaks. Also, despite some inconspicuous features, the general trend described for the R_{xy} measurements is still observed here, that is the single broad peak at high drive and the two sharp peaks at lower drive in the peak effect regime. Unfortunately, the position in B of the different peaks in the R_{yx} curves can not be compared directly to any R_{xx} data due to the impossibility of soldering four contacts in line on the ~ 1 mm wide samples, but owing to the similarities in the shapes of the Hall curves, it can be inferred that the high drive positive peak is located again at the transition to the normal state and the two low drive positive peaks correspond with the depinning 1 to pinning transition, and with the transition to the normal state.

6.12 Temperature Dependence

As for the R_{xx} data, the R_{xy} curves at different temperatures were acquired on sample $\text{Fe}_{0.4}\text{Ni}_{0.6}\text{Zr}_2$ with a driving current of 1 mA. Once again, the temperature over each B sweep was typically stable within 0.01 K for $T < 0.6$ K and within 0.07 K

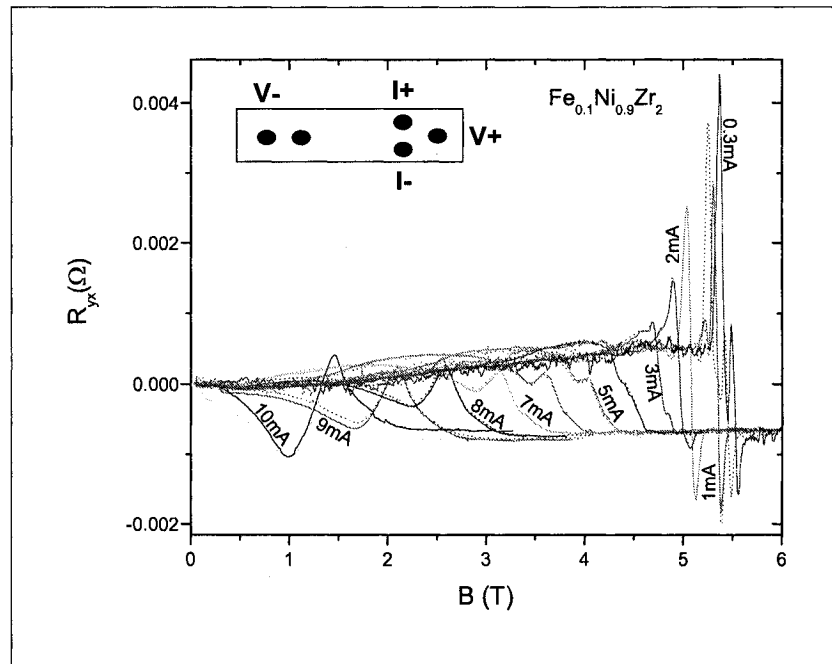


Figure 6.12: Hall resistance R_{yx} vs B field with the current and voltage contacts in the configuration shown in the upper left corner. The solid curves correspond to up B sweeps and the dotted lines to down B sweeps for $I=0.3, 1, 2, 2.5, 3, 4, 5, 6, 7, 8, 9, 10$ mA.

for $0.6 < T < 2$ K. The shape of the peak present at the transition to the normal state changes dramatically between $T = 0.62$ K and $T = 1.1$ K; it has some kind of plateau in the middle of the onset for the lower temperatures which disappears completely at higher temperature. Unfortunately, no data is available for temperatures between these two extremes due to the inability to stabilize the temperature within that range, making it all more difficult to understand how this peculiar structure disappears. However, the disappearance of this plateau seems to correspond with the narrowing of the pinning phase observed in the temperature dependence of the longitudinal data shown in Figure 4.12. The presence of this plateau could as well be related to the large depinning 2 phase present in this alloy. We expect this peak to be a hallmark of a phase transition, which implies that it should broaden significantly with increasing temperature; a characteristic which could not be investigated properly due to this evolution in the shape of the peak. R_{xy} vs B curves measured at different temperatures on a sample of $\text{Fe}_{0.15}\text{Ni}_{0.85}\text{Zr}_2$ shown in Figure 6.14 also yield

inconclusive results about the broadening of the peak.

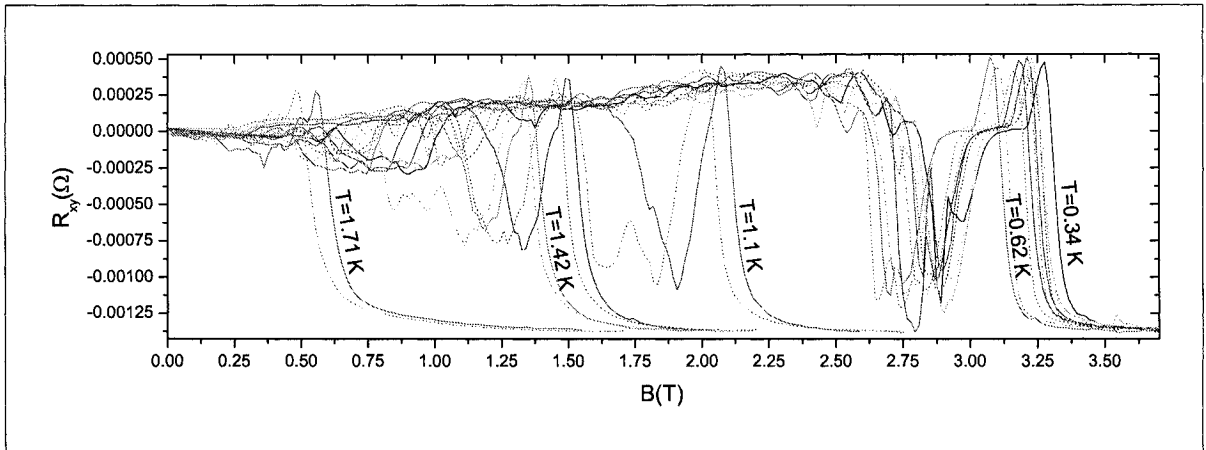


Figure 6.13: Hall resistance *vs* B field for up (solid lines) and down (dotted lines) B sweeps at different temperatures (0.34, 0.38, 0.45, 0.52, 0.62, 1.1, 1.35, 1.42, 1.71) K for sample $\text{Fe}_{0.4}\text{Ni}_{0.6}\text{Zr}_2$.

The R_{xy} curves at different temperatures are plotted in Figure 6.15 as a function of both temperature and magnetic field. The corresponding phase diagram extracted from the longitudinal resistance is also shown. The correspondence of the Hall peaks with the transition to the normal state is striking here again; the peak position in B moving to lower magnetic field value with increasing temperature at the same rate as the longitudinal upper critical transition does. However, it is to be noted that the shift in position of the pinning phase in the R_{xy} data with respect to that in the R_{xx} data results from an effect due to the sample itself; as shown before, the location of the contacts on the sample can influence the B -dependence of the different phases.

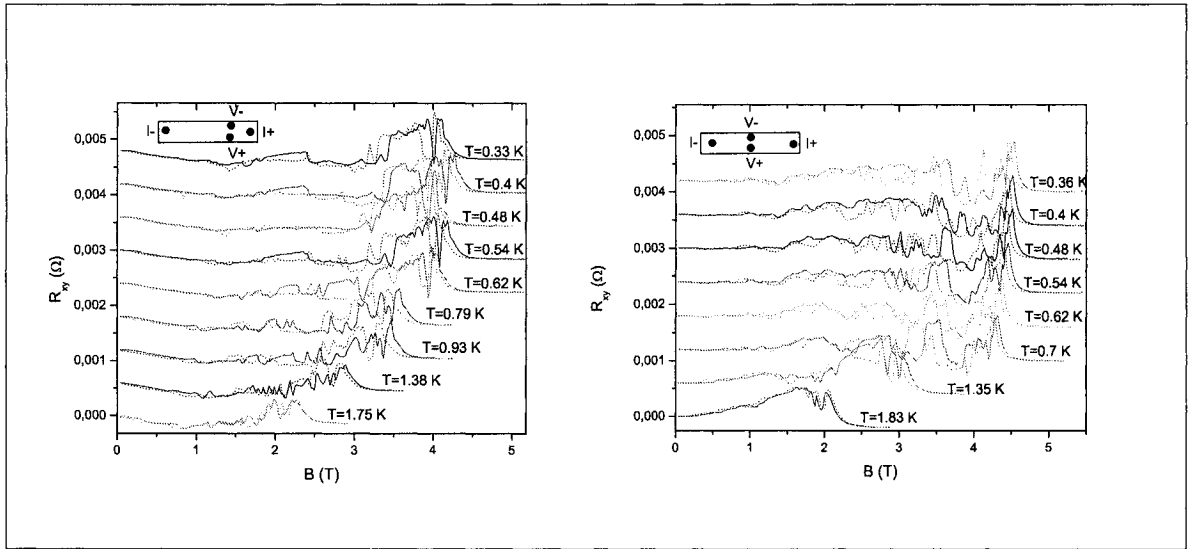


Figure 6.14: R_{xy} vs B for up (solid lines) and down (dotted lines) B sweeps at different temperatures below T_c on sample $\text{Fe}_{0.15}\text{Ni}_{0.85}\text{Zr}_2$, and for two different contact configurations. (The curves were shifted in R so as to show the features better.)

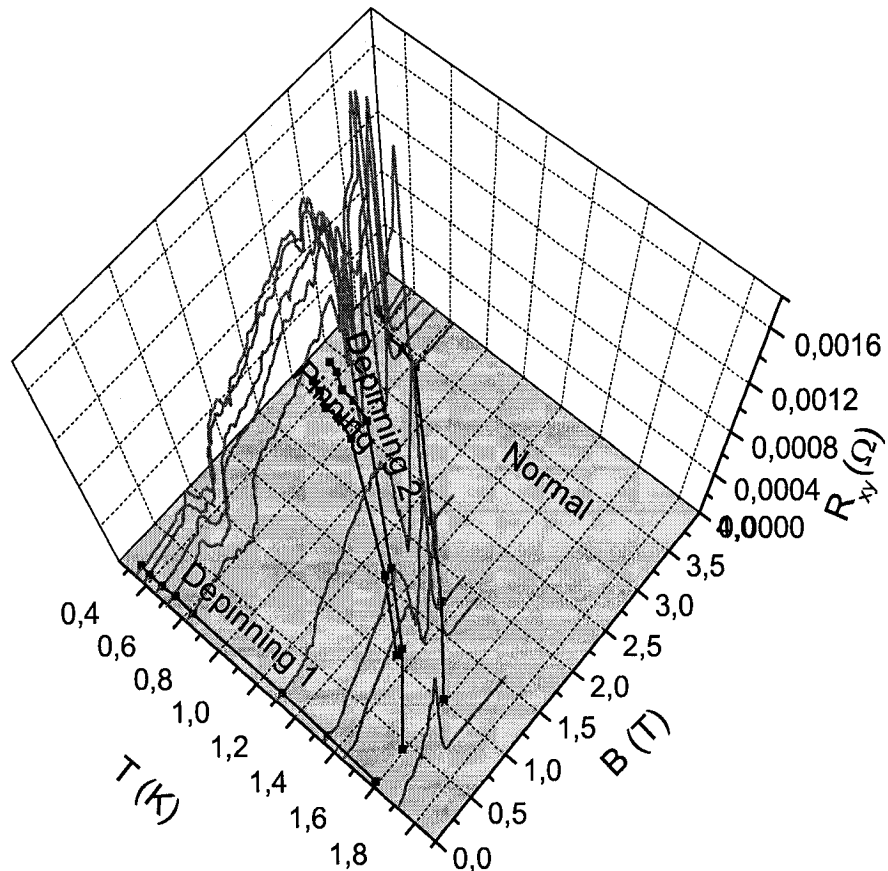


Figure 6.15: 3D plot of the Hall resistance (red) curves at different temperatures vs B field for up B sweeps and phase diagram (blue) extracted from R_{xx} measurements at different temperatures showing the evolution of the different phases of vortex motion with temperature.

CONCLUSIONS

Amorphous Fe-Ni-Zr-based materials with different concentrations of Fe were studied by dissipative transport (longitudinal and Hall) at temperatures below 400 *m* K, well below their superconducting transition temperature. Important information about the mechanisms of vortex motion in low- T_c type II superconductors were gained from such measurements.

For instance, the magnetic field dependence of the longitudinal resistance revealed a reentrant pinning phase characteristic of the anomalous peak effect. It was shown that the initial increase in resistance seen as the magnetic field is increased corresponds with a depinned vortex phase, the moving Bragg glass, in which quasi long-range is preserved and in which the vortices move in channels following each other like beads on a string. In this regime, the Hall resistance was found to be relatively smooth, though some features were still discernible; these small peaks result from some vortices slipping out of the channels in which they flow. However, in this case it is important to note that these vortex slippings are isolated events, and collective motion still proceeds through channels.

At higher magnetic field values and low driving currents, the longitudinal resistance was observed to decrease rather abruptly; this phase which is known as the peak effect is caused by a sudden softening of the vortex lattice which makes it adjust more easily to the pinning potential such that some, or all (in this case, one has a reentrant superconducting phase) the vortices get pinned again. This phase is highly disordered such that the peak effect is often described as arising from a disordering

transition. In the Hall resistance, the onset of this reentrant pinning phase is characterized by the presence of a very sharp peak, which was shown to be the signature of this disordering transition.

Still increasing the magnetic field, another depinned phase having directional quasi long-range order is encountered, which is characterized again by an increase in the longitudinal resistance when leaving the peak effect regime. The onset of this phase was found to be marked by a sharp minimum, often negative, in the Hall resistance.

Finally, as still slightly higher magnetic field values are reached, the system suffers the transition to the normal state through lattice melting; also a disordering transition. Correspondingly, another sharp peak is observed in the Hall resistance.

In the high driving current regime, the reentrant pinning phase is not present and the longitudinal resistance shows a direct transition between the two different moving vortex regimes: the first one, the MBG characterized by coupled channels, and the second one, most likely distinguished by uncoupled channels. A small drop in the Hall resistance was sometimes observed at this direct transition between two moving vortex phases, though this signature is very insignificant: it must arise from a sudden reorientation of the direction in which the vortices are moving, but not from such a dramatic disordering transition as that found between a moving vortex phase and a pinning phase. For instance, at the transition from the second moving vortex phase to the normal state, the strong wide peak observed in the Hall resistance marks the presence of the disordering transition, and the large width of the peak seems to be reminiscent of the size of the second depinning phase. Therefore, the conclusion can be reached that the Hall resistance peaks are the signatures of phase transitions from ordered to disordered vortex phases as can be inferred from their omnipresence at the onset of the pinning phase and at the transition to the normal state. Also, the negative Hall peak present at the onset of the second depinning phase equally marks

a phase transition, though now from a disordered to an ordered state for increasing B field. Moreover, the width of the peak marking the transition to the normal state was observed to increase with increasing drive, alike the size of the second depinning phase; an unambiguous indication of the relation existing between the Hall peak and the disordering transition.

In the lowest drive regime, a direct transition from the superconducting state, in which all vortices are pinned, to the normal state at which point the vortices cease to exist was expected. However, the indisputable presence of a peak in the Hall resistance at the transition to the normal state confers that a depinned phase exists even in this lowest drive regime, but would be very narrow as suggested by the limited width of the Hall peak.

The temperature dependence of the dissipative transport phenomena was also studied, and the expected lowering of the onset of the different B -driven phases with increasing temperature was observed in both the longitudinal and Hall resistances. Accordingly, the widths in B of the two depinning phases and of the pinning phase were seen to decrease with increasing temperature, but were always present.

In addition, the resistance measurements performed on different alloys with different iron concentrations yielded the anticipated lowering of B_{c2} with increasing iron concentration, except for a marked drop around $x = 0.2$ suggesting some inhomogeneity in the material probably arising from the fact that it was not structurally relaxed. Another distinctive behavior which marks the special character of samples having about 20 % of Fe is the very small pinning phase observed in samples with $x = 0.1$ and $x = 0.2$, which also suggests their inhomogeneity. However, a much more systematic study in which the resistance measurements would be performed on several different samples of each iron concentration would be required before reaching any valuable conclusion about the exact B -dependence of the various vortex phases.

A natural extension of this work would be to practice similar dissipative transport measurements on samples which are structurally relaxed, such that an exhaustive study of their properties could be performed. Also, another interesting project would be to measure the longitudinal and Hall resistance on other materials with a pinning potential as weak as the one characteristic of the materials used in this study, thereby establishing whether the behavior of the Hall resistance found in this study is ubiquitous to all weakly-pinned type II superconducting materials, or if it depends on the elements used here, namely Fe, Ni and Zr. This question is justified by the fact that no other studies have shown such strong features as the peaks observed in the Hall resistance here, although this could be due to the fact that, to the best of our knowledge, no other studies have been performed on samples having such a weak-pinning character.

A

MORE LONGITUDINAL RESISTANCE RESULTS

This appendix includes experimental results for the longitudinal resistance as a function of magnetic field for the samples of $\text{Fe}_x\text{Ni}_{1-x}\text{Zr}_2$ with $x = 0, 0.3, 0.33, 0.4$ (see page 35) and $V - I$ curves for samples with $x = 0, 0.1, 0.2, 0.4$ (see page 41).

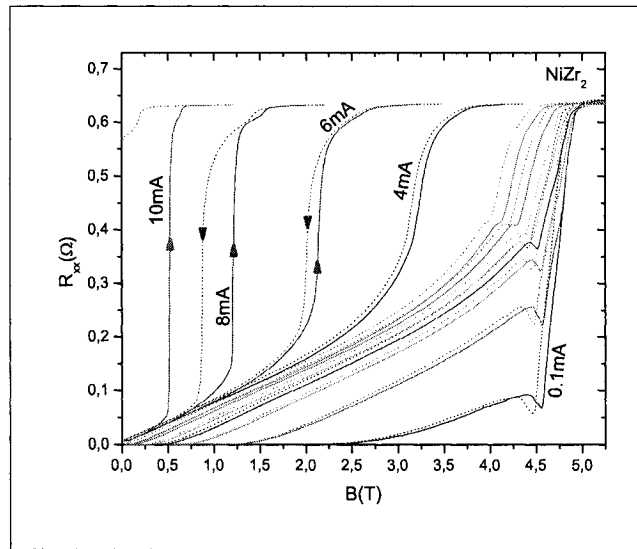


Figure A.1: Longitudinal resistance as a function of B for up (solid lines) and down (dotted lines) B sweeps on sample NiZr_2 and driving currents between 0.1 mA and 10 mA (0.1, 0.25, 0.5, 0.75, 1, 1.5, 2, 4, 6, 8, 10) mA. $T \approx 320$ mK.

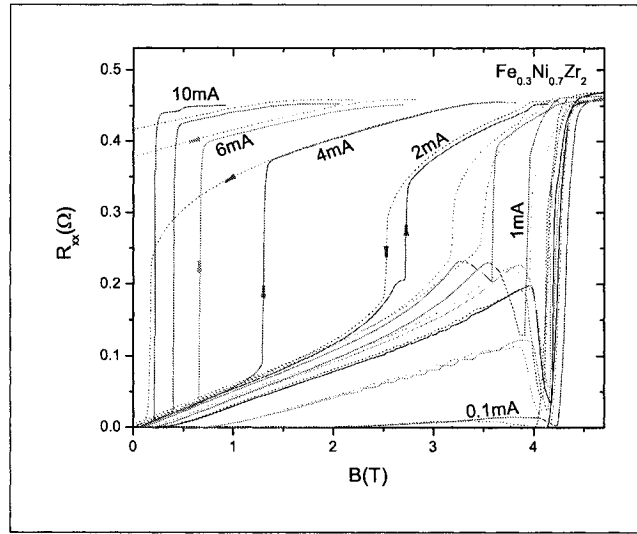


Figure A.2: Longitudinal resistance as a function of B , for up (solid lines) and down (dotted lines) B sweeps on sample $\text{Fe}_{0.3}\text{Ni}_{0.7}\text{Zr}_2$ with driving currents between 0.05 mA and 8 mA (0.05, 0.1, 0.25, 0.5, 0.75, 1, 1.5, 2, 4, 6, 8) mA. $T \approx 320$ mK.

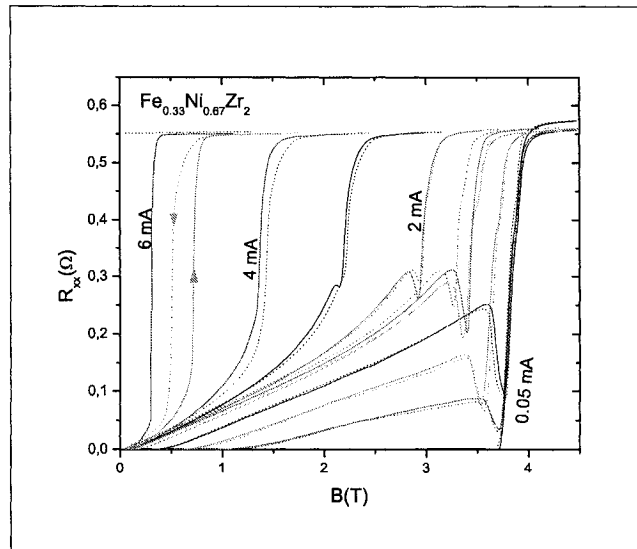


Figure A.3: Longitudinal resistance as a function of B for up (solid lines) and down (dotted lines) B sweeps on sample $\text{Fe}_{0.33}\text{Ni}_{0.67}\text{Zr}_2$ with driving currents between 0.05 mA and 6 mA (0.05, 0.15, 0.25, 0.5, 1, 1.5, 2, 3, 4, 5, 6) mA. $T \approx 320$ mK.

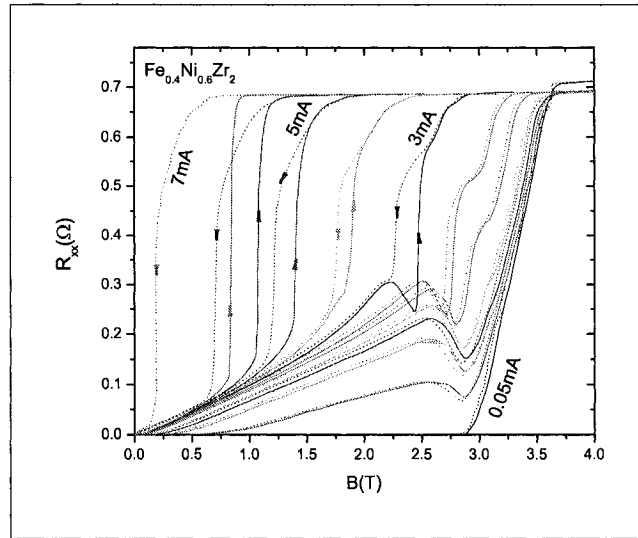


Figure A.4: Longitudinal resistance as a function of B for up (solid lines) and down (dotted lines) B sweeps on sample $\text{Fe}_{0.4}\text{Ni}_{0.6}\text{Zr}_2$. The different curves are for different driving currents between 0.05 mA and 7 mA (0.05, 0.25, 0.5, 0.75, 1, 1.5, 2, 3, 4, 5, 6, 7) mA. $T \approx 320$ mK.

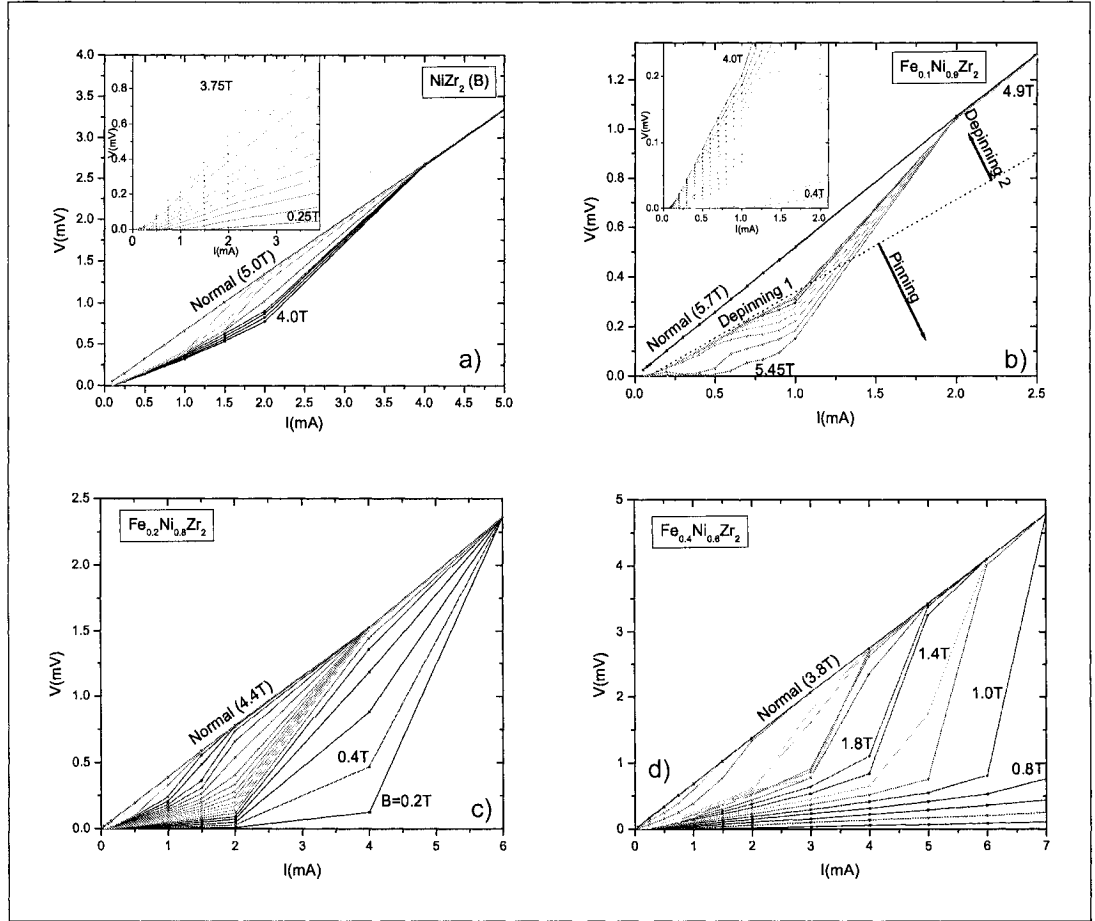


Figure A.5: $V - I$ curves extracted from R_{xx} vs B data acquired during increasing B sweeps for samples a) $x = 0$, b) $x = 0.1$, c) $x = 0.2$, d) $x = 0.4$.

B

MORE HALL RESISTANCE RESULTS

This appendix presents the R_{xy} and R_{yx} data not shown in the text for samples $x = 0, 0.1, 0.15, 0.2, 0.3, 0.4$ (see page 70) and the $V - I$ curves extracted from R_{xy} vs B data for some samples. (see page 75).

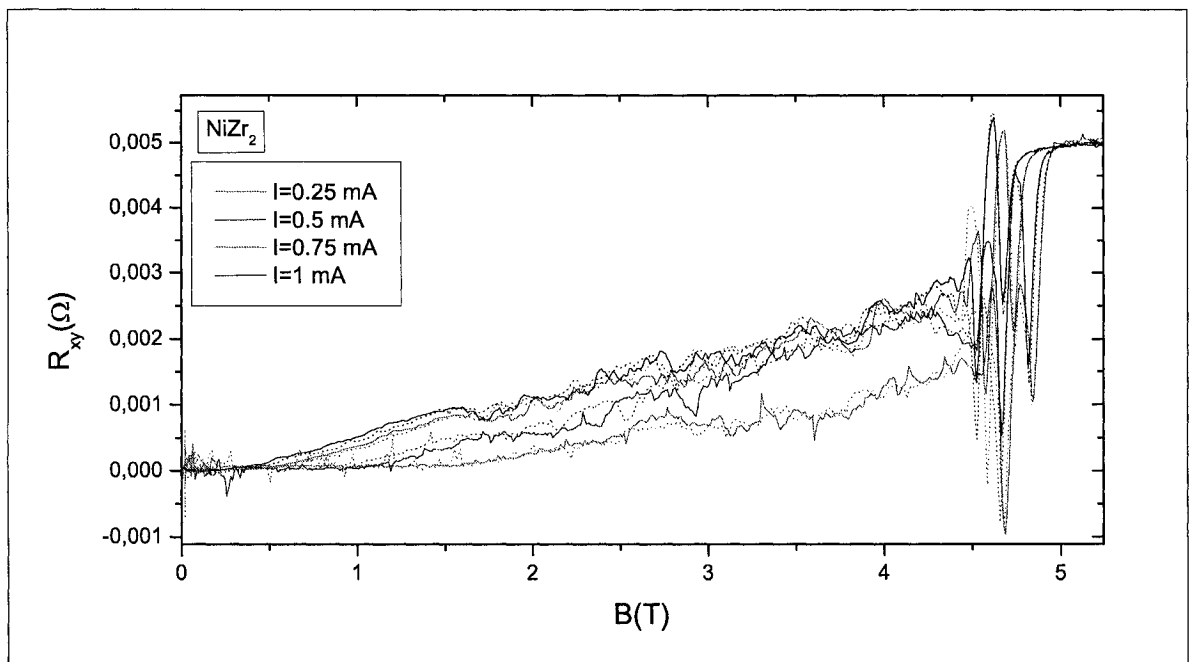


Figure B.1: Hall resistance vs B field for sample NiZr_2 . The solid lines correspond to data acquired during an increasing B sweep and dotted lines correspond to decreasing B sweeps.

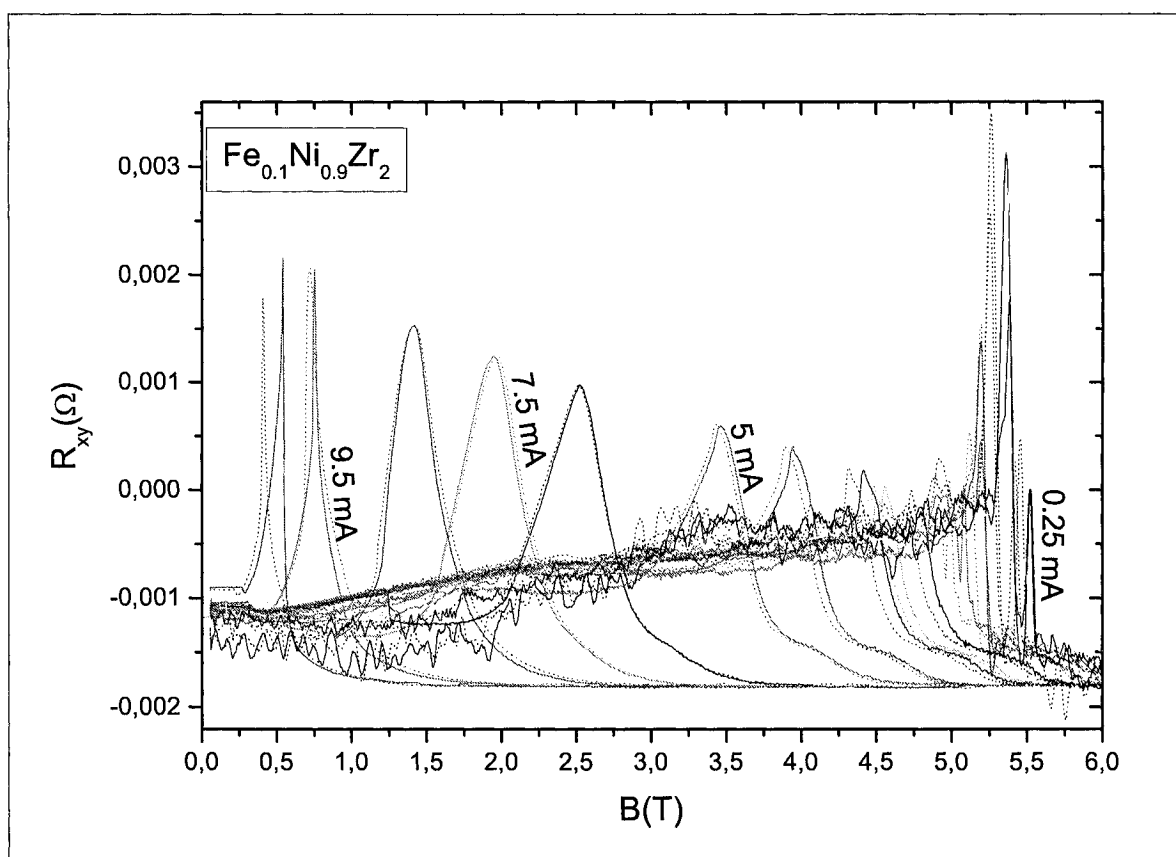


Figure B.2: Hall resistance vs B field for sample $\text{Fe}_{0.1}\text{Ni}_{0.9}\text{Zr}_2$. The solid lines correspond to up B sweeps and the dotted lines to down B sweeps and for the following driving currents: 0.1, 0.25, 0.5, 1, 1.3, 1.66, 2.5, 3, 3.33, 4.16, 5, 6.66, 7.5, 8.3, 9.5, 10 mA.

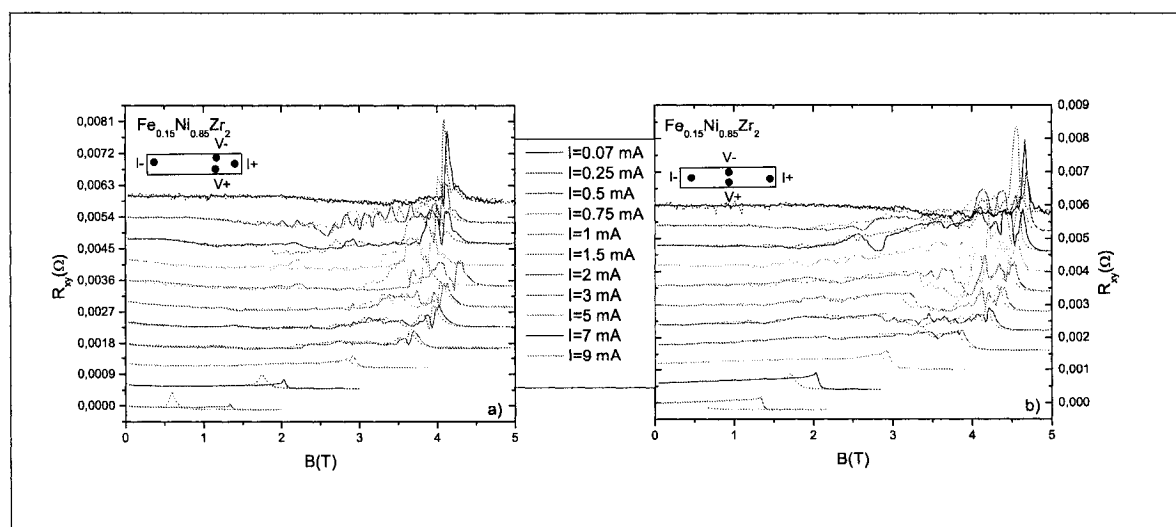


Figure B.3: R_{xy} vs B for up (solid lines) and down (dotted lines) B sweeps with different excitation currents. The curves were offset in R with respect to each other to make the structures more visible.

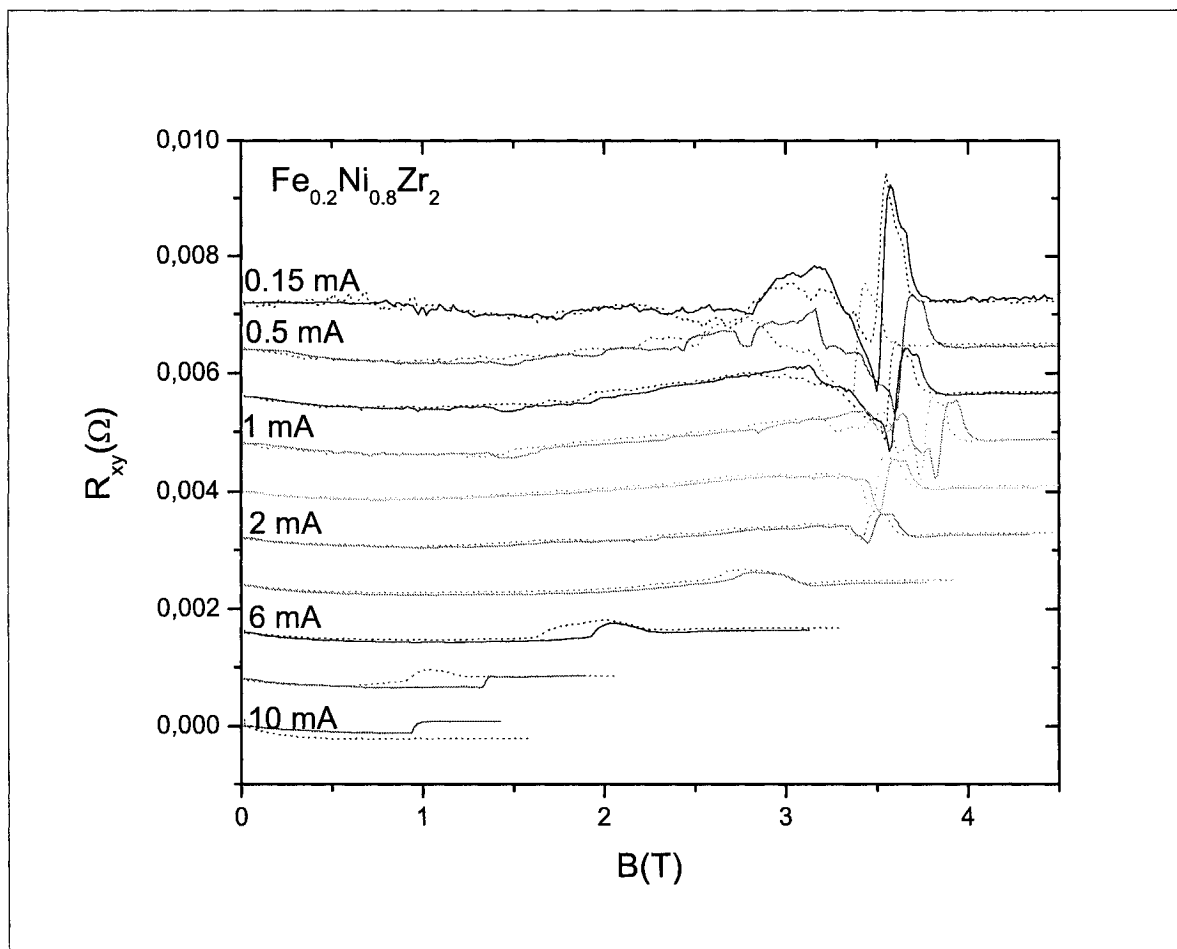


Figure B.4: Hall resistance as a function of magnetic field for up (solid lines) and down (dotted lines) B sweeps. These curves were also shifted in R with respect to each other in order to make the structures visible.

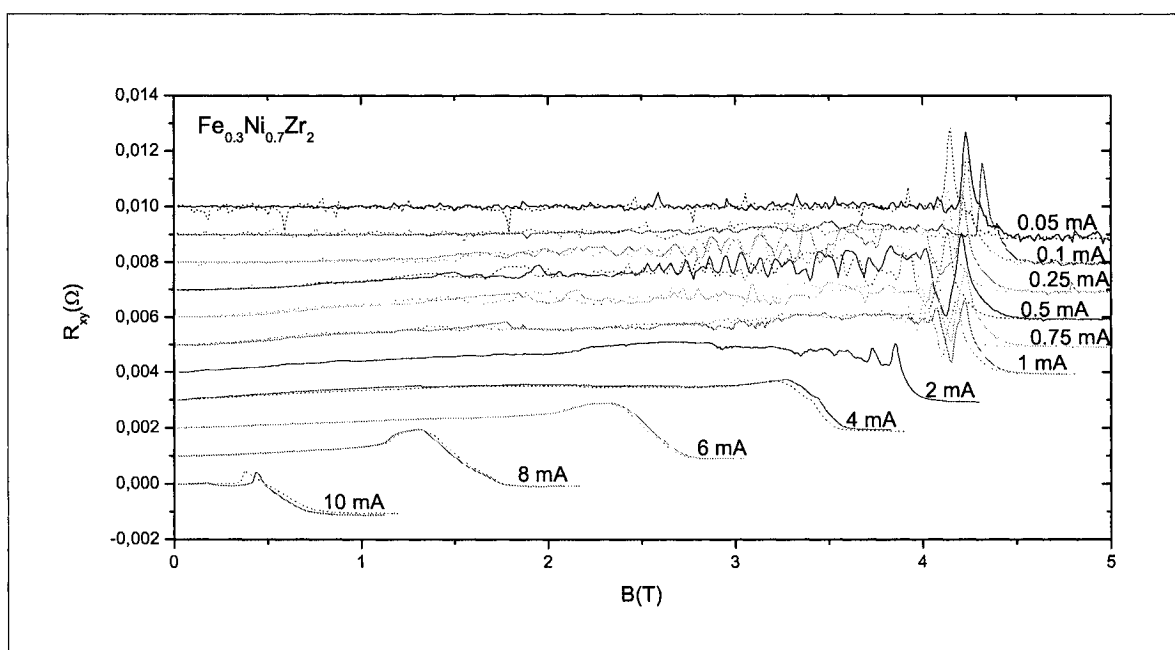


Figure B.5: Hall resistance vs magnetic field for up (solid B lines) and down (dotted lines) B sweeps for different driving currents between 0.05 mA and 10 mA on sample $x = 0.3$. The curves were offset with respect to each other to make the features visible.

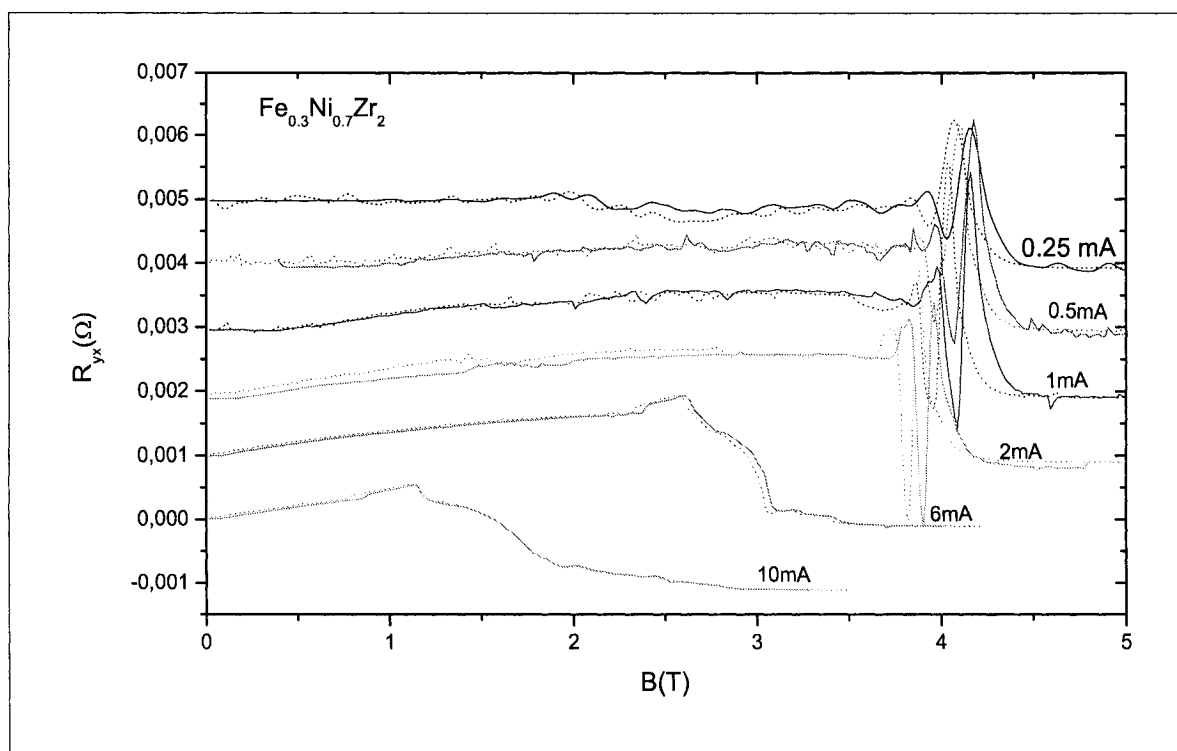


Figure B.6: Hall resistance (R_{yx}) vs B field for up (solid lines) and down (dotted lines) B sweeps and for $I=0.25, 0.5, 1, 2, 6, 10$ mA. The curves were also offset in R with respect to each other to make the structures visible.

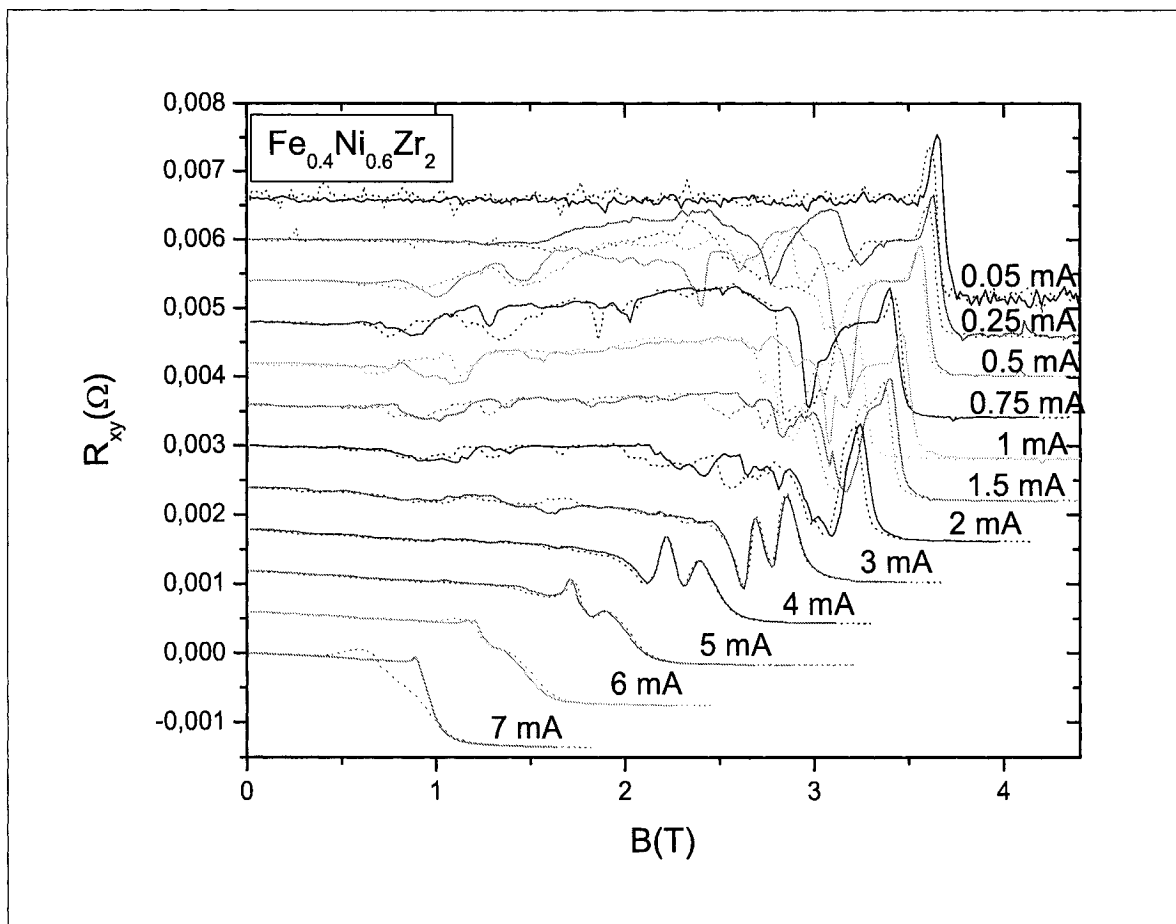


Figure B.7: Hall resistance vs magnetic field for up (solid lines) and down (dotted lines) B sweeps on sample $x = 0.4$. Curves were offset in R to make the features more visible.

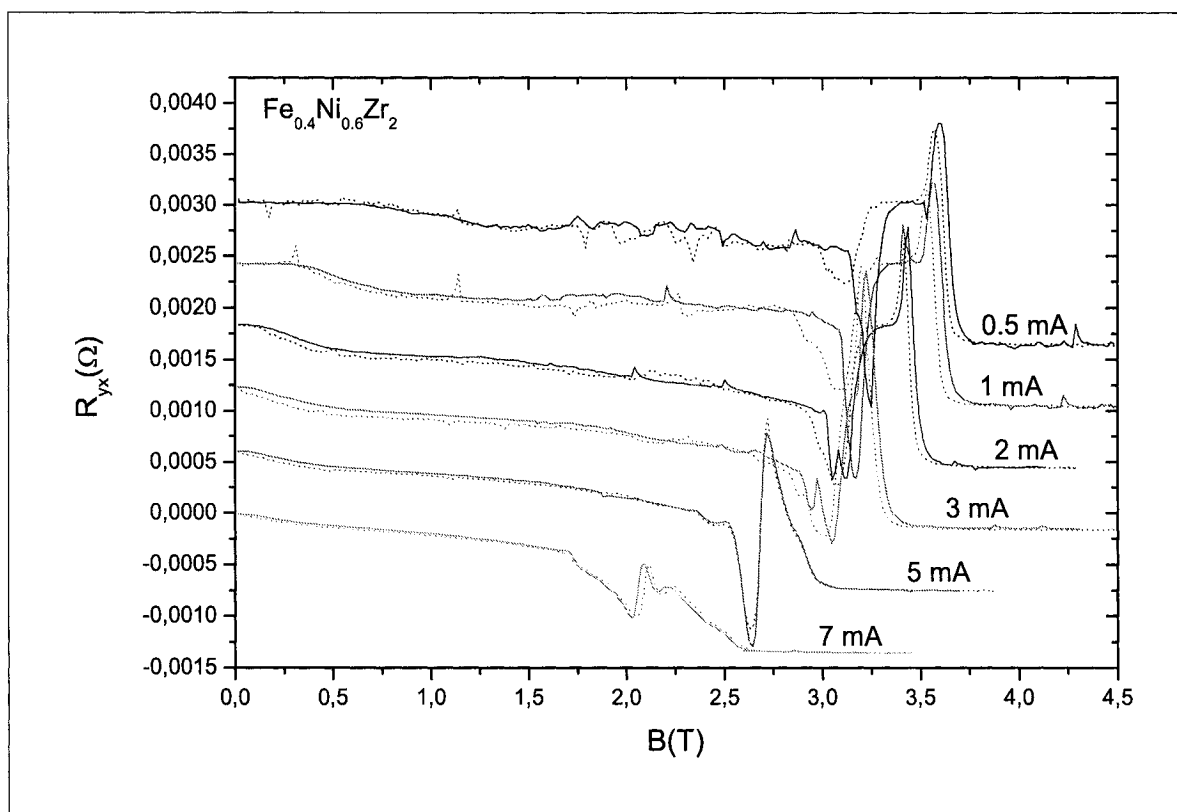


Figure B.8: R_{yx} vs B field for up (solid lines) and down (dotted lines) B sweeps with $I=0.5, 1, 2, 3, 5, 7$ mA. Curves were offset in R with respect to each other to make the structures more visible.

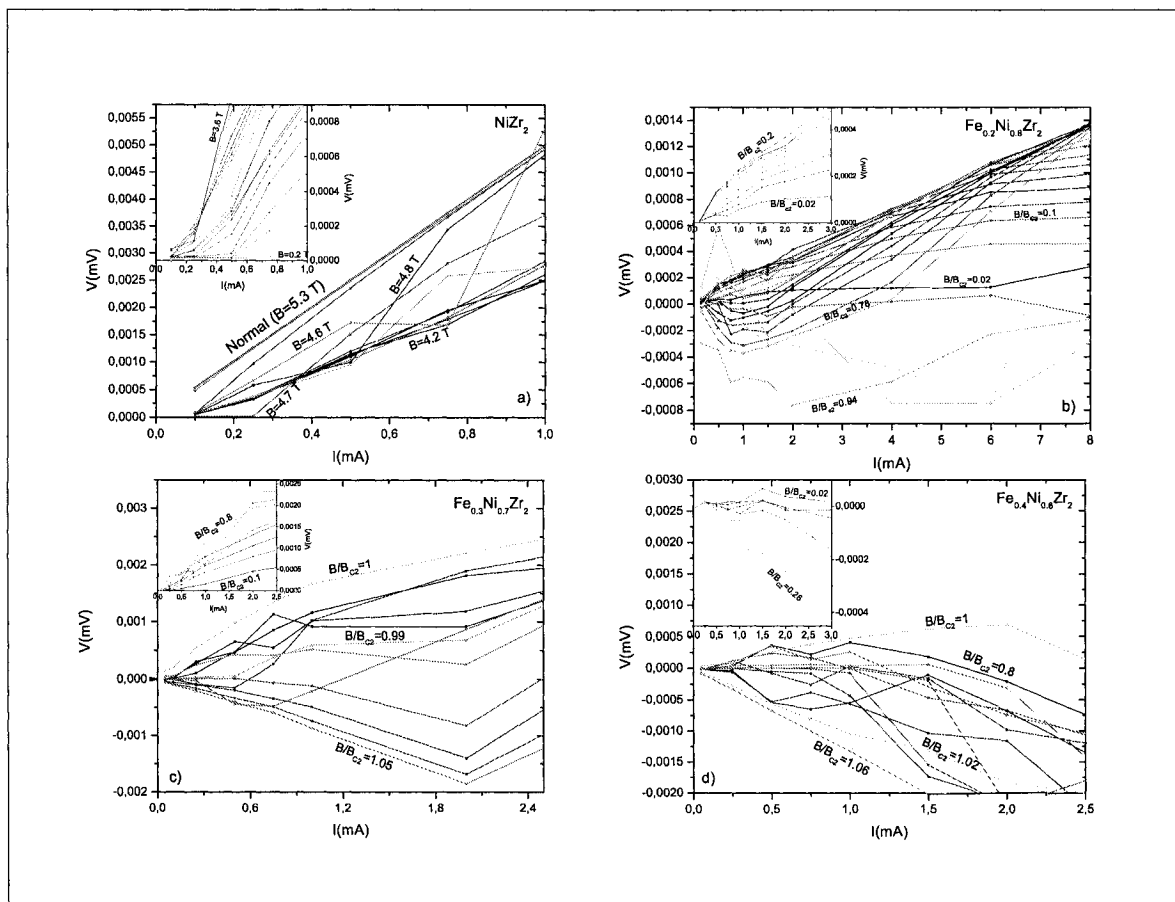


Figure B.9: $V - I$ curves for a) NiZr_2 b) $\text{Fe}_{0.2}\text{Ni}_{0.8}\text{Zr}_2$ c) $\text{Fe}_{0.3}\text{Ni}_{0.7}\text{Zr}_2$ d) $\text{Fe}_{0.4}\text{Ni}_{0.6}\text{Zr}_2$.

BIBLIOGRAPHY

- [1] Giamarchi, T. and LeDoussal, P. *Phys. Rev. B* **57**, 11356 (1998).
- [2] Tinkham, M. *Introduction to Superconductivity*. McGraw-Hill, (1975).
- [3] London, F. and London, H. *Proc. Roy. Soc. (London)* , 71 (1935).
- [4] Pippard, A. B. *Proc. Roy. Soc. (London)* , 547 (1953).
- [5] Ziman, J. M. *Principles of the theory of solids*. Cambridge, (1964).
- [6] Bardeen, J., Cooper, L. N., and Schrieffer, J. R. *Phys. Rev.* **108**, 1175 (1957).
- [7] Ginzburg, V. L. and Landau, L. D. *Zh. Eksperim. i Teor. Fiz.* **20**, 1064 (1950).
- [8] Abrikosov, A. A. *Sov. Phys. JETP* **5**, 1174 (1957).
- [9] Larkin, A. I. and Ovchinnikov, Y. N. *J. Low Temp. Phys.* **34**, 409 (1979).
- [10] Brandt, E. H. *Phys. Rev. B* **34**, 6514 (1986).
- [11] Wördenweber, R. and Kes, P. H. *Phys. Rev. B* **33**, 3172 (1986).
- [12] Banerjee, S. S., Patil, N. G., Ramakrishnan, S., Grover, A. K., Bhattacharya, S., Mishra, P. K., Ravikumar, G., Rao, T. V. C., Sahni, V. C., Higgins, M. J., Tomy, C. V., Balakrishnan, G., and Paul, D. M. *Phys. Rev. B* **59**, 6043 (1999).
- [13] Klein, T., Joumard, I., et al. *Nature* **413**, 404 (2001).
- [14] Ling, X. S., abd B. A. McClain, S. R. P., Choi, S. M., Dender, D. C., and Lynn, J. W. *Phys. Rev. Lett.* **86**, 712 (2001).
- [15] Giamarchi, T. and Bhattacharya, S. *High Magnetic Fields: Application in Condensed Matter Physics and Spectroscopy*. Springer-Verlax, (2002).
- [16] Paltiel, Y., Zeldov, E., Myasoedov, Y. N., Shtrikman, H., Bhattacharya, S., Higgins, M. J., Xiao, Z. L., Andrei, E. Y., Gammel, P. L., and Bishop, D. J. *Nature* **403**, 398 (2000).
- [17] Xiao, Z. L., Andrei, E. Y., Paltiel, Y., Zeldov, E., Shuk, P., and Greenblatt, M. *Phys. Rev. B* **65**, 094511 (2002).
- [18] Marchevsky, M., Higgins, M. J., and Bhattacharya, S. *Nature* **409**, 591 (2001).
- [19] Paltiel, Y., Zeldov, E., Myasoedov, Y. N., Rappaport, M. L., Jung, G., Bhattacharria, S., Higgins, M. J., Xiao, Z. L., Andrei, E. Y., Gammel, P. L., and Bishop, D. J. *Phys. Rev. Lett.* **85**, 3712 (2000).

- [20] Paltiel, Y., Myasoedov, Y. N., Zeldov, E., Jung, G., Rappaport, M. L., Feldman, D. E., Higgins, M. J., and Bhattacharrya, S. *Phys. Rev. B* **66**, 060503 (2002).
- [21] Giamarchi, T. and LeDoussal, P. *Phys. Rev. B* **52**, 1242 (1995).
- [22] Rosenblum, E. S., Autler, S. H., and Gooen, K. H. *Rev. Mod. Phys.* **36**, 77 (1964).
- [23] Kwok, W. K., Fendrich, J. A., van der Beek, C. J., and Crabtree, G. W. *Phys. Rev. Lett.* **73**, 2614 (1994).
- [24] Troyanovski, A. M., van Hecke, M., Saha, N., Aarts, J., and Kes, P. H. *Phys. Rev. Lett.* **89**, 147006 (2002).
- [25] Gammel, P. L., Yaron, U., Ramirez, A. P., et al. *Phys. Rev. Lett.* **80**, 833 (1998).
- [26] Fasano, Y., Menghini, M., de la Cruz, F., et al. *Phys. Rev. B* **66**, 020512 (2002).
- [27] Berlincourt, T. G., Hake, R. R., and Leslie, D. H. *Phys. Rev. Lett.* **6**, 671 (1961).
- [28] Kes, P. H. and Tsuei, C. C. *Phys. Rev. B* **28**, 5126 (1983).
- [29] Geers, J. M. E., Attanasio, C., Hesselberth, M. B. S., Aarts, J., and Kes, P. H. *Phys. Rev. B* **63**, 094511 (2001).
- [30] <http://musr.physics.ubc.ca/theses/Sonier/MSc/node11.html>.
- [31] Trudeau, M. *Étude de l'effect Hall et de la magnetoresistivité dans les alliages métalliques amorphes de M-Zr (M=Ni, Co et Fe)*. PhD thesis, Université de Montréal, Montréal, Canada, (1986).
- [32] Dikeakos, M. *Fe-TM-Zr alloys: from glass to big cube crystal*. PhD thesis, McGill University, Montréal, Canada, (2001).
- [33] Marder, M. P. *Condensed Matter Physics*. John Wiley and Sons, (2000).
- [34] Olson, C., Reichhardt, C., and Nori, F. *Phys. Rev. Lett.* **81**, 3757 (1998).
- [35] Fangohr, H., Cox, S. J., and de Groot, P. A. J. *Phys. Rev. B* **64**, 064505 (2001).
- [36] Chauve, P., Giamarchi, T., and LeDoussal, P. *Phys. Rev. B* **62**, 6241 (2000).
- [37] Hilke, M., Reid, S., Gagnon, R., and Altounian, Z. *Phys. Rev. Lett.* **91**, 127004 (2003).
- [38] Bhattacharya, S. and Higgins, M. J. *Phys. Rev. Lett.* **70**, 2617 (1993).
- [39] Mawatari, Y. *Phys. Rev. B* **59**, 12033 (1999).
- [40] Olson, C. J. and Reichhardt, C. *Phys. Rev. B* **64**, 140502 (2001).
- [41] Vinokur, V. M. and Nattermann, T. *Phys. Rev. Lett.* **79**, 3471 (1997).

- [42] Larkin, A. I. and Ovchinnikov, Y. N. *Sov. Phys. JETP* **41**, 960 (1976).
- [43] Larkin, A. I. and Ovchinnikov, Y. N. *Nonequilibrium Superconductivity*. Elsevier Science, (1986).
- [44] Musienko, L. E., Dmitrenko, I. M., and Volotskaya, V. G. *Sov. Phys. JETP Lett.* **31**, 567 (1980).
- [45] Klein, W. et al. *J. Low Temp. Phys.* **61**, 413 (1985).
- [46] Ruck, B. J., Abele, J. C., Trodahl, H. J., Brown, S. A., and Lynam, P. *Phys. Rev. Lett.* **78**, 3378 (1997).
- [47] Doettinger, S. G. et al. *Phys. Rev. Lett.* **73**, 1691 (1994).
- [48] Samoilov, A. V., Konczykowski, M., Yeh, N.-., Berry, S., and Tsuei, C. C. *Phys. Rev. Lett.* **75**, 4118 (1995).
- [49] Gurevich, A. V. and Mints, R. G. *Rev. Mod. Phys.* **59**, 941 (1987).
- [50] Stekly, Z. J. J. *Adv. Cryog. Eng.* **8**, 585 (1965).
- [51] Altounian, Z. and Strom-Olson, J. O. *Phys. Rev. B* **27**, 4149 (1983).
- [52] Marchevsky, M., Higgins, M. J., and Bhattacharya, S. *Nature* **409**, 591 (2001).
- [53] Wang, Z. D. and Ting, C. S. *Phys. Rev. Lett.* **67**, 3618 (1991).
- [54] Vinokur, V., Geshkenbein, V., Feigel'man, M., and Blatter, G. *Phys. Rev. Lett.* **71**, 1242 (1993).
- [55] Liu, W., Clinton, T. W., and Lobb, C. J. *Phys. Rev. B* **52**, 7482 (1995).
- [56] Bhattacharya, S., Higgins, M. J., and Ramakrishnan, T. V. *Phys. Rev. Lett.* **73**, 1699 (1994).
- [57] Bardeen, J. and Stephen, M. *Phys. Rev.* **140** (1964).
- [58] Schindler, A. I. and Gillespie, D. J. *Phys. Rev.* **130**, 953 (1963).
- [59] Jing, T. W. and Ong, N. P. *Phys. Rev. B* **42**, 10781 (1990).
- [60] Niessen, A. K. and Staas, F. A. *Phys. Lett.* **15**, 26 (1965).
- [61] Niessen, A. and Weijnsfeld, C. *J. Appl. Phys.* **40**, 384 (1969).
- [62] Staas, F., Niessen, A., Druyvesteyn, W., and Suchtelen, J. *Phys. Lett.* **13**, 293 (1964).
- [63] Hagen, S. J., Lobb, C. J., and Greene, R. L. *Phys. Rev. B* **41**, 11630 (1990).
- [64] Chien, T. R., Jing, T. W., Ong, N. P., and Wang, Z. Z. *Phys. Rev. Lett.* **66**, 3075 (1991).

- [65] Hagen, S. J., Smith, A. W., Rajeswari, M., Peng, J. L., Li, Z. Y., Greene, R. L., Mao, S. N., Xi, X. X., Bhattacharya, S., Li, Q., and Lobb, C. J. *Phys. Rev. B* **47**, 1064 (1993).
- [66] Nakao, K., Hayashi, K., Utagawa, T., Enomoto, Y., and Koshizuka, N. *Phys. Rev. B* **57**, 8662 (1998).
- [67] Göb, W., Liebich, W., Lang, W., Puica, I., Sobolewski, R., Ressler, R., Pedarnig, J. D., and Buerle, D. *Phys. Rev. B* **62**, 9780 (2000).
- [68] Zhu, B. Y., Xing, D. Y., Wang, Z. D., Zhao, B. R., and Zhao, Z. X. *Phys. Rev. B* **60**, 3080 (1999).
- [69] Bardeen, J. *Phys. Rev. Lett.* **13**, 747 (1964).
- [70] Nozières, P. and Vinen, W. F. *Philos. Mag.* **14**, 667 (1966).
- [71] Lobb, C. J., Clinton, T. W., Smith, A. W., Liu, W., Li, Q., Peng, J. L., Greene, R. L., Eddy, M., and Tsuei, C. C. *Appl. Sup.* **2**, 631 (1994).
- [72] Dorsey, A. T. *Phys. Rev. B* **46**, 8376 (1992).
- [73] Kopnin, N. B., Ivlev, B. I., and Kalatsky, V. A. *J. Low Temp. Phys.* **90**, 1 (1993).
- [74] Staas, F., Niessen, A., and Druyvesteyn, W. *Phys. Lett.* **17**, 231 (1965).